# NUMERICAL STUDY OF HIGH-PRESSURE ROTATING DETONATION ENGINES

A Dissertation

Submitted to the Faculty

of

Purdue University

by

Kota Mikoshiba

In Partial Fulfillment of the

Requirements for the Degree

of

Doctor of Philosophy

May 2020

Purdue University

West Lafayette, Indiana

# THE PURDUE UNIVERSITY GRADUATE SCHOOL
# STATEMENT OF DISSERTATION APPROVAL

Dr. Stephen D. Heister, Chair

School of Aeronautics and Astronautics

Dr. Haifeng Wang

School of Aeronautics and Astronautics

Dr. Carson Slabaugh

School of Aeronautics and Astronautics

Dr. Jonathan Poggie

School of Aeronautics and Astronautics

Dr. Swanand V. Sardeshmukh

School of Aeronautics and Astronautics

**Approved by:**

Dr. Gregory A. Blaisdell

Head of the School Graduate Program

For my parents

# ACKNOWLEDGMENTS

I would like to express my deepest appreciation to all who have supported my Ph.D. work. First, my Ph.D. research would not have been possible without the support and nurturing of Professor Stephen D. Heister. I also must thank my committee members: Dr. Haifeng Wang, Dr. Carson Slabaugh, Dr. Jonathan Poggie, and Dr. Swanand V. Sardeshmukh. I'd like to acknowledge the help and support of lab mates: David Stechmann, Brandon Kan, Wesly Anderson, Dasheng Lim, Jenna Humble, Alexis Harroun, Kevin Dille, and Steven Kubic. I'd also like to extend my gratitude to Kyle Schwinn and Ian Walters.

# TABLE OF CONTENTS

Page

# LIST OF TABLES

# LIST OF FIGURES

Figure Page

# ABSTRACT

Mikoshiba, Kota Ph.D., Purdue University, May 2020. Numerical Study of High-Pressure Rotating Detonation Engines. Major Professor: Stephen D. Heister Professor.

The potential higher performance of rotating detonation engines (RDEs), due to the constant volume combustion process, has attracted researchers and engineers from around the world. However, additional research is necessary to achieve higher performance because the dynamic nature of RDEs.

While a few experiments have been conducted for the injector dynamics for RDEs, this parameter plays a key role relative to the development of high performance RDEs. A parametric study of three dimensional computational fluid dynamics (CFD) simulations is performed to investigate dynamics of an oxidizer injector utilized in an RDE. Input parameters of this parametric study are the simulated detonation strength at oxidizer injector throat (i.e. inlet of a combustion chamber), the injector geometry and number of wave.

The injector dynamics potentially change local equivalence ratio before detonation wave arrival in an RDE chamber. Also, the injector spacing plays a large role in determining local mixing efficiency. From these point of views, a two dimensional non-premixed detonation parametric study is performed in order to investigate effects of injector mixing and mixing efficiency. An unwrapped domain in the azimuthal direction of an RDE chamber is considered and the mixing efficiencies and injector spacings are modeled as initial conditions.

In general, from the injector dynamics study, all the results show a strong attenuation of the detonation overpressures in the near field of the injector exit and as a result, the wave traversing the annular passage is largely acoustic in nature. With the mass flow inlet boundary condition employed, reflections are present at this boundary

and reflected waves have a non-negligible contribution to the transient mass flow of the injector. These mass flow pulsations could conceivably contribute to the formation of additional waves depending on their energy content and subsequent detailed mixing and combustion. Increasing the number of waves or shortening the length of the injector created reflections as one would predict from acoustic behavior. In the presence of higher amplitude waves these effects will likely be more pronounced. Together with the non-linearities in the heat release, the small fluctuations in the mass flow can significantly alter the detonation behavior.

The two dimensional non-premixed detonation parametric study further examines the effects of the potential non-uniform mixture due to the injector dynamics exposed to a single planer detonation wave. In all non-premixed cases, the detonation wave is decoupled with the pressure wave (the shock) and the combustion wave once the detonation wave arrives at the non-premixed target region. However, in the cases with the 45 mm and smaller injector spacings, the shock and combustion wave are recoupled. This decouple-explosion-recouple sequence becomes smoother and happens earlier with finer injector spacing. There are some higher pressure pockets than the CJ and the premixed case. The poor mixing efficiency cases show the similar decouple-explosion-recouple sequence.

The local high pressure in the detonated non-premixed and poor mixing cases is caused by the compression by the shock and other compression from the upstream high pressure pockets. Time scale separation of exothermic and endothermic reactions due to the non and poor mixing efficiencies allows the shock compression closer to the the classical Zel'dovich, Neumann, and Döring (ZND) model : the shock is the only pressurization mechanism the poor and non-mixing cases where as the combustion starts at the same time as the shock arrives in the premixed and good mixing efficiencies cases such as the baseline and Gaillard mixing efficiencies.

The non-premixed and poor mixing efficiency cases with the 45 mm or finer injector spacings provide the higher time and space averaged pressure at the injector surface than it of the premixed case. The poor mixing profile with 11.3 mm injector spacing is the best performer among the all cases in this part of parametric study with respect to pressure thrust. It may be possible to attain a desired axial pressure profile through injector design for specific mixing profile.

# 1. INTRODUCTION

## 1.1 Background

Recently, "pressure gain" combustion technologies have drawn researchers' attention because of their potential higher thermal efficiency associated with a constant volume heat release as compared to current devices approximated by constant pressure heat release in the Brayton thermodynamic cycle. For example, Figure 1.1 illustrates the potential work advantage of the detonation cycle versus a conventional Brayton cycle device. Basic thermodynamic studies indicated increased performance of 10-15% depending on the application [1]. There are few applications where such a performance gain would have greater impact than in the launch propulsion field. Figure 1.2 illustrates that the performance (as measured by specific impulse, Isp) has peaked for both kerosene and hydrogen fuels and that a 10% increase in specific impulse would have a dramatic impact.

Among the pressure gain combustion technologies available, the rotating detonation engine (RDE) is receiving the most attention because these devices utilize a conventional feed system, and do not require any high speed valving/rotor to achieve pulsed combustion performance. Research on RDEs began approximately 60 years ago [2, 3]. Lu and Braun [4] reviewed the 60-year-history of RDE research and development and pointed out several challenges including transient mixing, detonation-turbulence, and cooling.

With regard to rocket application, the 2006 paper by Bykovskii et al. [5], enhanced interest in RDE research in our group due to demonstrated pressure gain (Isp gain) for a number of rocket propellant combinations. Modern high speed measurement technologies permit accelerated development of the technology. Although the idea and its potential has had a long history, the path leading to its feasibility has recently

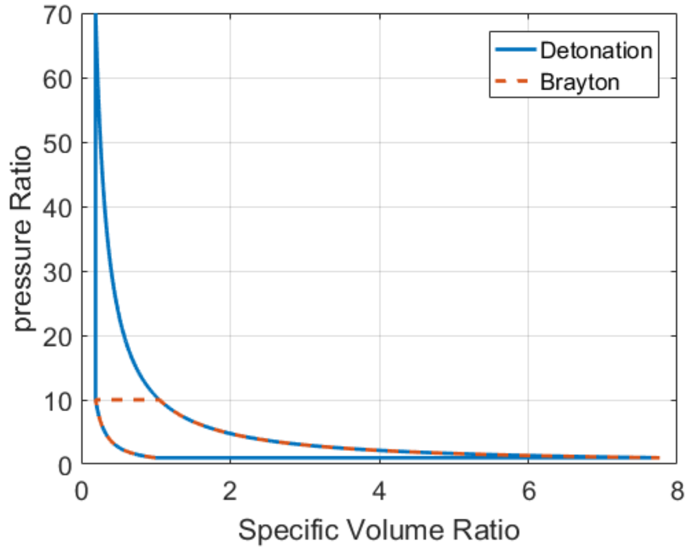


Figure 1.1. The thermal efficiency comparison between a Detonation cycle and a Brayton cycle with stoichiometric methane and oxygen and the initial gas compression ratio of 10

seen many advances. The strides made in technology, such as additive manufacturing, have made it possible to design unconventional injectors that may be a requirement to realize this concept.

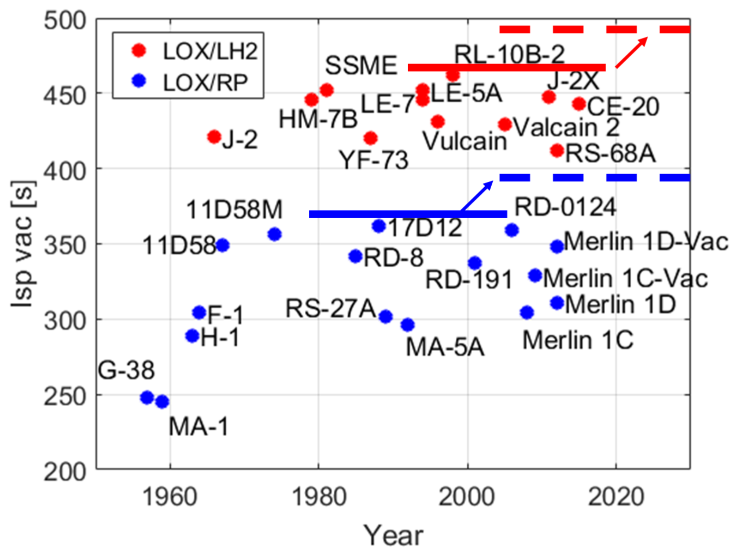


Figure 1.2. Summary of Isp values for launch vehicle engines using kerosene (blue symbols) and hydrogen (red symbols) propellants with potential for 10% gain noted.

## 1.2 RDE operation

Several shapes of RDE combustors have been proposed and tested. The most common RDE has an annular shape combustor shown in Figure 1.3 [6]. The micro nozzles inject either premixed propellants or fuel and oxidizer separately into the combustion chamber axially. The detonation wave travels in the azimuthal direction and the combusted gas is exhausted from the nozzle-end axially.

Figures 1.3 and 1.4 illustrate the combustion field created in an idealized RDE combustor. Fresh reactants are injected vertically upward in Figure 1.3 and the detonation wave moves around the annular combustor at speeds of 1500-2000 m/s. The "unwrapped" view of the combustor in Figure 1.4 illustrates that passage of the high pressure detonation gases temporarily stops the flow of fresh reactants into the chamber. As reactant flow recovers, these gases contact hot product gases. Along this contact surface, the potential for parasitic deflagration (contact surface burning) exists. To maximize performance of the combustor, parasitic deflagration must be minimized as this combustion occurs at relatively low pressure far from the detonation front. For this reason, an excellent understanding of the transient behavior of the injection system is required to achieve optimum performance.

In general, the combustor can support multiple detonation waves if the fill velocities of the reactants are high enough. The combustor size, reactant mass flow, pressure of injection and detonation, and propellant combination all play a role in setting the number of waves, the detonation wave velocity/strength, and the overall performance of the engine.

Another feature in Figure 1.4 is the oblique shock propagating downstream axially from the upper edge of the detonation wave front. If the combustor is long enough, product gases traveling axially downstream from the detonation region may intercept this oblique shock one more time, which causes an additional stagnation pressure loss. Expansion waves form behind the detonation front to equilibrate pres-

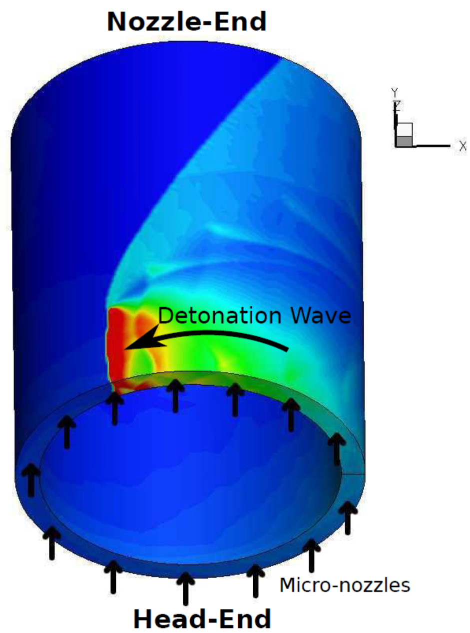


Figure 1.3. Typical annular RDE combustor simulation [6]

sure. These waves propagate not only azimuthally but also axially upstream. Also, another oblique shock forms upstream of the detonation front.

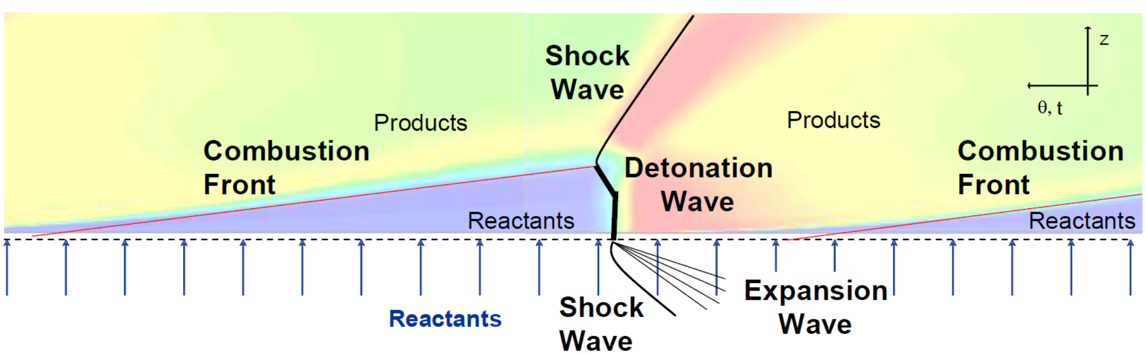


Figure 1.4. Unrapped RDE combuster [6]

High pressure detonation gases significantly influence the transient injector flow near the detonation front, and in some cases, back flow into the injector manifolds can occur. These injector dynamics are strongly influenced by the pressure drop accross of injectors. High pressure drop (stiff) injectors can reduce the back flow and the effects of the high pressure disturbance, whereas lower pressure drop (soft) injectors are easily affected by the detonation. However, stiff injectors require more pressure budget for injection. Transient mixing is promoted by stiffer/higher velocity injection, but the potential exists to mix too quickly and realize parasitic deflagration prior to detonation wave arrival. These complex dynamics provide a significant challenge to the designer and in general the optimal pressure drop for a given engine configuration is not well known.

The pressure disturbance propagating into a manifold keeps travels upstream as an acoustic wave and reflects back from upstream boundaries such as choked flow paths, blades of turbomachinery, and other structures. In some cases the response of the injectors is related to the inlet design and the wave attenuation level affects the injector dynamics. For example, in the Purdue RDE [7] shown in Figure 1.5, the pressure fluctuation created by the detonation wave propagates into both oxidizer and fuel manifolds. The pressure perturbation in both manifolds is rapidly attenuated due to the large area change along the paths. However, even small perturbations in propellant flows are amplified by their large energy release upon combustion as is well known to the combustion instability community. The effects of the injector dynamics and wave attenuation in the injector have not been investigated in the RDE platform with a focused study. The primary objective of this work is to investigate these effects using a multidimensional, time-accurate CFD platform.

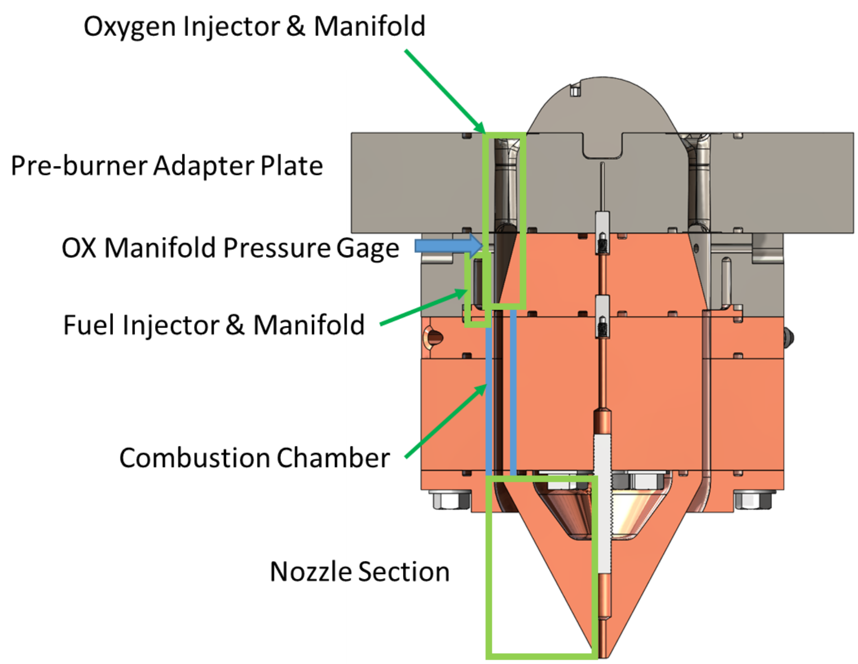


Figure 1.5. A sectional view of the Purdue RDE [7]

## 1.3 Studies of RDE Injector Dynamics

Many researchers around the world have developed CFD models to simulate RDEs with different focus. Some researchers utilized the 2-D unwrapped wave-based computation which was first developed by Paxson [8], to investigate combustors' performances and some injector analysis. Recently, some groups have developed three dimensional models that include injection, mixing, and combustion as coupled processes.

Gaillard [9] simulated a single set of an impinging oxygen and hydrogen injector with an unsteady LES 3D CFD, a 2D CFD approach, and the periodic boundary condition for taking the neighboring injector effects into account, in order to investigate unsteady mixing behavior of the injector. The 2D results exhibited the back flow of the burnt gas into the injector. The 3D results clearly illustrated that the mixing process of these two propellants with the

t gas was a dynamic process and the mixing efficiency varied over time and the axial length

Researchers in the Naval Research Laboratory utilized unwrapped 2D and 3D inviscid CFD simulation to investigate the effect of injector set up in CFD [10–12]. In Ref [10] three types of ideal injectors and a type of a micro injector were simulated. Although the results from the three continuous injectors were similar, the micro injector case had some differences from these continuous injectors: the pressure feedback to the injector manifold, dead zone, detonation structure, shear layer and oblique shock, and detonation propagation along the azimuthal direction. Even though very little back flow was observed, the injector quickly recovered in the micro injector case when compared to the continuous injector cases. The authors suggested that the ideal cases over-predicted the back flow time. They also mentioned an unclear fish–scaled pattern evolving from interactions of the detonation wave with the multiple jets. The jets also tended to obscure the shear layer and oblique shock structures described in the classical view in Figure 1.4. The authors also indicated that the detonation front "jumps" from a given micro injector jet to the next jet.

Schwer and Kailasanath [11] investigated feedback effects in different injector configurations. The authors extended their computational domain into the premixed gas manifold in two 2D cases and examined the injector manifold length effects. A snapshot of pressure gradient field of their shorter manifold case is shown in Figure 1.6. The high peak pressure produced by the detonation wave propagated into the mixture plenum, reflected at the upstream boundary (a constant stagnation pressure and temperature boundary), and went back to the chamber. However, the back flow into the mixture plenum due to the detonation was not observed in all of their cases. The authors claimed that the axial manifold length produced only minor differences in the peak pressure in the slot micro injector configuration.

However, Figure 1.7 clearly indicates that the peak pressure between the two manifold cases varied by roughly 4 atm (10% of the peak pressure) in some peaks. This peak pressure change might have originated from the injector dynamics. As seen in Figure 1.6, the reflected wave arrives at the injectors where the next detonation wave is closely located. Here, the premixed fuel inside the injectors might be compressed by both the detonation wave and the reflected wave so the injected mass flux near the injectors could have been different. Two other injectors were investigated in the paper: one was a cylindrical micro injector and the other was a pintle injector. The injector checked-off region was smaller than the slot injector case and the region after the detonation was different from the slot injector cases. The pintle injector case had no turbulence structure and detonation cell structure. In terms of performance,a higher area ratio (softer injector) produced greater specific impuls and more pressure fluctuation in the mixture plenum.

In Ref [12], the authors studied five different angled micro injectors, and three different shape micro injectors. The pressure feedback to the mixture plenum and the chamber pressure varied with the injector designs. The injector design also affected performance parameters such as thrust and specific impulse. A recent publication by

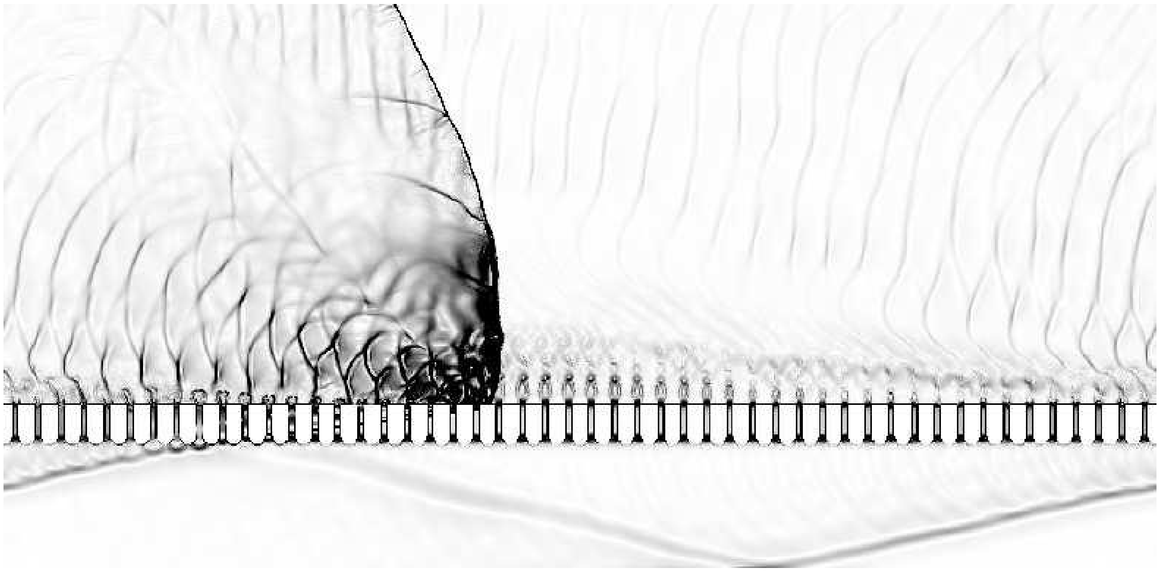

Figure 1.6. Instantaneous pressure gradient for the slot micr-injector simulation. Pst=10 atm, Tst=300K, L=100 mm, l=282.7 mm, a=0.2 [11]

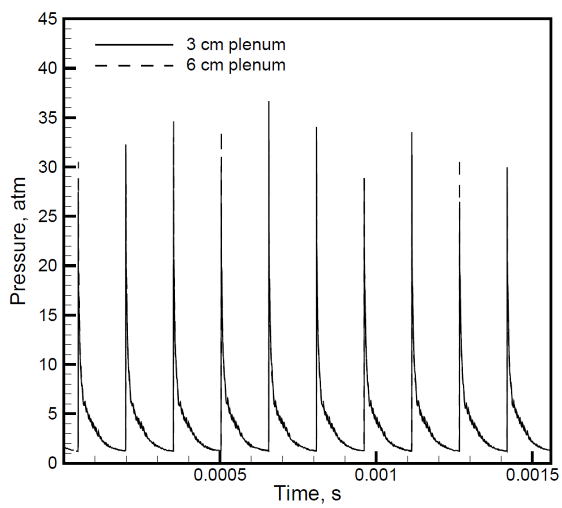


Figure 1.7. Instantaneous pressure gradient for the slot micr-injector simulation. Pst=10 atm, Tst=300K, L=100 mm, l=282.7 mm, a=0.2 [11]

Schwer and Kailasanath [13] presents a simulation that contains an RDE connected to a ram jet to evaluate pressure perturbation propagation in the diffuser section. A 2D Euler RDE combustion computations with slot micro injectors was utilized. The resultant force pressure function was fed into a FEM-FCT solver to compute the diffuser pressure distribution. The pressure variation in the diffuser inlet plane in the single wave case was greater than that of the two wave case since the expansion waves in two wave cases interacted with the high pressure peak and reduced it by a greater extent than in the single wave case. More work needs to be done to evaluate the variation effects to the inlet performance, but Ref [13] clearly indicates that pressure waves from detonations can propagate upstream. Ref [10–13]imply that injector response is affected by the design of the injector and that detonation strength and the resultant response eventually affects the performance of the RDE.

Researchers at the Russian Academy of Sciences also published important CFD results for the injector dynamics in RDEs. Frolov et al. [14] computed a 3D non-premixed air-hydrogen RDE with an upstream isolator. Their turbulence model was the standard k-$\epsilon$ model using a single step hydrogen chemical reaction scheme. The particle method was used for micromixing and turbulence-chemistry interactions. The existence of back flow and pressure feedback into the injector manifold were clearly observed. The chamber peak pressure fluctuated every cycle and was also affected by the prescribed inlet pressure. Due to the chamber pressure fluctuation, the manifold pressure also varied. In Ref [15], the authors carried out a similar simulation and reported 15% increment in stagnation pressure with their proposed upstream isolator. These papers also support the importance of injector dynamics.

Researchers at the United Technologies Research Center and the Air Force Research Laboratory (AFRL) performed the highest fidelity simulations published in literature thus far [16,17]. They modeled the AFRL air breathing RDE [18] and these simulations employed an improved detached eddy simulation (IDDES) hybrid RANS-LES approach based upon the one-equation Spalart-Allmaras turbulence model. A 7-species 7-step hydrogen-air chemical mechanism [19] was employed. They compared their 3D results to 2D and 3D Euler simulations and also evaluated wall effects (slip/non-slip and adiabatic/isothermal) in 3D computations. The specific impulse in the Euler computation was higher due to the deflagration. Viscous effects near wall decreased the Isp significantlyand the isothermal wall caused a further decrease. In Ref [17], the researchers extended their computational domain and included both fuel and oxidizer injectors and their manifolds. The back flow of the combusted gas (water vapor) into the fuel injectors was clearly captured in this paper and presented in Figure 1.8. The authors also pointed out that the high pressure caused by the detonation front propagated into the region upstream of the air injector.

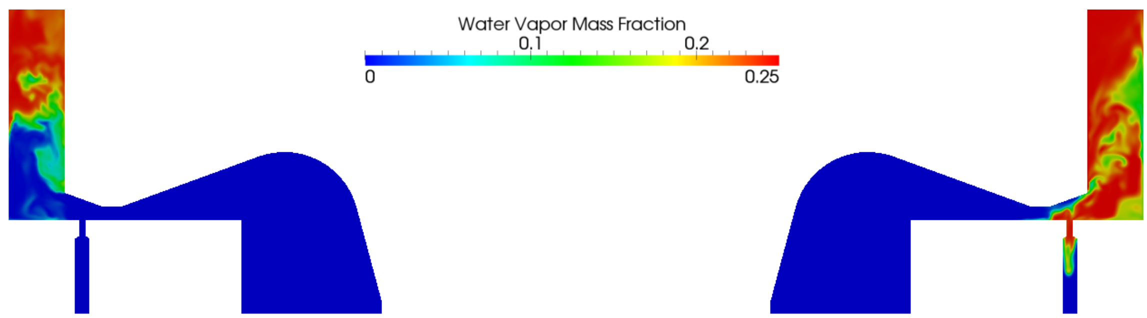


Figure 1.8. Instantaneous water vapor mass fraction contours, comparing snapshots just after the wave has passed by (right) and after a period (slightly less than 0.5 wave revolutions) of recovery (left) [17]. The computational model was developed from the AFRL RDE geometry [18]

Other researchers also reported the back flow and manifold pressure variation due to the high pressure of the detonation front. Paxson et al. [20] presented premixed quasi-2D inviscid CFD results (which contained axial area variation for a nozzle) and compared them with experimental results. Capillary tube averaged pressure (CTAP) from experiments along the axis of the RDE generally agreed with the computed pressure along the axis of the RDE. They also pointed out that there was back flow in one simulation case. Strakey et al. [21] performed an "engineering" level non-premixed RDE simulation. Their target RDE models were a part of the AFRL and

National Energy Technology Laboratory (NETL) RDEs. Fluent with the standard k-$\omega$ turbulence model and the tuned Arrhenius model which had been adjusted by 1D detonation, were utilized. The model was consist of the combustion chamber and both the fuel and air injector manifolds. The back flow of combusted gas into the fuel injectors was also confirmed. Chenglong et al. [22] conducted a 3D Euler equation with 7-species 8-reaction chemical model to assess non-premixed H2-Air RDE. They included both air and fuel injector manifolds into their computational domain. They reported pressure oscillations in both manifolds.

Additionally, authors suggested that injector dynamics contribute to the bifurcation of a detonation wave. Yao and Wang [23] utilized 3D Euler RDE(premixed H2-Air) computation with one-step Arrhenius chemistry to investigate the number of waves in an RDE combustion chamber. They mapped linear pre-detonator simulation results to the RDE chamber as the RDE computation's initial condition to achieve multiple detonation ignition. In the single- and double-wave cases, just after the ignition, the detonation wave(s) propagated in one direction azimuthally while a separate shock wave originating from the ignition traveled in the opposite direction and collided with the detonation wave. The superposition of the shock and detonation waves resulted in the former becoming weakened while the latter continued to propagate. In the four ignition case, a stronger shock wave collided with a detonation wave. The shock wave eventually strengthened a detonation wave propagating in the same direction as the detonation wave. This resulted in a total of eight waves in the detonation chamber. The injector response near the primary detonation front was related to the bifurcation process.

back flow and pressure disturbance propagation into the injector manifolds has been observed experimentally [24, 25]. Lim et al. [24] evidenced the back flow due to the high pressure at the detonation with their liquid injector test facility in 2015. Bedick et al. [25] examined the linear model of the NETL RDE (which is quite similar to the AFRL RDE). Pressure measured at both manifolds showed fluctuations. High speed Schlieren images shown in Figure 1.9 clearly captured the back flow of the combustion gas into the fuel and air injector manifolds, and the pressure shocks and its reflections inside the air injector manifold caused by the detonation high pressure. The shock which propagated into the air manifold interacted with the walls in a complex manner.

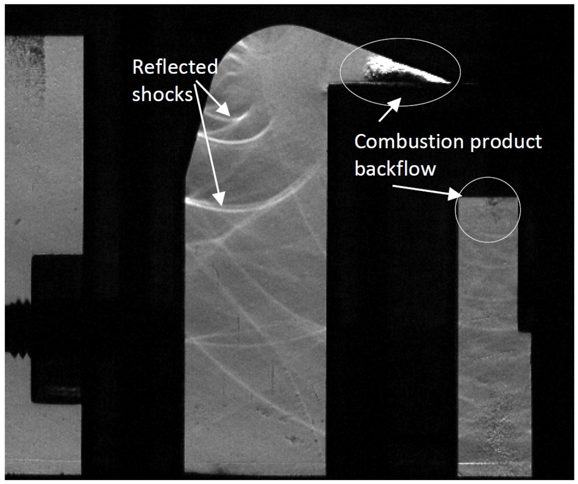


Figure 1.9. High speed Schlieren image, t = 0.01216 sec, 0.55 mm air gap, 300 slpm air, no helium [24, 25]

The literature demonstrates that manifold response contributes significantly to detonation waves topologies, and combustion products penetrated into the manifolds in some cases. Some of the studies examined the geometry and configuration of injectors but did not examine injector dynamics. The relationship between detonation strength and injector dynamics requires investigation and the dynamics of gaseous propellant injectors in RDE environments have not been studied in an organized manner. Specifically, the wave attenuation along the injector axis needs to be explored. Injector response studies are not only helpful for the design of injectors but are also crucial in the development of RDE technology.

## 1.4 Studies of Non-Premixed Detonation Wave Characteristics for RDEs

Previously, non-premixed 3D [16, 17, 26–31], premixed 2D [10, 11, 14, 15, 23], and non-premixed 2D [10–13, 15, 22] RDE CFD simulations were performed and revealed the combustion characteristics and the performance of RDEs. Non-premixed 3D RDE CFD with injectors and nozzles was preferable for revealing the performance of RDEs by providing detailed information of the flow field. Specifically, full 3D simulation with a skeleton chemistry mechanism performed by Lietz et. al. [26] predicted the number of waves in the chamber similar to that observed in experiments and also some detailed phenomena such as the existence of unburnt fuel just behind a detonation wave. This study demonstrated that high-fidelity CFD with a relatively-detailed chemical mechanisms was required to correctly predict RDE performance using simulations. Furthermore, Lietz et. al. [31] investigated the effects of a geometrical throat at the end of the combustion chamber with a nozzle with their 3D simulation model. Although their simulated wave velocity and pressure agreed with the corresponding experiments, the simulated thrust and specific impulse were over-predicted.

The transient mixing characteristics of a given injector design play a strong role in detonation strength and topology and hence have been the subject of study in the community. On this path, several simulations in 2D and 3D were performed to investigate the effects of various injector configurations [9, 32–35] implemented as initial conditions. Gaillard et. al. [9] performed a 3D injector mixing LES CFD simulation for a pair of impinging injectors flowing gaseous hydrogen and oxygen. Figure 1.10 illustrates their simulation results. The equivalence ratio contour is presented in Figure 1.10(a) and the mixing efficiency along the y-direction of the figure was defined as Equation 1.1 in order to quantify the mixing between the fuel and oxidizer:

$$\eta_{mix,\rho} = \frac{\iint_{\mathrm{S_y}} (\rho Y_{\mathrm{H_2}}/max(\Phi, 1))d\mathrm{S}}{\iint_{\mathrm{S_y}} (\rho Y_{\mathrm{H_2}}/mix(\Phi, 1))d\mathrm{S}} \tag{1.1}$$

where $\rho$, $Y_{\mathrm{H_2}}$, $\mathrm{S_y}$, and $\Phi$ represented the density, mass fraction of hydrogen, the considered section (at a y location), and the equivalence ratio respectively. A single mixing efficiency value at the considered location $S_y$ was computed with Equation 1.1 and the value of $\eta_{mix,\rho}$ was varied in the range [0 1]. The computation revealed that the mixing efficiency did not reach unity at the most well mixed region (far side from the injector surface) even in the established state (steady state) with this injector design. More importantly, the mixing efficiency started with a non-zero value due to the recirculation of products.

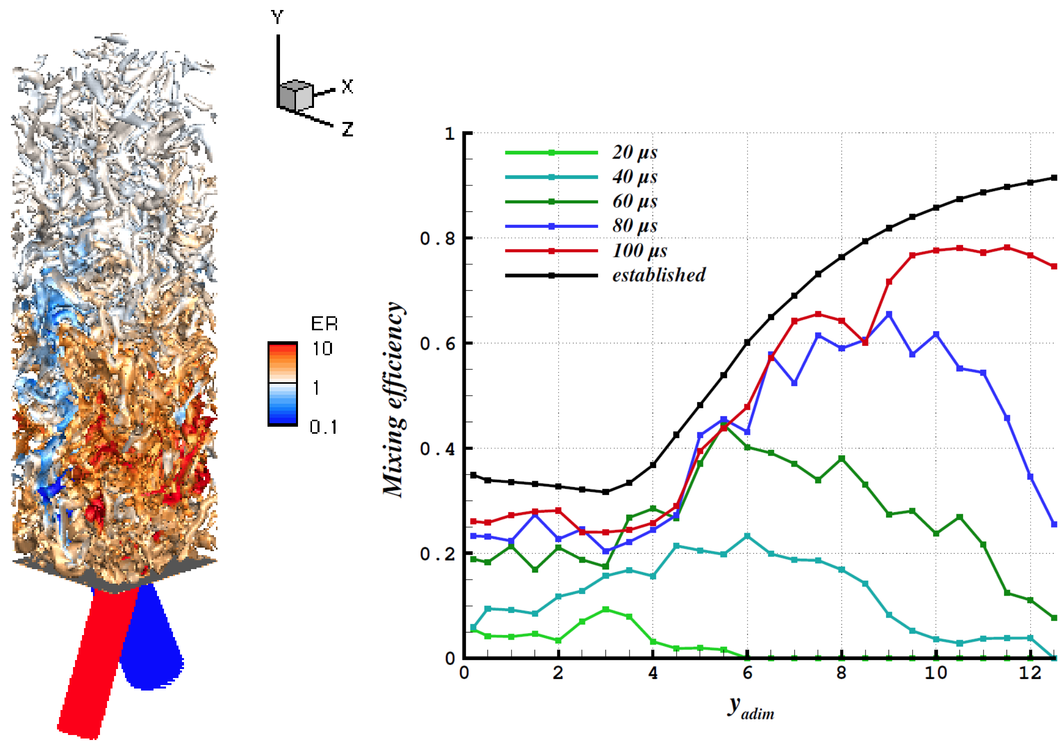


(a) Equivalence ratio contour (b) Mixing efficiency profiles

Figure 1.10. 3D Equivalence ratio contour and mixing efficiency profile. [9]

Fujii et. al. [32] investigated the detonation wave behavior in a non-premixed fuel ($C_2H_4$), oxidizer($O_2$), and product gases($CO_2$ and $H_2O$). They simulated in a 2D rectangular domain shown in Figure 1.11. Repeating non-premixed fuel, oxidizer and product gases bands were located along the horizontal axis and the spacing of the bands were $200\mu m$, $600\mu m$, and $600\mu m$, respectively. A planar detonation wave propagated along the horizontal axis as shown in Figure 1.11. They reported that there were large amounts of unburnt fuel and oxidizer behind the detonation wave and the detonation wave velocity of this non-premixed case was reduced to 2351m/s from the CJ detonation velocity 2377m/s.

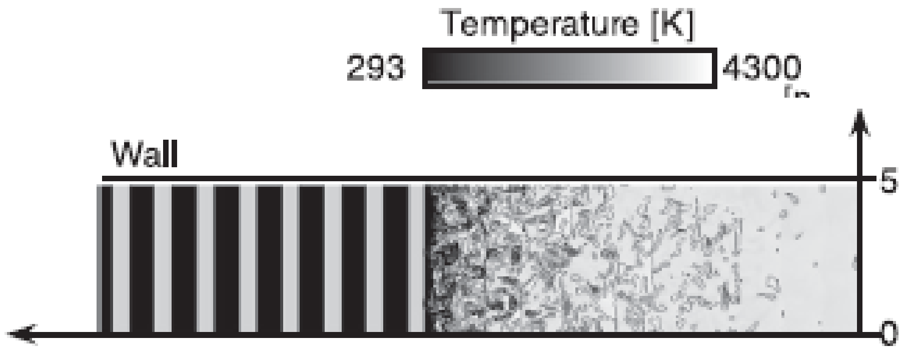


Figure 1.11. Temperature contour snap shot [32]

Researchers from the University of Michigan [35] also performed several similar simulations to reference [32]. Three different initial stratification cases were computed with a 3D DNS solver and a 9-species 19-reaction hydrogen-air mechanism. The smallest and largest stratification cases were presented in Figure 1.12(a). In their results, specifically in their pressure distribution presented in Figure 1.12(b), there were multiple pressure peaks whose values varied with the initial stratification. In addition, their results suggested that smaller stratification enhanced combustion.

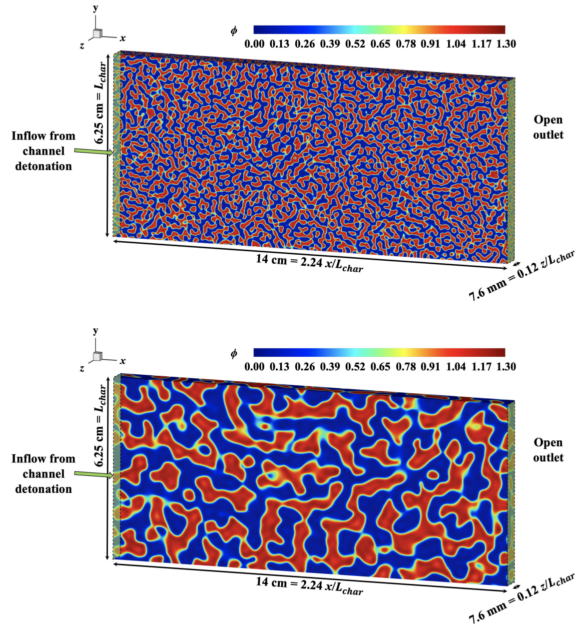


(a) Initial equivalence ratio contours: (top) small stratification case and (bottom) large stratification case

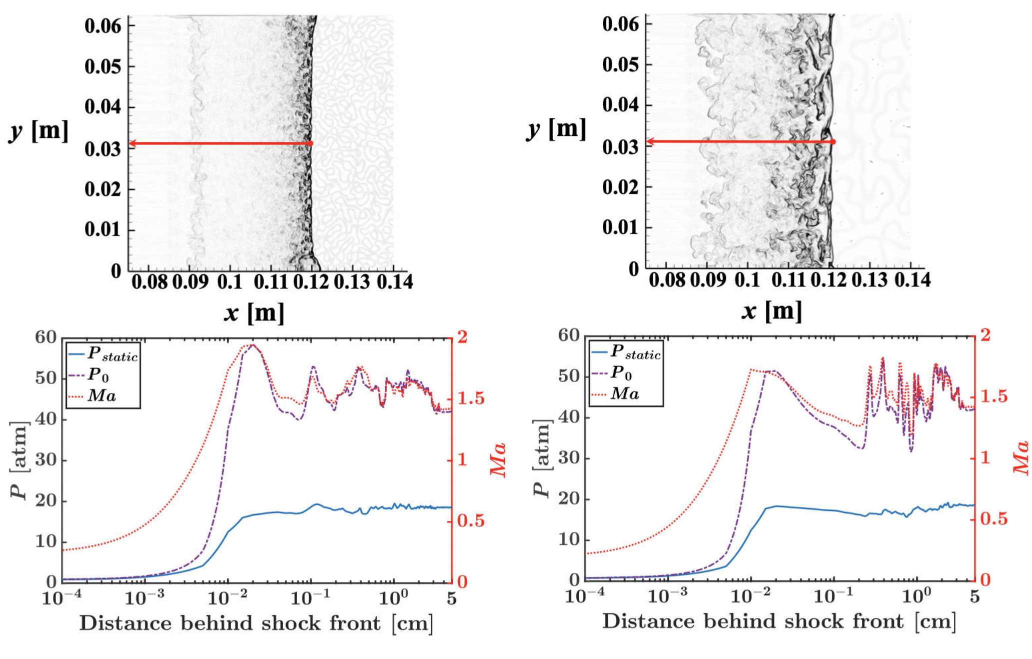


(b) Simulation results : (left top) the numerical Schlieren image of the small stratification case, (right top) the numerical Schlieren image of the large stratification case, (left bottom) the pressure and Mach number distribution of the small stratification case,and (left bottom) the pressure and Mach number distribution of the large stratification case,

Figure 1.12. 3D Equivalence ratio contour and mixing efficiency profile. [35]

## 1.5 Research Objectives and Approach

In an ultimate model, mixing, combustion and fluid flow interactions need to be accounted for in a 3-D unsteady manner, but the expense involved can be prohibitive. Additionally, lower order tools are needed to aid in the preliminary design process. Apart from the time scales and resolution required to capture the important phenomena, this expense is also a direct result of the close coupling between the RDE and the feed system.

Most RDE combustors are based on a combination of a large annular convergent oxidizer/air inlet duct that may include a number of radial or transverse fuel jets upstream of the combustor as illustrated in Figure1.5. In many applications, the area ratio of the annulus is sufficient to physically choke the flow, but in airbreathing applications low area ratio inlets are of interest as the pressure drop is lower than the choked alternative. The convergent/choked annulus is expected to serve a twofold purpose: 1) to accelerate the flow and promote mixing, and 2) to attenuate pressure disturbances from the detonation wave passage so as to establish a limit cycle behavior responsible for the operation of the RDE. While the first objective has been examined in literature [36, 37] the latter has seen limited attention. The 3D injector dynamics study is intended to address this gap in the development of an RDE injector understanding. The response of both fuel and air/oxidizer passages to the passage of a detonation wave is a fundamental dynamic process associated with the device and a well-designed system will need to consider appropriate matching of fuel and air/oxidizer response in order to operate successfully. Optimization of this response will allow the design to achieve the performance promised by the concept of RDE. Since most existing devices employ circular fuel holes, one might argue that a simple 1-D dynamic study of these fuel orifices as they respond to transient chamber pressures might be a reasonable initial approximation to the fuel-side response. However, for the annular air/oxidizer passage, the transverse relief of the detonation wave overpressure is surely important and for this reason a transient 3-D analysis is required. In order to support design of RDE combustors, a parametric study needs to be conducted to provide a top level characterization of annular injector response times under a variety of channel shapes and for a variety of detonation overpressure impulses in order to provide an approximate tool for assessing dynamic behavior of the channel. For these reasons, a parametric study has been conducted to assess the influence of the wave shape on the transient response of this element of the RDE system.

The previous research related to non-premixed detonation reveled important components in an RDE's operation. However, in a real RDE, mixing efficiency and effects of injector spacing affect the propagation of the detonation wave. Additionally, it is challenging to compute the large range of the length scale and time scales of an RDE. The propellant combination of methane and oxygen is also rarely studied in this context. In this non-premixed detonation part of study, it is assumed that the mixing efficiency and the injector spacing can be changed freely for the purpose of performing parametric studies of their effects on the detonation of gaseous methane and oxygen. A majority of RDEs for rocket application have an annular combustion chamber, thus an RDE combustor is unwrapped in the azimuthal direction into a 2D rectangular domain as similar to reference [32], in order to reduce parameters and perform multiple simulations in a reasonable amount of time on Purdue University's RCAC clusters. Also, turbulence is neglected for the same reasons. The parametric injector spacing computations address the minimum number of injectors required so as to reduce the cost and complexity of a chamber's design. The mixing efficiency and the injector spacing is aimed to provide an ideal mixing efficiency and injector spacing of RDE design.

Chapter 2 provides a description of the models and boundary conditions employed in the studies. Chapter 3 presents results from the injector dynamics modeling efforts and Chapter 4 provides the results of non-premixed detonation simulations. Chapter 5 concludes this document and provides proposed follow-on efforts for future work.

# 2. MODEL

## 2.1 CFD Solver

The CFD code, General Equation and Mesh Solver (GEMS), being used in this study was developed over a 20 year period by Prof. Charles Merkle's research group at UTSI and Purdue University [38, 39]. It is a fully coupled, implicit dual time solver with second order accuracy in both space and time. The thermodynamic and transport properties are modeled based on piecewise polynomials that are validated with tabulated data for up to 6000 K [40]. The mixture properties are then estimated using rules due to Bird and Mathur [41].

The present study deals with discontinuities not only present with shocks, but also with chemical kinetics. It is generally recognized that such problems require numerical schemes with more artificial dissipation included either explicitly or implicitly through the order of discretization. In the present study we choose either first or second order accurate schemes for spatial discretization while maintaining a first order accuracy in time [42,43]. The time step chosen is further verified to have insignificant impact on the results, thereby demonstrating the adequacy of the chosen numerical setup. GEMS can handle supersonic and subsonic outlets, and pressure at a supersonic outlet is calculated with the input boundary pressure using ghost cells [39]. The pressure on a subsonic outlet boundary is applied at the interface between the boundary cell and the ghost cell [39]. The ghost cell solutions such as pressure, the three components of velocity, static temperature, turbulence kinetic energy, and specific turbulent dissipation rate, are computed from the user defined condition at the interface and the boundary cell values. The solver then computes the boundary cell value for the next time step. For the supersonic pressure outlet, the code does not require any user defined value at the boundary since all the flow characteristics are outgoing.

## 2.2 Injector Dynamics Study

### 2.2.1 Computational Model

Figure 2.1 shows a schematic image of an RDE and a computational domain. The computational domain is a convergent annulus representing an oxidizer manifold in a topology similar to many of the current RDE research combustors. The computational domain terminates at the injector/chamber interface, i.e. at the injector throat. The simulations and geometry have been inspired to some degree by the RDE experimental facility developed at Purdue University [7] but efforts have been made to keep the analysis generally applicable to other designs that employ such a topology of oxidizer injection.

In some of the designs, the fuel is injected through a series of radial orifices within the convergent flowpath. This is demonstrated in the cross-section of the Purdue combustor shown in Figure2.1. However, in the present study, the fuel injectors and their potential influence on the manifold dynamics is ignored. This assumption significantly simplifies the geometry and allows efficient, targeted computations of the oxidizer injection process.

There are several important parameters to be taken into consideration. One of these is the contraction area ratio of the injector ($A_{out}/A_{in}$). This value is 0.094 for the baseline case. While representative of the Purdue hardware, this area ratio lies at the lower end of values employed in current/prior designs as there is motivation to run larger area ratios to minimize injection pressure drop. This is particularly applicable for air-breathing combustors, where the pressure drop directly impacts the overall efficiency and translates to significant performance metrics. Larger area ratios are therefore considered in the parametric studies. The outer diameter, the length of the manifold, and the throat width of the baseline case are 98.3mm (3.9 inch), 38.1mm (1.5 inch), and 0.27mm (0.01 inch), respectively.

Pure oxygen is assumed as the injected fluid and a mass flow inflow boundary condition is employed. A constant mass flow rate of $\dot{m} = 0.96 kg/s$ is specified with a static temperature of T=500K. The higher than atmospheric temperature is a typical effluent condition from a preburner used for the supply of oxygen [7]. The small amount of combustion products ($\approx$ 5% of water vapor) present in the oxidizer supply is ignored in the present work.

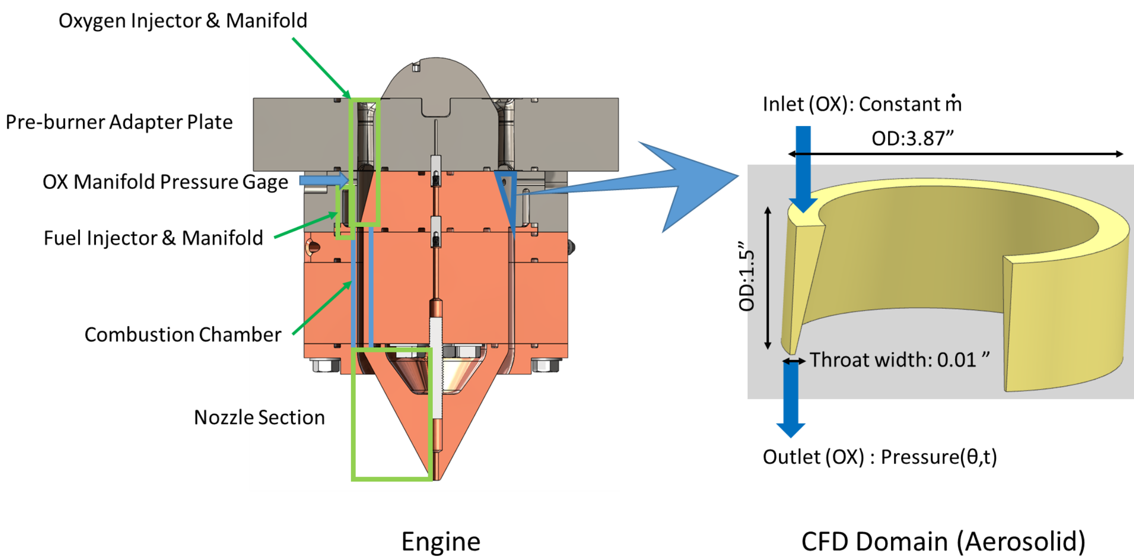


Figure 2.1. Schematic Image of RDE and CFD domain selected to roughly approximate the oxidizer inlet

Side walls are modeled as adiabatic with a non-slip viscous boundary condition. A moving triangular pressure wave is imposed on the outflow boundary to simulate a passing detonation front. The azimuthal extent of the triangular pulse was set to reflect representative measured waveforms [44].While overpressure events from the passing detonation might be closer to an exponential decay, the selected triangular waveform is chosen to simplify and minimize the parameters (chamber height/gap ratio) that would otherwise be required. Additionally it benefits the numerical convergence, which is an important consideration. The largest difference between the calculation domain and the actual test article is the inlet boundary. The computational domain has a constant mass flow inlet that mimics a choked flow condition, reflecting all the incident pressure waves. The experimental condition at the location contains 11 struts as shown in Figure2.2 to support the centerbody within the flow path. The incident pressure waves in the experiment will therefore result in reflections at the walls with the angle of the reflection dependent on the geometry. Mesh complexity and the specificity of the inlet to this particular configuration led us to choose a more generic and simpler flow path. The selected inlet treatment therefore represents a bounding case of perfect reflection. Turbulence effects are modeled using Wilcox's k-$\omega$ model [45]. The closure coefficients in the model are the same as the original reference [45]. While the coupled equations permit usage of an arbitrary equation of state, perfect gas behavior is assumed in this study.

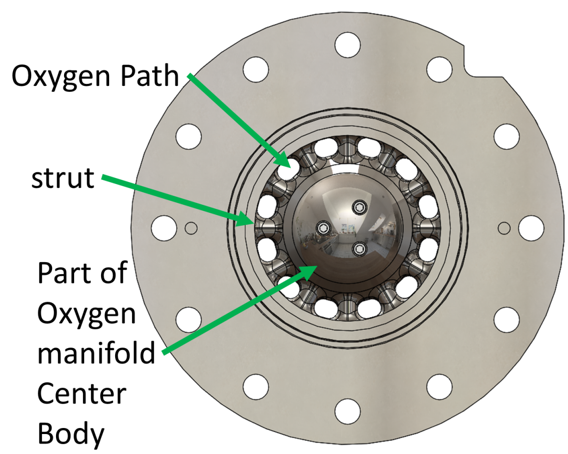


Figure 2.2. The Pre-burner Adapter Plate: the flow path is NOT choked in the actual tests.

A few representative triangular pressure waveforms imposed on the outlet boundary are shown in Figure2.3. Another important parameter is the pressure ratio (PR), defined as the peak pressure divided by the chamber pressure. The azimuthal width of the triangular wave is selected as a third parameter, which is explained further in the next section. A pressure wave velocity of 2000 m/s was assumed based on results from Stechmann et al. [7] and the wave shape was assumed to be invariant. The chamber pressure ($P_{cham}$)is set in 0.25 MPa which is consistent with the experiments [7].

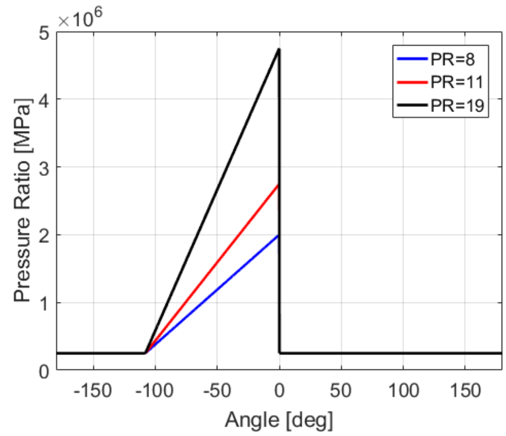


Figure 2.3. Assumed Combustion Chamber (outflow) Pressure Profiles used in the study. Pressure Ratio (PR) is defined as the peak pressure divied by the chamber pressure.

A schematic image of the outlet boundary is presented in Figure2.4. The yellow region corresponds to the imposed pressure impulse. At the beginning of each time step, an angle of a wave front $\theta_{det}$ is computed as Equation2.1. The angle of the wave front is always located at $0 \leq \theta_{det} \leq 2\pi$ and the width of wave,$W_{wave}$ as a fraction of the circumference is a parameter as described before. The back pressure at the outlet boundary, $P_{back}(\theta)$ is computed using Equation2.2.

$$\theta_{det} = \frac{w_s t}{2\pi R} - floor(\frac{w_s t}{2\pi R}) + \pi, \tag{2.1}$$

where $floor$ is the floor function in Fortran.

$$\begin{aligned} &\text{if } \theta_{det} - 2\pi W_{wave} \leq \theta \leq \theta_{det} \text{ then } P_{back}(\theta) = P_{cham} - PR\frac{2\theta}{2\pi W_{wave}} \\ &\text{else } P_{back}(\theta) = P_{cham} \end{aligned} \tag{2.2}$$

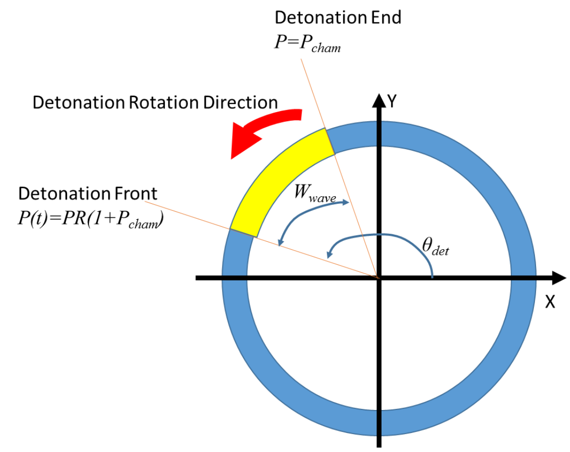


Figure 2.4. Outlet Pressure Boundary and Computation Description for Simulating Detonation Pressure.

The initial condition is obtained from a steady state solution without the imposed pressure wave. The outlet pressure in this case is set at $P_{cham}$. The steep-fronted pressure wave presents a numerical challenge. In order to mitigate numerical difficulties, the input pressure ratio is gradually (0.8MPa) ramped up during every pressure cycle. This approach permitted solution for pressure ratios of up to 19.

### 2.2.2 Mesh Design, Grid Function Convergence, and Time Step Convergence

A grid function convergence study was performed prior to the parametric study. Three mesh resolutions corresponding to coarse, fine, and finest discretization are constructed. Both the resolution and uniformity near the outlet are expected to be sensitive factors, especially along the azimuthal direction. The resolution of the steep pressure gradient created by the imposed pressure wave is dependent on these two factors. The fine mesh is approximately 15% more refined in the azimuthal and axial directions than the coarse mesh, while the finest mesh is independently refined so as to match the values from literature [16, 17]. The resulting coarse mesh has 1.125 degree resolution for a total of 829440 cells, whereas the fine mesh has 1.000 degree resolution and 1152000 cells. The finest mesh, inspired by a study by Cocks et al. [16, 17], has an average cell size of 0.2 mm in all three directions and a total of 12211200 cells. Figure 2.5 shows all three meshes at the same physical length scale so as to provide a reasonable comparison. In this figure, the smallest cell size of the coarse mesh is 0.79mm along the axis, 0.95mm in the azimuthal and 0.02 mm in the radial direction. The smallest cell size of the fine mesh is 0.49mm along the axial, 0.85 mm in the azimuthal and 0.02mm in the radial direction. The finest mesh has a cell size of 0.2mm along all the three directions. Flow conditions employed in the convergence study were the same as the baseline case of the parametric study. These correspond to a constant mass flow rate of 0.96kg/s with a static temperature of T=500K and an imposed pressure wave with pressure ratio of 8 and an azimuthal extent of 30%.

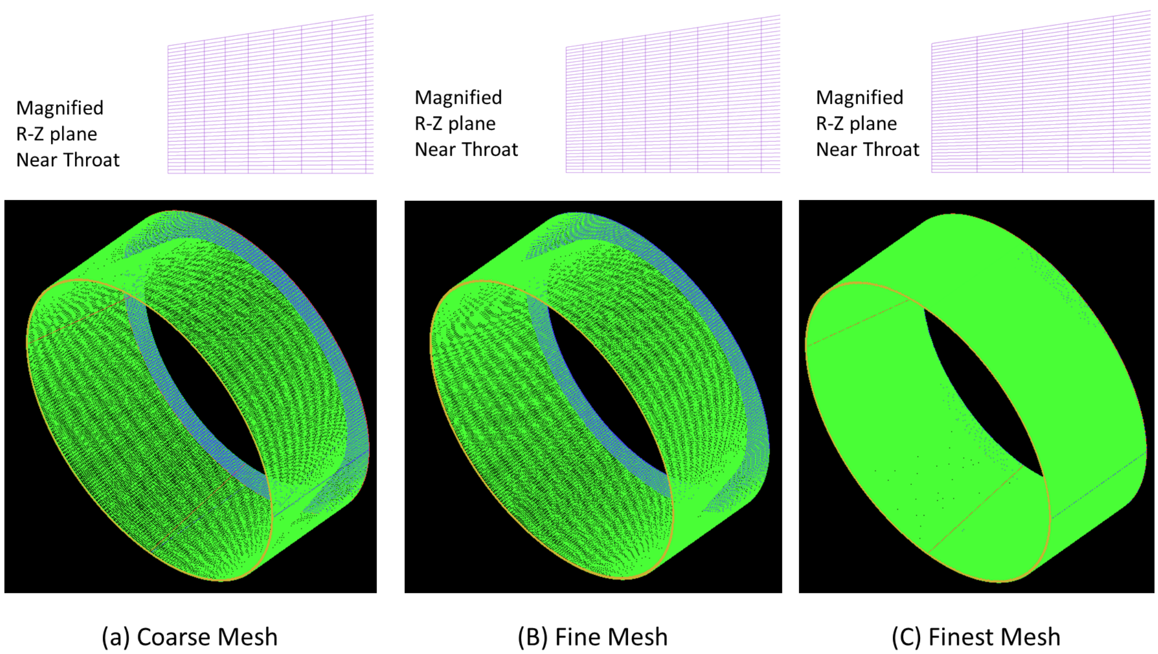


Figure 2.5. Mesh convergence study

To assess the convergence of the solution, it is necessary to attain a limit cycle operation. Figures 2.6(a) and 2.6(b) show the behavior during the transient up to the limit-cycle operation. In Figure 2.6(a), the pressure history at a point that is one cell inside from the outlet boundary is displayed for the fine mesh case. Changes in this pressure from cycle-to-cycle are shown in Figure 2.6(b). This result demonstrates that the pressure at the selected location changes less than 0.1% from cycle to cycle after the 21st cycle, signifying the presence of limit cycle operation.

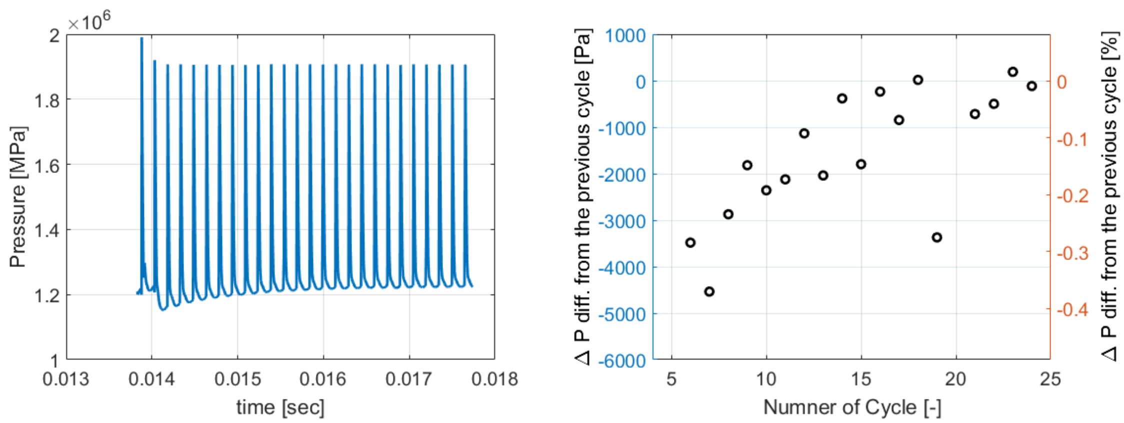


(a) Pressure history at a point one cell inside from the outlet boundary in the fine mesh case

(b) Pressure increment difference over each cycle from the previous cycle

Figure 2.6. Limit cycle behavior.

Figure 2.7(a) compares the imposed and computed pressure profiles near the boundary at a limit cycle condition. As the imposed peak pressure remains greater than that inside the injector and the inlet mass flow remains constant, the injector volume is pressurized. The increase in the mean pressure under such an operation leads to a different overall pressure ratio than the prescribed value. The results with the three levels of mesh refinement are shown in this figure. Quantitative comparison shows that the coarse mesh overpredicts the peak pressure by 4.8% while the fine and the finest mesh results show underprediction of 1.8% and 0.5% respectively. The deviation from the imposed profile is also noted in both the fine and the finest mesh results at other points than the peak pressure. However, the differences in the finest and fine mesh results are relatively small in contrast to the incurred computational cost. Hence the results reported in the remainder of this study utilize the fine mesh, which is a reasonable intermediate choice.

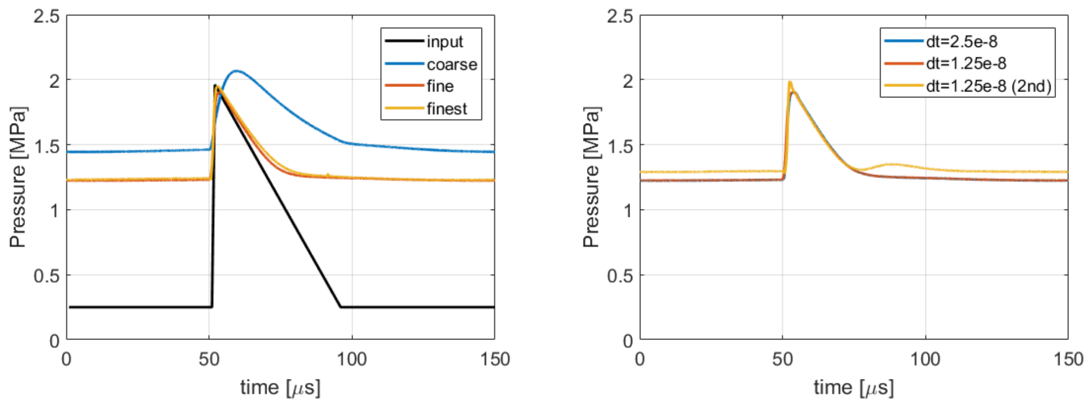


(a) Snapshots of Pressure in the axial direction at the limit cycle; unwrapped at R=1.92inch (the mid-line at the injector throat radius). The input line is the ideal input line and it is shifted to match the peak to the fine mesh peak.

(b) Pressure histories with different time step size in the fine mesh (two lines from the first order method overlap each other).

Figure 2.7. Mesh and time step convergence.

Table 2.1 shows the grid resolution in the three directions – r, $\theta$, and z. The finest mesh differs from the fine in two respects: clustering and maximum cell size. While it significantly improves the latter, the former is forsaken to manage the computational expense incurred. The resulting maximum CFL (Courant-Friedrichs-Lewy) number with respect to the flow speed is shown in Table 2.2. Note that for the same flow field and time step, the higher CFL means better resolution. It is anticipated that the improved resolution in the azimuthal direction will better capture the significant quantity of interest: pressure. It is therefore not surprising that the agreement between imposed pressure and the upstream pressure profile is better in the case of the fine mesh rather than the finest. The discriminating factor in this case is therefore, not the azimuthal but the axial resolution, which is highlighted by the CFL number. The results presented hereafter are therefore obtained with the “fine” mesh, which favors clustering as opposed to limiting the maximum cell size.

Table 2.1. Mesh Resolutions

| | Max Mesh Resolution[mm] | | | Min Mesh Resolution[mm] | | |
|---|---|---|---|---|---|---|
| | R | θ | z | R | θ | z |
| Coarse | 0.25 | 0.97 | 0.68 | 0.25 | 0.79 | 0.07 |
| Fine | 0.22 | 0.86 | 0.57 | 0.22 | 0.7 | 0.07 |
| Finest | 0.22 | 0.21 | 0.21 | 0.22 | 0.17 | 0.21 |

Table 2.2. Max. CFL for flow velocity

| Maximum $CLF_v$ | | | |
|---|---|---|---|
| | R | θ | z |
| Coarse | 0.01 | 2.50E-06 | 0.015 |
| Fine | 0.073 | 7.80E-06 | 0.215 |
| Finest | 0.022 | 6.10E-03 | 0.048 |

As noted previously, the imposed steep fronted pressure wave is numerically more amenable to the first order temporal accuracy and hence it is necessary to perform a time step convergence study. Figure 2.7(b) shows pressure histories of two first order cases with time steps differing by a factor of two. Additionally the smaller of the time steps is repeated with a second order temporal accuracy. It is clearly seen that the higher time step does not notably affect the resultant pressure histories. Furthermore, the second order result is within 8 % of the first order pressures despite the level of detail captured. The first order results appear sufficient to illustrate the major features of the pressure history, while requiring 25% less computational time. This concludes that the time step utilized in this study, $2.5 \times 10^{-8}$ s, is sufficiently small to avoid any impact of the first order accuracy on the results of the parametric variations.

### 2.2.3 3D Injector Dynamics Parametric Study

There are many parameters that might affect to the injector dynamics and parametric studies are suitable in this situation. Table 2.3 shows the major parameters of this parametric study. Case 0 is the base line condition and it is compared with Case1 to observe the length effect. Cases 1, 4, and 8 have identical input impulse values with different shapes. In these cases, the input pressure ratio and the azimuthal extent of high pressure region are adjusted to achieve the identical impulse value. These cases allow us to investigate the effect of the impulse shape. Cases 1, 2, and 3 are for evaluating the effects of the input pressure ratio. Their azimuthal extent are identical whereas the input pressure ratios are varied to simulate different strength of detonation.

Table 2.3. Parametric Study Conditions

| Case No. Name | Pressure Ratio PR= $P_{peak}/P_{cham}$ [-] | Wave Length λ[%] | Area Ratio $A_{out}/A_{in}$[-] | Outer Rad. R [inch] | Length L [inch] | Number of Waves N[rot] | Input Impulse $I_0$ [Pa·s] |
|---|---|---|---|---|---|---|---|
| 0. Base PR=8 | 8.0 | 30 | 0.094 | 1.9350 | 0.38 | 1 | 33.8 |
| 1. Long PR=8 | 8.0 | 30 | 0.094 | 1.9350 | **1.5** | 1 | 33.8 |
| 2. Long PR=11 | **11.0** | 30 | 0.094 | 1.9350 | **1.5** | 1 | **50.6** |
| 3. Long PR=19 | **19.0** | 30 | 0.094 | 1.9350 | **1.5** | 1 | **95.6** |
| 4. Small Dia. | 8.0 | **60** | 0.094 | **0.9675** | **1.5** | 1 | 33.8 |
| 5. Same I PR=4.5 | **4.5** | **60** | 0.094 | 1.9350 | **1.5** | 1 | 33.8 |
| 6. Two Wave | 8.0 | 30 | 0.094 | 1.9350 | **1.5** | **2** | 33.8 |
| 7. Wider Gap PR=19 | **19.0** | 30 | **0.186** | 1.9350 | **1.5** | 1 | **95.6** |
| 8. Same I PR=15 | **15.0** | **15** | 0.094 | 1.9350 | **1.5** | 1 | 33.8 |
| 9. Two Wave PR=19 | **19.0** | 30 | 0.094 | 1.9350 | **1.5** | **2** | **95.6** |

The inlet geometry is an important design parameter evaluated in this study. Injector aspect ratio and area ratio variations are considered in this study. The injector aspect ratios (height and diameter) are assessed by contrasting results from Cases 1 and 4, and area ratio (i.e. injector contraction ratio) effects by comparing Cases 3 and 7. Finally, the number of waves affects the manifold dynamic response and Cases 6 and 9 assess the effects in the low and high pressure, respectively. These two cases are comparable to the identical pressure input single wave cases such as Cases 1 and 3.

## 2.3 Non-premix Detonation Study

### 2.3.1 Computational Model

This parametric study focuses on the effects of the injector spacings and the mixing efficiencies for an RDE combustor. As explained in Chapter 1, ultimately all of the components (the injectors, combustor, and nozzle) represented in a coupled 3D simulation with a detailed chemical kinetics mechanism will provide a solution representative of the actual engine. However, the computational expense involved is not affordable at the current time and at any level of research. A typical strategy is therefore to separately analyze the components. Among these, the RDE combustor can be further simplified by unwrapping and considering it as a 2D rectangular domain. The x and y axes in such a domain represent the azimuthal and axial direction of the RDE combustor. The RDE combustor size considered for this study is similar to that studied experimentally at Purdue University [46]. The detailed computational domain and conditions are explained in latter part of this section.

The Purdue RDE experiment [46] uses methane and oxygen as the propellants. For these propellants, more than a dozen of chemical kinetics mechanisms are available. A prime consideration, however, is the computational cost associated. A detailed chemical kinetics mechanism such as the GRI [47] mechanism, can more than double the cost of a non-reacting flow. In order to obtain a good accuracy with reasonable computational cost, FFCM-Y mechanism [48] is chosen in this study. This mechanism is smaller than the other kinetics models for $CH_4$ and $O_2$ combustion and has small difference in terms of the ignition delay compared with the established models. This is shown in Figure 2.8, which is computed with the kinetics solver Cantera [49]. This mechanism is utilized by Lietz et al. [26] in their 3D simulations, which correctly predicted the number of waves and the wave velocity. In the current setup, Euler equations are utilized for simplicity, which is consistent with literature [32].

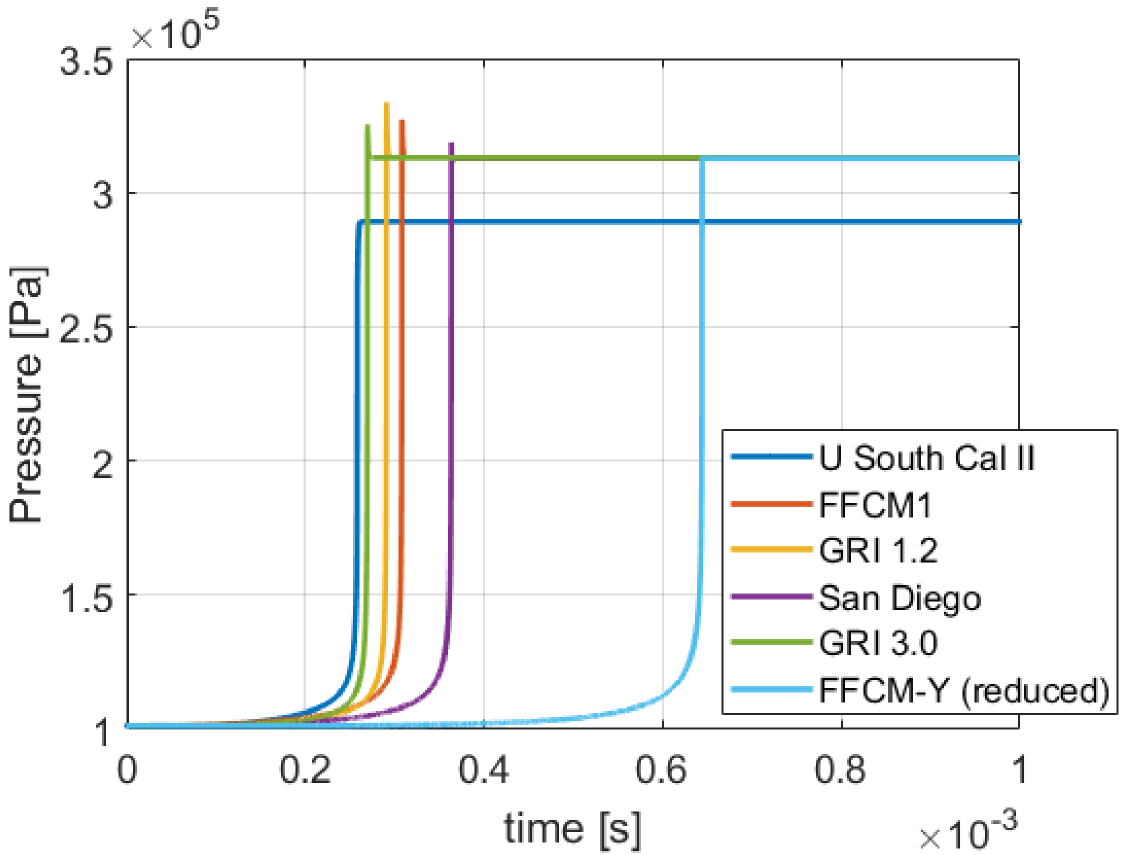


Figure 2.8. Pressure history of constant pressure combustion with Cantera [49] with different mechanisms: initial temperature and pressure are 1500 $K$ and 1 atm

The computational domain is rectangular as presented in Figure 2.9; the x and y directions of this domain represent the azimuthal and axial directions of the unwrapped annular RDE, respectively. The domain can be thought to include three regions: driving, run-away, and target. The driving section is initialized with gases at high pressure, temperature, and velocity to generate a planar detonation wave. The state of the driving section is based on a snap shot of the detonation tube result from Section 2.3.3 and presented in Table 2.4. This driving section creates a planer detonation wave propagating in the x-direction mimicking the azimuthal propagation in a RDE. The zone "runway" has a uniform, stationary mixture of the reactants at the same pressure and temperature as the target section. The purpose of this zone is to attain a steadily propagating, coupled detonation moving towards the "target" zone. The initial pressure, temperature, and velocity of the target and runway zones are 48263 $Pa$ (7 psi), 354 $K$, and 0 $m/s$, respectively. The mass fractions in the runway zone correspond to fully premixed propellants with an equivalence ratio of unity.

The mass fractions of the target zone is computed for various assumed mixing efficiency profiles as described below. All boundaries except the left boundary are treated as inviscid slip walls whereas the left boundary is defined as a non-reflective pressure outlet, which is representative of an infinitely long domain. The outlet pressure is set to an arbitrary low value that guarantees that the boundary behaves a super sonic pressure boundary. Thus, this non-reflective supersonic pressure boundary does not influence the solution within the target region. However, due to a large initial pressure ratio, this boundary condition implies supersonic outlet and therefore truly non-reflecting condition. Table 2.5 summarizes the initial conditions of the runway and target sections with the wave front values in the driving section.

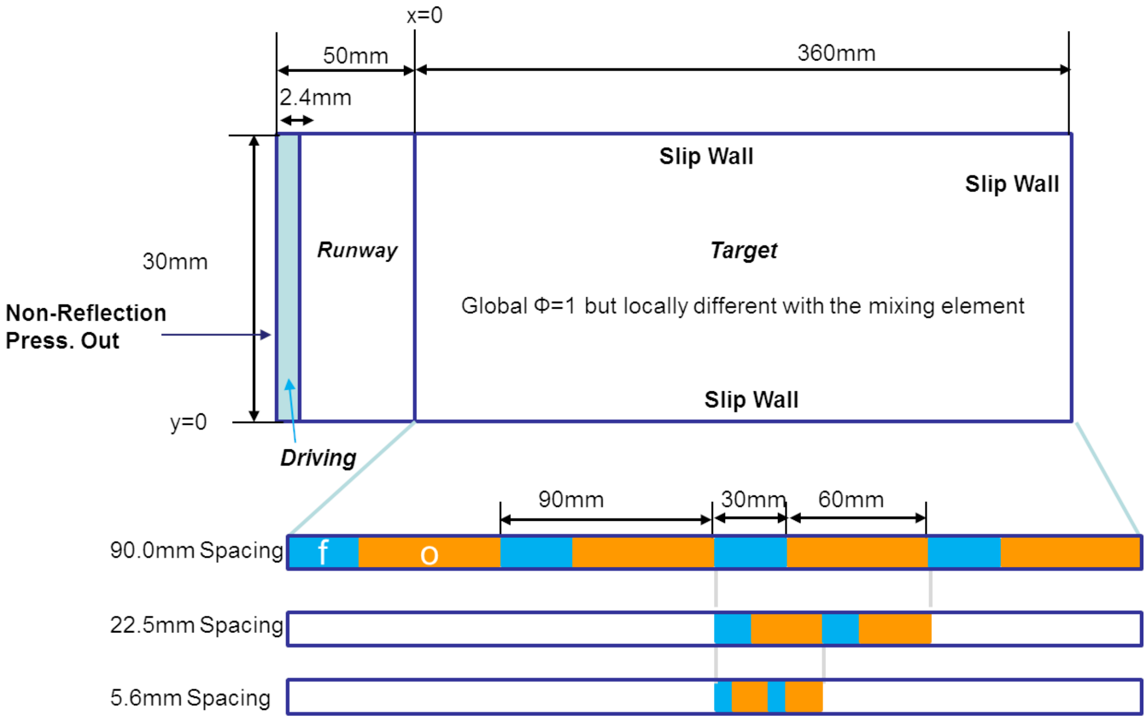


Figure 2.9. Computational Domain

There are two effects considered herein - that of discrete injection of the propellants and axially varying mixtures based on specific injector designs. The target zone is therefore azimuthally (x-axis) divided into fuel and oxidizer regions to imitate "injectors" as shown in Figure 2.9. The fuel to oxidizer length ratio in the x-direction is kept constant at 1 : 2 and Table 2.6 presents the actual sizes. The spacings of the injectors for this study are chosen to be in geometric proportion, starting at 360mm and decreasing with a ratio of 2 to 180, 90, 45, 22.5, 11.3, and lastly 5.6 mm. In the y-direction (the axial direction of the RDE), a mixing efficiency is assumed and is the subject of parametric studies for gaseous methane and oxygen propellants. In the limit, the injection process can be highly inefficient, leading to fully non-premixed propellants within the fill zone. The other extreme is the fully premixed condition. In between these two limits, the mixing efficiency defined by Gaillard et. al. [9],

Table 2.4. Initial simulation conditions in the driving section

| | x=-0.0499 | x=-0.0497 | x=-0.0495 | x=-0.0493 | x=-0.0491 | x=-0.0489 | x=-0.0487 |
|---|---|---|---|---|---|---|---|
| pressure [Pa] | 1.16E+06 | 1.16E+06 | 1.17E+06 | 1.17E+06 | 1.17E+06 | 1.17E+06 | 1.18E+06 |
| velocity in x [m/s] | 1.09E+03 | 1.09E+03 | 1.09E+03 | 1.09E+03 | 1.09E+03 | 1.10E+03 | 1.10E+03 |
| velocity in y [m/s] | 0.00E+00 | 0.00E+00 | 0.00E+00 | 0.00E+00 | 0.00E+00 | 0.00E+00 | 0.00E+00 |
| temperature [K] | 3.56E+03 | 3.56E+03 | 3.56E+03 | 3.56E+03 | 3.56E+03 | 3.56E+03 | 3.56E+03 |
| mass fraction of $H_2$ | 7.64E-03 | 7.65E-03 | 7.65E-03 | 7.65E-03 | 7.65E-03 | 7.65E-03 | 7.66E-03 |
| mass fraction of H | 2.72E-03 | 2.72E-03 | 2.72E-03 | 2.72E-03 | 2.73E-03 | 2.73E-03 | 2.74E-03 |
| mass fraction of $O_2$ | 1.27E-01 | 1.27E-01 | 1.27E-01 | 1.27E-01 | 1.27E-01 | 1.28E-01 | 1.28E-01 |
| mass fraction of O | 3.75E-02 | 3.75E-02 | 3.75E-02 | 3.76E-02 | 3.76E-02 | 3.76E-02 | 3.77E-02 |
| mass fraction of OH | 1.04E-01 | 1.04E-01 | 1.04E-01 | 1.04E-01 | 1.04E-01 | 1.04E-01 | 1.04E-01 |
| mass fraction of $HO_2$ | 2.75E-04 | 2.75E-04 | 2.75E-04 | 2.76E-04 | 2.76E-04 | 2.76E-04 | 2.76E-04 |
| mass fraction of $H_2O$ | 3.02E-01 | 3.02E-01 | 3.02E-01 | 3.02E-01 | 3.02E-01 | 3.02E-01 | 3.02E-01 |
| mass fraction of $CH_3$ | 2.54E-13 | 2.55E-13 | 2.55E-13 | 2.56E-13 | 2.57E-13 | 2.57E-13 | 2.57E-13 |
| mass fraction of $CH_4$ | 2.95E-14 | 2.96E-14 | 2.97E-14 | 2.97E-14 | 2.98E-14 | 2.98E-14 | 2.98E-14 |
| mass fraction of CO | 2.29E-01 | 2.29E-01 | 2.29E-01 | 2.29E-01 | 2.29E-01 | 2.29E-01 | 2.29E-01 |
| mass fraction of $CO_2$ | 1.90E-01 | 1.90E-01 | 1.90E-01 | 1.90E-01 | 1.90E-01 | 1.90E-01 | 1.89E-01 |
| mass fraction of $CH_2O$ | 6.77E-10 | 6.78E-10 | 6.79E-10 | 6.80E-10 | 6.81E-10 | 6.82E-10 | 6.83E-10 |

| | x=-0.0485 | x=-0.0483 | x=-0.0481 | x=-0.0479 | x=-0.0477 | x=-0.0475 | x=-0.0473 |
|---|---|---|---|---|---|---|---|
| pressure [Pa] | 1.19E+06 | 1.21E+06 | 1.28E+06 | 1.42E+06 | 1.54E+06 | 8.77E+05 | 1.34E+05 |
| velocity in x [m/s] | 1.11E+03 | 1.13E+03 | 1.20E+03 | 1.31E+03 | 1.41E+03 | 1.27E+03 | 3.02E+02 |
| velocity in y [m/s] | 0.00E+00 | -1.89E-16 | -1.88E-16 | -1.58E-16 | -8.28E-17 | -1.63E-17 | 1.54E-18 |
| temperature [K] | 3.56E+03 | 3.56E+03 | 3.57E+03 | 3.59E+03 | 3.58E+03 | 2.32E+03 | 7.36E+02 |
| mass fraction of $H_2$ | 7.68E-03 | 7.72E-03 | 7.78E-03 | 7.89E-03 | 8.03E-03 | 8.22E-03 | 1.26E-03 |
| mass fraction of H | 2.75E-03 | 2.78E-03 | 2.83E-03 | 2.91E-03 | 2.99E-03 | 2.46E-04 | 2.02E-07 |
| mass fraction of $O_2$ | 1.28E-01 | 1.28E-01 | 1.29E-01 | 1.29E-01 | 1.38E-01 | 5.57E-01 | 7.93E-01 |
| mass fraction of O | 3.79E-02 | 3.82E-02 | 3.89E-02 | 4.01E-02 | 4.03E-02 | 1.38E-03 | 6.63E-10 |
| mass fraction of OH | 1.04E-01 | 1.04E-01 | 1.05E-01 | 1.07E-01 | 1.06E-01 | 9.62E-03 | 3.53E-06 |
| mass fraction of $HO_2$ | 2.76E-04 | 2.78E-04 | 2.84E-04 | 3.00E-04 | 3.17E-04 | 4.49E-04 | 8.81E-05 |
| mass fraction of $H_2O$ | 3.01E-01 | 3.01E-01 | 2.99E-01 | 2.96E-01 | 2.94E-01 | 1.50E-01 | 9.76E-03 |
| mass fraction of $CH_3$ | 2.58E-13 | 2.62E-13 | 2.68E-13 | 3.06E-13 | 1.67E-06 | 3.56E-02 | 6.24E-03 |
| mass fraction of $CH_4$ | 2.97E-14 | 3.00E-14 | 3.04E-14 | 3.29E-14 | 2.28E-07 | 5.85E-02 | 1.86E-01 |
| mass fraction of CO | 2.29E-01 | 2.30E-01 | 2.31E-01 | 2.33E-01 | 2.45E-01 | 1.27E-01 | 8.96E-03 |
| mass fraction of $CO_2$ | 1.89E-01 | 1.88E-01 | 1.86E-01 | 1.82E-01 | 1.60E-01 | 3.51E-02 | 3.31E-09 |
| mass fraction of $CH_2O$ | 6.86E-10 | 6.95E-10 | 7.31E-10 | 8.16E-10 | 9.75E-07 | 1.14E-02 | 1.94E-03 |

Table 2.5. Simulation conditions for the 2D non-premixed detonation wave

| | Wave front in Driver | Runway | Target |
|---|---|---|---|
| pressure [Pa] | 1536862 | 48263 | 48263 |
| temperature [K] | 3575.6 | 354 | 354 |
| velocity in x and y [m/s] | 1411.4, 0 | 0, 0 | 0, 0 |
| mass fraction of $H_2$ | 0.00803 | 0 | mixing efficiency |
| mass fraction of H | 0.00299 | 0 | mixing efficiency |
| mass fraction of $O_2$ | 0.1378 | 0.7996 | mixing efficiency |
| mass fraction of O | 0.0403 | 0 | mixing efficiency |
| mass fraction of OH | 0.1060 | 0 | mixing efficiency |
| mass fraction of $HO_2$ | 0.0003 | 0 | mixing efficiency |
| mass fraction of $H_2O$ | 0.2938 | 0 | mixing efficiency |
| mass fraction of $CH_3$ | 1.67E-06 | 0 | mixing efficiency |
| mass fraction of $CH_4$ | 2.28E-07 | 0.2004 | mixing efficiency |
| mass fraction of CO | 0.2451 | 0 | mixing efficiency |
| mass fraction of $CO_2$ | 0.1602 | 0 | mixing efficiency |
| mass fraction of $CH_2O$ | 9.75E-07 | 0 | mixing efficiency |

specifically their mass-weighted mixing efficiency, is utilized as one of the profiles. Appropriate changes needed for the initial condition specification are made and the definition of the mixing efficiency at a y location (at a axial location of the RDE engine) is presented as Equation 2.3.

$$\eta_{mix,\rho} = \frac{\sum(\rho Y_{\mathrm{CH_4}}/max(\Phi, 1))}{\sum(\rho Y_{\mathrm{CH_4}}/mix(\Phi, 1))} \tag{2.3}$$

,where $\rho$, $Y_{\mathrm{CH_4}}$, and $\Phi$ are density, mass fraction of methane, and equivalence ratio of a cell, respectively.

Table 2.6. Parametric Study Conditions

| Mixing Efficiency | Injector Spacing | Fuel Inj. | Ox Inj. | Mixing Efficiency | Injector Spacing | Fuel Inj. | Ox Inj. |
|---|---|---|---|---|---|---|---|
| premixed | - | - | - | Gaillard | 360 mm | 120 mm | 240 mm |
| non-premixed | 360 mm | 120 mm | 240 mm | Gaillard | 180 mm | 60 mm | 120 mm |
| non-premixed | 180 mm | 60 mm | 120 mm | Gaillard | 90 mm | 30 mm | 60 mm |
| non-premixed | 90 mm | 30 mm | 60 mm | Gaillard | 45 mm | 15 mm | 30 mm |
| non-premixed | 45 mm | 15 mm | 30 mm | Gaillard | 22.5 mm | 7.5 mm | 15 mm |
| non-premixed | 22.5 mm | 7.5 mm | 15 mm | Gaillard | 11.3 mm | 3.8 mm | 7.5 mm |
| non-premixed | 11.3 mm | 3.8 mm | 7.5 mm | Gaillard | 5.6 mm | 1.9 mm | 3.7 mm |
| non-premixed | 5.6 mm | 1.9 mm | 3.7 mm | poor | 360 mm | 120 mm | 240 mm |
| baseline | 360 mm | 120 mm | 240 mm | poor | 180 mm | 60 mm | 120 mm |
| baseline | 180 mm | 60 mm | 120 mm | poor | 90 mm | 30 mm | 60 mm |
| baseline | 90 mm | 30 mm | 60 mm | poor | 45 mm | 15 mm | 30 mm |
| baseline | 45 mm | 15 mm | 30 mm | poor | 22.5 mm | 7.5 mm | 15 mm |
| baseline | 22.5 mm | 7.5 mm | 15 mm | poor | 11.3 mm | 3.8 mm | 7.5 mm |
| baseline | 11.3 mm | 3.8 mm | 7.5 mm | poor | 5.6 mm | 1.9 mm | 3.7 mm |
| baseline | 5.6 mm | 1.9 mm | 3.7 mm | | | | |

Globally, any given pair of fuel and oxidizer injectors has an equivalence ratio of unity. Locally (either fuel or oxidizer side), the equivalence ratio is computed from a mixing efficiency based on the y location. The equivalence ratio is then converted to mass fractions of methane and oxygen for an initial condition within the target region. The mixing efficiency in this study artificially mimics various designs of an RDE injector. The chosen mixing efficiency profiles are presented in the Figure 2.10. The baseline mixing efficiency is defined as per Equation 2.4. It is an arc tangent function, which gives a zero value or fully non-premixed at the bottom cell (injector surface). At the top, it has a value of unity indicative of fully premixed propellants. Gaillard et. al. [9] simulated mixing with discrete injectors and their result is curve-fitted to give Equation 2.5 and labeled as Gaillard. The poor mixing efficiency profile is obtained as given by Equation 2.6. It is a modification of the baseline profile obtained by doubling the normalized y and truncating at normalized y=1. Additional to these three mixing profiles, the perfectly premixed case and the non-premixed cases are also considered.

$$\begin{gathered} \eta_{mix,\rho,baseline} = 0.5\frac{1 + atan(\bar{y})}{atan(6.0)} \\ \bar{y} = -6 + 0.12 * [y/max(y) * 100] \end{gathered} \tag{2.4}$$

$$\begin{gathered} \eta_{mix,\rho,Gaillard} = 0.5(1 - 0.25)\frac{1 + atan(\bar{y})}{atan(6.0)} + 0.25 \\ \bar{y} = -6 + 0.12 * [y/max(y) * 100] \end{gathered} \tag{2.5}$$

$$\begin{gathered} \eta_{mix,\rho,baseline} = 0.5\frac{1 + atan(\bar{y})}{atan(6.0)} \\ \bar{y} = -6 + 0.12 * [y/max(y) * 50] \end{gathered} \tag{2.6}$$

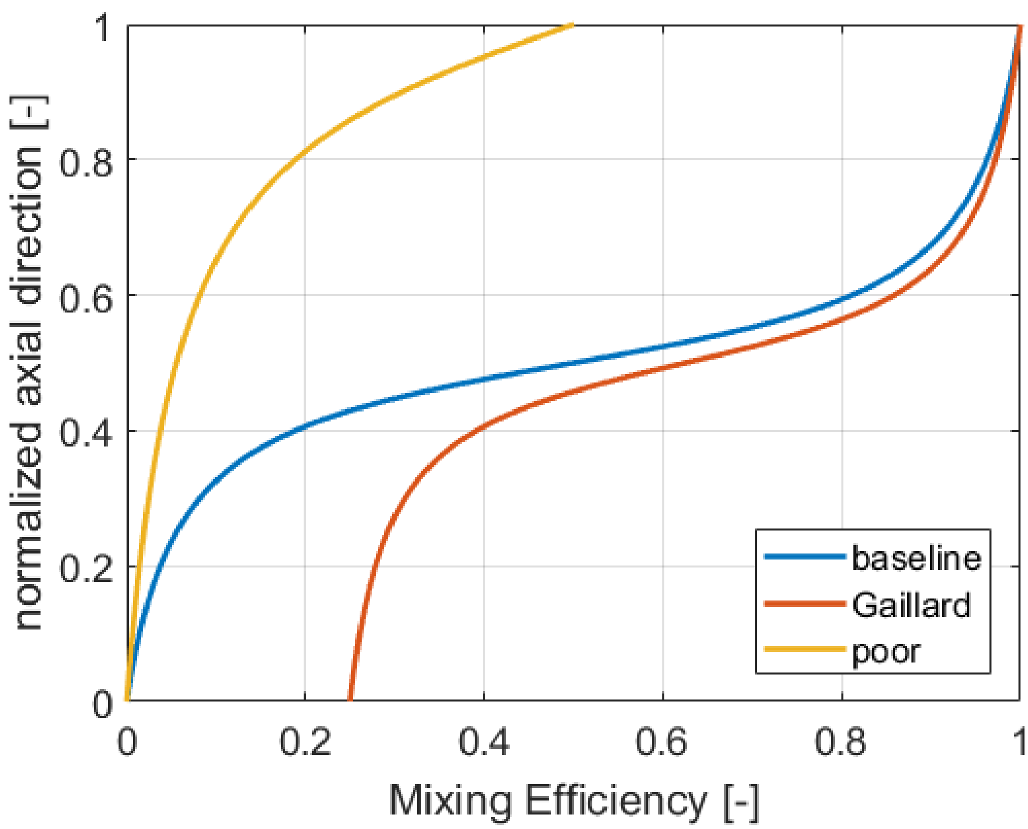


Figure 2.10. Target mixing efficiencies

The procedure that converts the mixing efficiency to mass fractions of the fuel and oxidizer is described step by step below:

1. Select a mixing efficiency profile.

2. For a given y location, compute mixing efficiency ($\eta_{target}$).

3. Guess the initial fuel side oxidizer mass fraction : $Y_{fuel,O_2,guess}$.

4. Compute the fuel side fuel mass fraction as : $Y_{fuel,CH_4} = 1 - Y_{O_2,guess}$. It is assumed that there are no diluents or recirculating combustion products present.

5. Compute the local equivalence ratio for the fuel side using $Y_{fuel,O_2,guess}$ and $Y_{fuel,CH_4}$. Additionally, the mass of fuel ($m_{fuel,CH_4}$) and oxidizer ($m_{fuel,O_2}$) at the fuel side are calculated : $m_{fuel,CH_4} = \rho_{fuel} Y_{fuel,CH_4} vol$ and $m_{fuel,O_2} = \rho_{fuel} Y_{O_2,guess} vol_{fuel}$. $\rho_{fuel}$, and $vol_{fuel}$ are the density of the cell with the initial pressure and the mass fractions ($Y_{fuel,CH_4}$ and $Y_{fuel,O_2,guess}$) and the total volume of the fuel side cells at the y location.

6. Since the global equivalence ratio is assumed as unity, mass of fuel ($m_{CH_4}$) and oxidizer ($m_{O_2}$) in this pair of fuel and oxidizer injectors can be computed with stoichiometric mass fraction of the fuel (0.2004) and oxidizer (0.7996): $m_{CH_4} = vol \rho_{st} 0.2004$ and $m_{O_2} = vol \rho_{st} 0.7996$. $vol$ is the total volume of the set of cells at the y location. $\rho_{st}$ is the density at the stichometric condition with the initial pressure

7. The oxidizer-side mass of fuel ($m_{ox,CH_4}$) and oxidizer ($m_{ox,O_2}$) can be computed by the difference of items 6 and 5: $m_{ox,CH_4} = m_{CH_4} - m_{fuel,CH_4}$ and $m_{ox,CH_4} = m_{O_2} - m_{fuel,O_2}$.

8. Step 7 can be converted as the mass fraction of both fuel ($Y_{ox,CH_4}$) and oxidizer ($Y_{ox,O_2}$) of the oxidizer side: $Y_{ox,CH_4} = m_{ox,CH_4}/(m_{ox,CH_4} + m_{ox,O_2})$ and $Y_{ox,O_2} = m_{ox,O_2}/(m_{ox,CH_4} + m_{ox,O_2})$.

9. Compute the mixing efficiency ($\eta_{computed}$) by Equation 2.3 with values from step 3 and 8 .

10. If step 9 is close enough (order of $10^{-4}$ or less), the mass fractions of the cell is assigned for the initial condition. Otherwise, the steps repeat from step 3 until it satisfies the small error with the bisection method.

Figure 2.11 illustrates the normalized equivalence ratio ($\phi^\star = \phi/(\phi + 1)$ where $\phi$ is the equivalence ratio [50]) contours near the boundary between the runway and the target regions for the four mixing efficiencies with the 22.5 mm injector spacing. For all mixing efficiencies, the normalized equivalence ratio is 0.5 that represents the stoichiometric condition in the runway section (before $x = 1$). The local normalized equivalence ratio varies with the mixing efficiency in the target region.

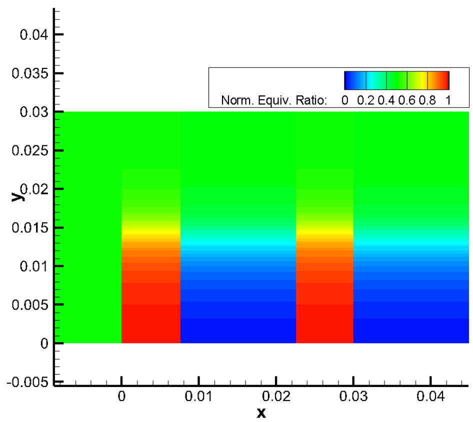


(a) Baseline mixing efficiency

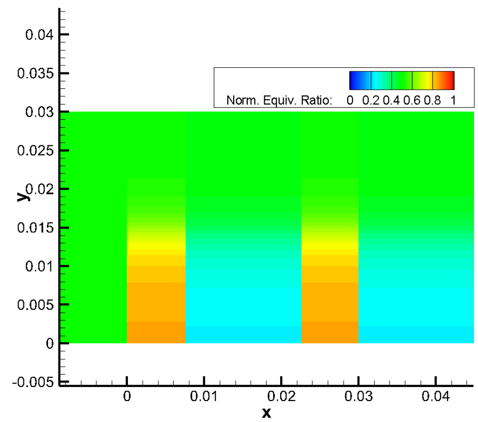


(b) Gaillard mixing efficiency

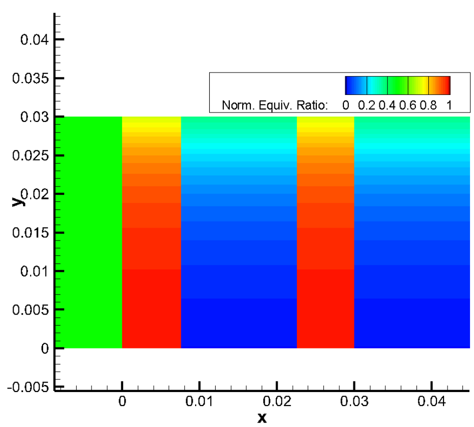


(c) Poor mixing efficiency

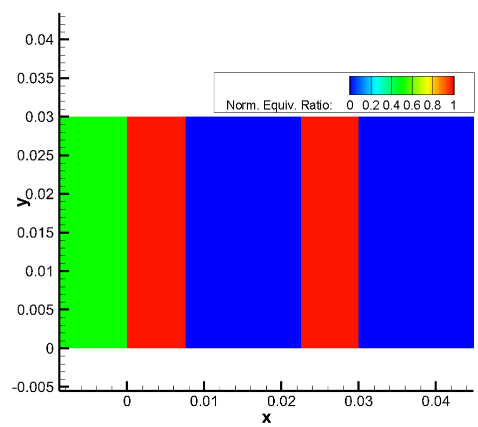


(d) Non-premixed mixing efficiency

Figure 2.11. Normalized equivalence ratio ($\phi^{\star} = \phi/(\phi + 1)$ where $\phi$ is the equivalence ratio [50]) contours near the boundary between the runway and target region for the four mixing efficiencies with the 22.5 mm injector spacing.The normalized equivalence ratio ranges between zero and one: pure oxidizer, pure fuel, and the stoichiometric condition represent 0, 1, and 0.5 respectively.

### 2.3.2 Validation of GEMS for a detonation simulation

The code is validated against available reference data from literature [51] and a prior CFD result [26] before conducting the parametric studies. The experiment consists of a detonation tube that can demonstrates incident shock, its reflection and subsequent deflagration-to-detonation transition (DDT). This case can be simulated as a quasi-one-dimensional case as shown by Lietz et al. [26]. The case is initialized with a part of the tube filled with a quiescent mixture of $H_2$, $O_2$, and Ar with a molar ratio of 2:1:7 at temperature of 298 K and pressure of 0.066 atm. Another section of the tube contains the same mixture at a pressure of 0.362 atm, temperature of 300K and velocity of 465 m/s. Once the computation starts, a shock is formed between the stationary and the moving fluid. Then the shock propagates in the quiescent gas, eventually encountering and reflecting at the end-wall of the tube. The gas between the reflected shock and the wall is compressed and heated twice and the resultant temperature is sufficient to ignite the mixture. The deflagration, on account of the end-wall, transitions to a detonation. The chemical mechanism used for this case of hydrogen-oxygen combustion is a 21 step, nine species mechanism by Li et. al. [52], which is the same as used by Lietz et al. [26].

Table 2.7 shows the shock related parameter comparison between the experimental measurements [51], the CFD result by Lietz et. al. [26], and the current CFD result. It can be seen that the encountered error is reasonable considering neglected multi-dimensional effects and non-adiabatic wall conditions from the experiment.

The experiment and comparison obtained herein is important for another aspect of the study, that of deflagration to detonation transition or DDT. Figure 2.12 presents the peak pressure histories from the measurements obtained by Oran [51], Lietz [26] and the current case. Figure 2.12(a) *sim* Figure 2.12(c) agrees in general with some differences noticeable towards the end of the simulation and beyond the occurrence of the DDT(100 $\mu s$). An important difference between the two CFD cases is the length of the detonation tube, which is shorter in the current case to manage the

Table 2.7. Summary of validation for the shock

| | Experiment [51] | Lietz et. al. CFD [26] | GEMS | Error to ref [26] % |
|---|---|---|---|---|
| P incident wave [atm] | 0.362 | 0.362 | 0.365 | 0.8 |
| T incident Wave [K] | 621 | 631 | 628 | -0.5 |
| $U_{shock}$ of incident wave [m/s] | 754 | 752 | 754 | 0.3 |
| P reflected wave [atm] | 1.3 | 1.26 | 1.29 | 2.4 |
| T reflected Wave [K] | 1036 | 1033 | 1039 | 0.6 |
| $U_{shock}$ of reflected wave [m/s] | 450 | 415 | 414 | -0.2 |

computational expense. The resulting pressure wave from the end of the tube reaches the detonation just as it encounters the peak pressure. However, the two aspects that are of interest, namely shock propagation and deflagration to detonation transition are captured reasonably well in this case, supporting the computational methodology described herein.

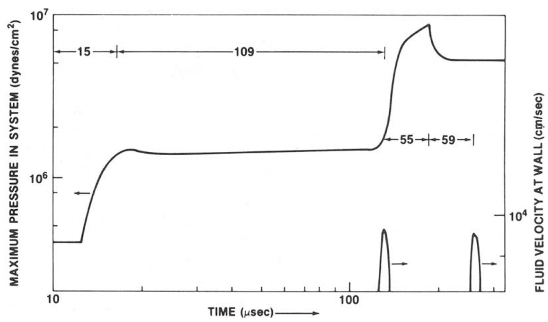


(a) Oran [51]

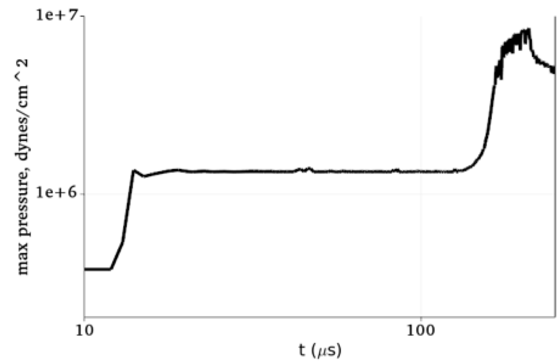


(b) Lietz [26]

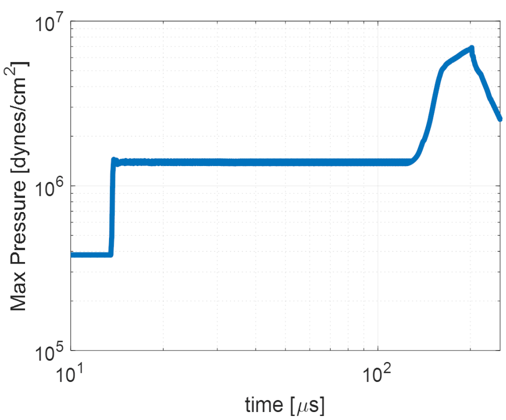


(c) GEMS

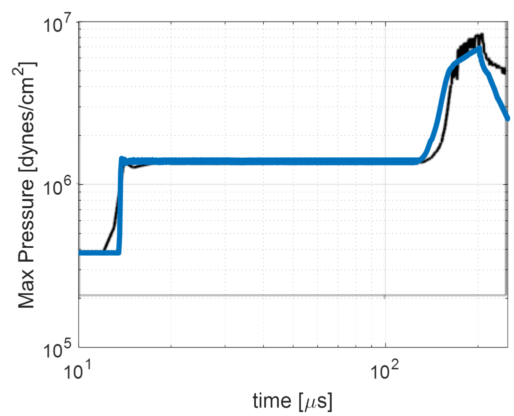


(d) Comparison Lietz [26] and GEMS. The black and purple lines represent Lietz and GEMS, respectively.

Figure 2.12. Peak pressure histories of domain

### 2.3.3 Grid Convergence

The propellants of interest to this study are different than those from the validation case, and hence it is important to demonstrate the adequacy of the spatial resolution chosen. The mesh convergence was performed in a 1m long detonation tube as shown in Figure 2.13. The left hand boundary is defined as an outlet. The Chapman–Jouguet detonation condition computed with the solver Cantera [49] (Shock and Detonation toolbox [53]) is used for this boundary pressure specification. All other boundaries are treated as the slip wall condition. The first 20mm from the left boundary is the driving section and is initialized as the CJ condition from Cantera as shown in the Table 2.3.3. The remaining 980mm is set as a driven section condition described in the Table 2.3.3. The time step chosen was $5.0^{-9}s$, which is equivalent to a CFL number of 0.2 corresponding to the CJ velocity of $2345.5m/s$ for the smallest of the meshes ($62.5\mu m$).

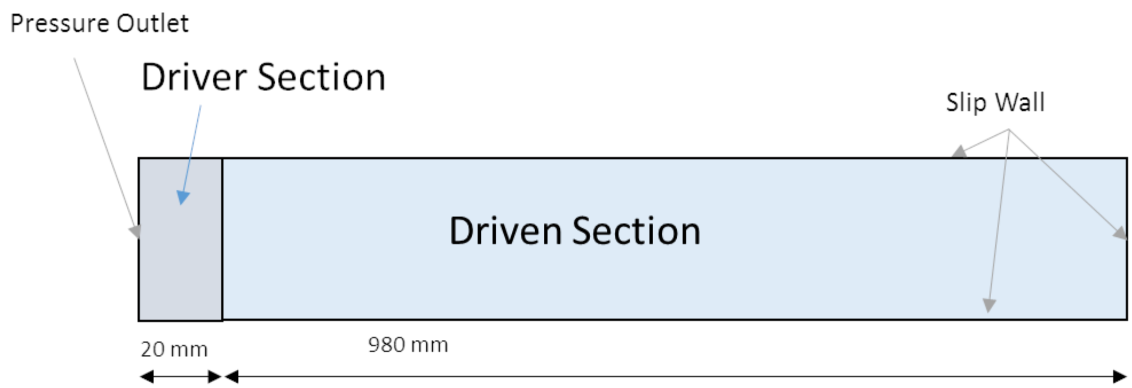


Figure 2.13. Computational domain for 1D detonation tube

Figure 2.14 shows snapshots of the pressure near the detonation front compared with the CJ detonation pressure computed with the Cantera. All meshes with a cell size lower than 250 $\mu m$ show a resolved peak pressure just after the wave front. The magnitude variation of this peak is within 10 %, indicating mesh convergence with respect to the shock induced compression. The pressure beyond the peak decays to the CJ pressure and the relaxation profile is also found to be minimally varying below the computational cell size of 250 $\mu m$. A slightly smaller cell size of 200 $\mu m$ is therefore chosen for the 2D parametric study. The pressure, temperature, velocity, and the

Table 2.8. 1D detonation tube initial conditions

| | Driver Section | Driven Section |
|---|---|---|
| pressure [Pa] | 1153162 | 48263 |
| temperature [K] | 3559.0 | 354 |
| velocity in x and y [m/s] | 1078.3, 0 | 0, 0 |
| mass fraction of $H_2$ | 0.00766 | 0 |
| mass fraction of H | 0.00272 | 0 |
| mass fraction of $O_2$ | 0.1270 | 0.79957 |
| mass fraction of O | 0.0374 | 0 |
| mass fraction of OH | 0.1034 | 0 |
| mass fraction of $HO_2$ | 0.0002 | 0 |
| mass fraction of $H_2O$ | 0.3025 | 0 |
| mass fraction of $CH_3$ | 4.3E-11 | 0 |
| mass fraction of $CH_4$ | 4.9E-12 | 0.2004 |
| mass fraction of CO | 0.2290 | 0 |
| mass fraction of $CO_2$ | 0.1900 | 0 |
| mass fraction of $CH_2O$ | 9.4E-087 | 0 |

mass fraction obtained in this case, from the wave front to 3 mm downstream are utilized as the initial condition for the driving section of the non-premixed detonation wave parametric study described in the chapter 3.2.5.

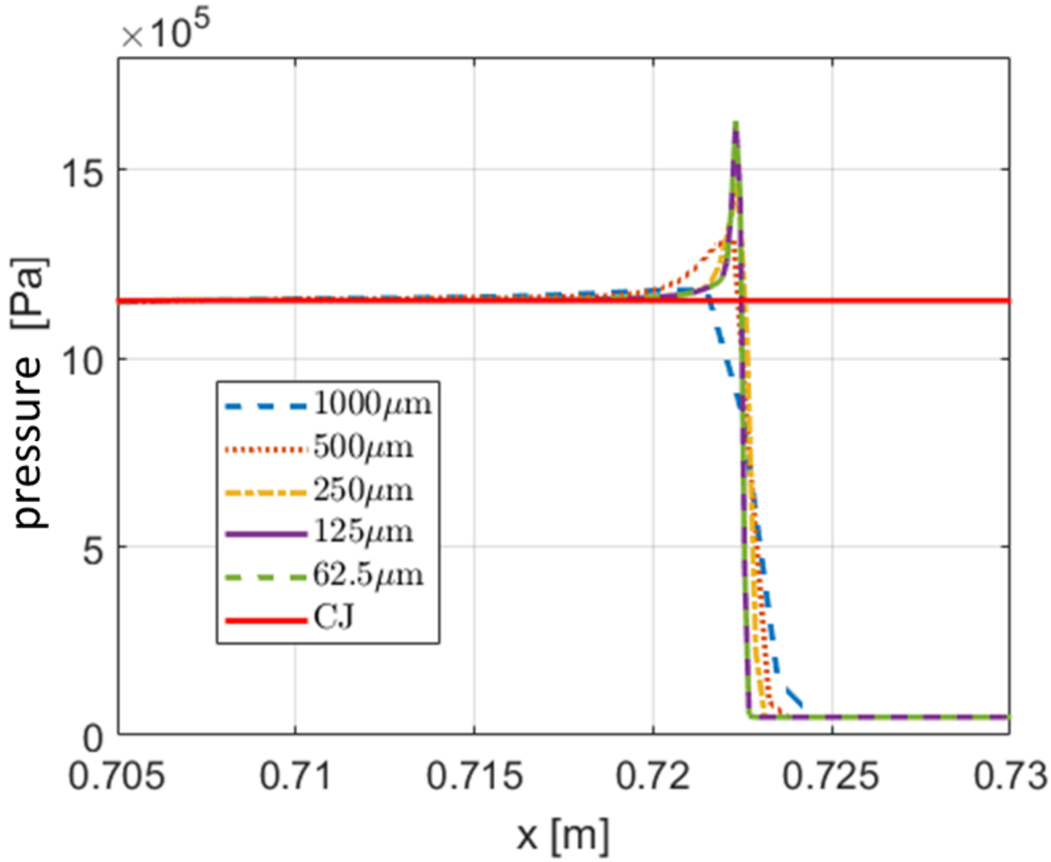


Figure 2.14. Snapshots of pressure profile near the detonation front

# 3. RESULTS AND DISCUSSION FOR OXIDIZER INJECTOR DYNAMICS

The parametric study of the simulations described in Chapter 2 were executed on the Rosen Center for Advanced Computing (RCAC)'s clusters (Rice, Conte, and Carter) at Purdue University. Simulations took roughly from 3 days to 1 month on 200 cores to obtain limit cycle behavior within the manifold. In many cases, this behavior is achieved within 10 cycles. No back flow due to the high pressure impulse is observed for all cases except the wider gap case in the limited cycle. However, in several high pressure input cases, the high pressure wave forces flow reverse in the high pressure region at the exit in their earlier cycles. The back flow behavior of these cases quickly disappears as the cycle goes due to the fact that the manifold is pressurized by the back flow and unchoked flow around the high pressure region since the imposed pressure is kept identical, which might be different from the actual experiments. The wider gap case has back flow after 28 rotations which is in the limited cycle, because of lower manifold pressure.

## 3.1 Baseline Case (Case 0)

A "baseline" configuration was selected to provide a detailed assessment of the behavior such that parametric results could be distilled and simplified. A fairly short inlet was intentionally selected here in order to provide multiple reflections of upstream propagating waves. Recognizing that the mass flow inflow boundary condition behaves as a "hard" surface, this condition provides an upper bound on the amount of reflection of compression waves stemming from the passing detonation event. Figure 3.1 summarizes the geometry for the baseline inlet. As with other cases, a triangular-shaped pressure pulse is employed to simulate the passing detonation. In this baseline case, the maximum pressure is 8.0 times the base pressure and the pulse width corresponds to 30% of the annulus as in Table 2.3 .

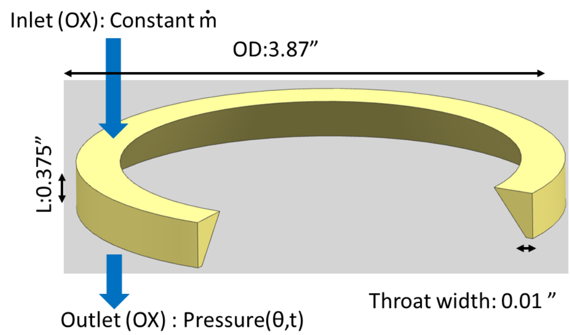


Figure 3.1. CFD domain (aerosolid) of the baseline case

The temporal evolution of pressure contours for this case are shown in Figure 3.2. The model was run for a total of 50 cycles of the detonation wave to remove any memory of the initial condition and establish a limit-cycle behavior. The flow direction is from top to bottom and the imposed waveform is moving in the counterclockwise direction as noted by the arrow in the figure. Here, $t_S$ is the starting time of a cycle defined with a certain angle and the cycle time in this case is approximately $151\mu s$. The disturbance from the applied pressure wave travels upstream and reflects off the inlet boundary. However, the local pressure disturbance generated by this interaction is fairly weak due to the large area contraction and strong pressure gradients that exist in the mean flow.

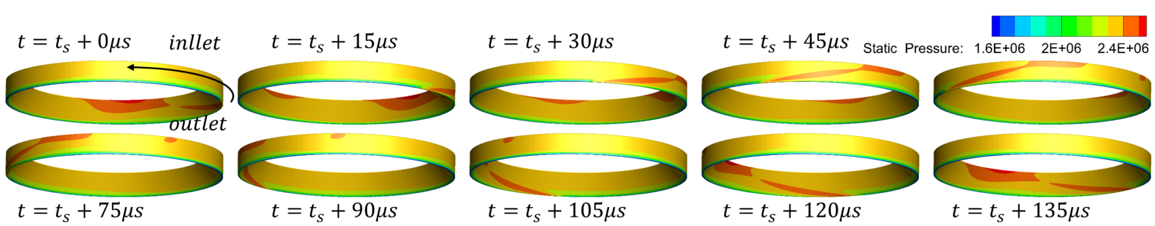


Figure 3.2. Temporal evolution of pressure contours for the 50th rotation of calculation. Here, flow is from top-to-bottom and imposed waveform is in the counterclockwise direction as noted by the arrow.

In order to visualize the manifold pressure fluctuations induced by the waveform, local pressures are normalized by the pressure under a steady flow condition when the outlet pressure is constant as the chamber pressure $P = P_{cham}$(0.25MPa). Figure 3.3 shows the dimensionless pressure fluctuation contours at various instances in time for the baseline case.The contours are displayed as a function of azimuthal location for a point at R=1.92 inch which is the center of the converging annular passage. The flow direction is from top to bottom. The wave is imposed in azimuthal direction from the left to right as shown as the magenta arrow. The black arrow indicates the pressure fluctuation traveling up stream and the yellow arrow represent the downstream reflection wave in Figure 3.3 at $t = t_s + 30\mu s$. The wave is significantly attenuated even at locations very near the exit plane. For example, the red region represents pressures only about 18% above the unperturbed value. There are multiple reflections from both the inlet and outlet. As seen the red arrow in Figure 3.3, the multiple-reflected wave eventually is canceled by the next applied wave. The high pressure fluctuation peak trajectory forms a "ridge" that corresponds the imposed and reflected waves. Since the x-axis is unwrapped angle in the constant radius and y-axis is a normalized axis of the injector, an angle of the ridge from x-axis represents a velocity vector angle constructed with the sonic velocity (a) and axial characteristic velocity (u), i.e. either u+a or u-a. The two angles on Figure 3.3 are computed with the input wave speed (2000m/s), average flow velocity (39.8m/s), and average sonic speed (418.1m/s) and adjust to the aspect ratio of the figure. As the average flow velocity is much less than the sound speed, the approximate result of $tan^{-1}(a/u_{wave})$ closely approximates the angle at which the disturbance propagates. The computed angles agree well with the computed pressure contours since high Mach number region is limited to near the exit.

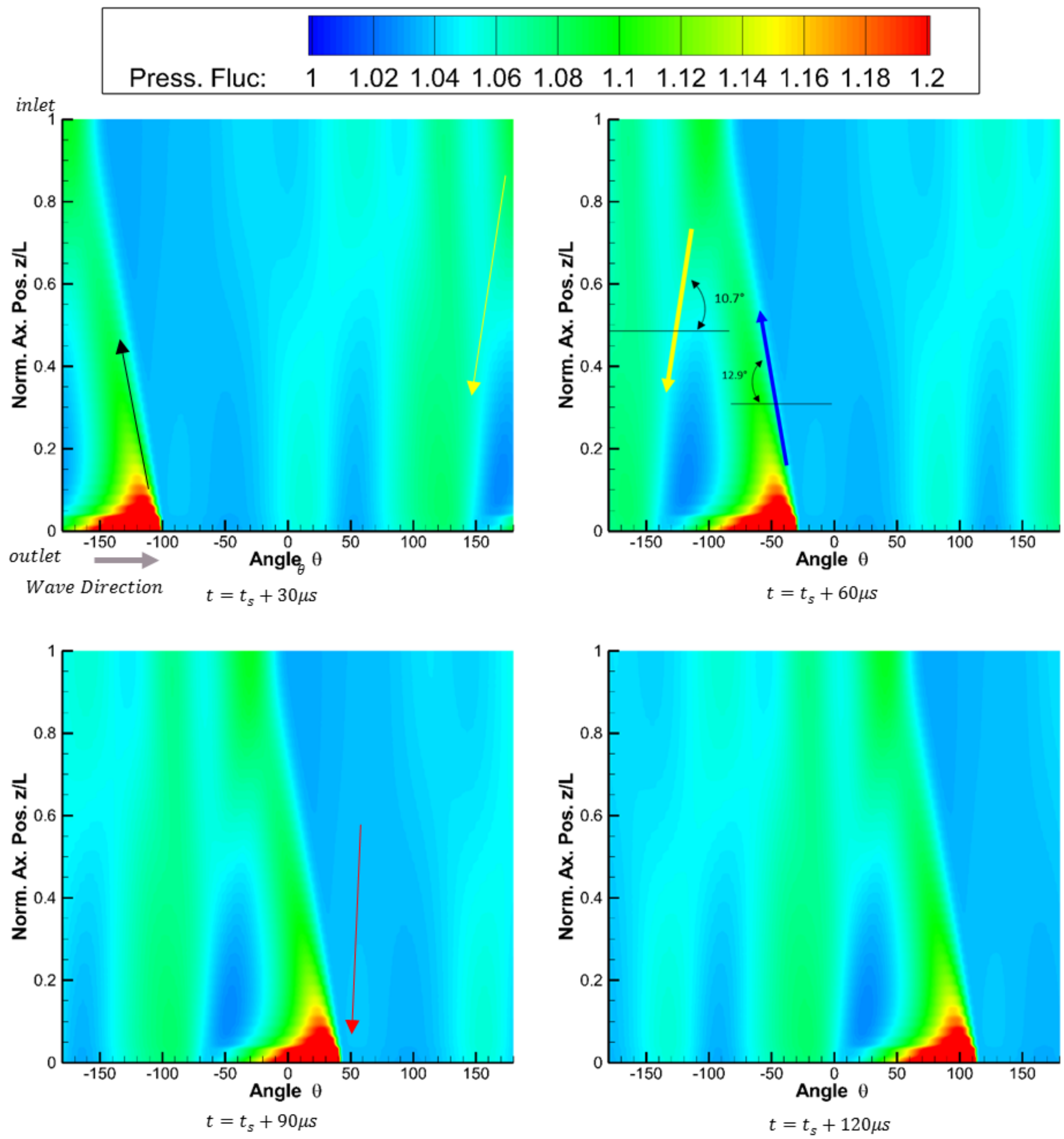


Figure 3.3. Pressure fluctuation (local pressure of the baseline case divided by local pressure of steady boundary condition case) contours for the 50th rotation of calculation unwrapped at R=1.92inch location within the middle of the inlet annulus: the flow direction, and the wave direction are top to bottom, and left to right, respectively. The pressure wave is applied at the outlet (Normalized z=0). The arrows of angle in figure are adjusted with the aspect ratio of the figure(x-axis is compressed largely comparing to y-axis).

Figure 3.4 shows temporal evolution of the axial velocity fluctuation in the inlet duct at the mid-radius point. Here, the axial velocity is non-dimensionalized by the local axial velocity of the steady-flow case with no downstream perturbation. The flow and wave direction are identical as Figure 3.3. The same wave structure Figure 3.3 as is seen: the black arrows show an upstream traveling perturbation while the blue arrow represents a downstream wave. Since the flow rate produced by the injector is proportional to this quantity, it provides an important measure of the inlet dynamic response. From Figure 3.4, the applied wave decelerates the local flow; in the blue region the velocity is depressed to roughly $50 \sim 60\%$ of the unperturbed value whereas the orange region is $110\%$ of the unperturbed value, whereas the majority of the region has slightly faster flow velocity than its steady case. As with the computed pressure, the behavior agrees well with an acoustic wave convecting upstream at velocity $u - a$ and then convecting downstream at velocity u + a.

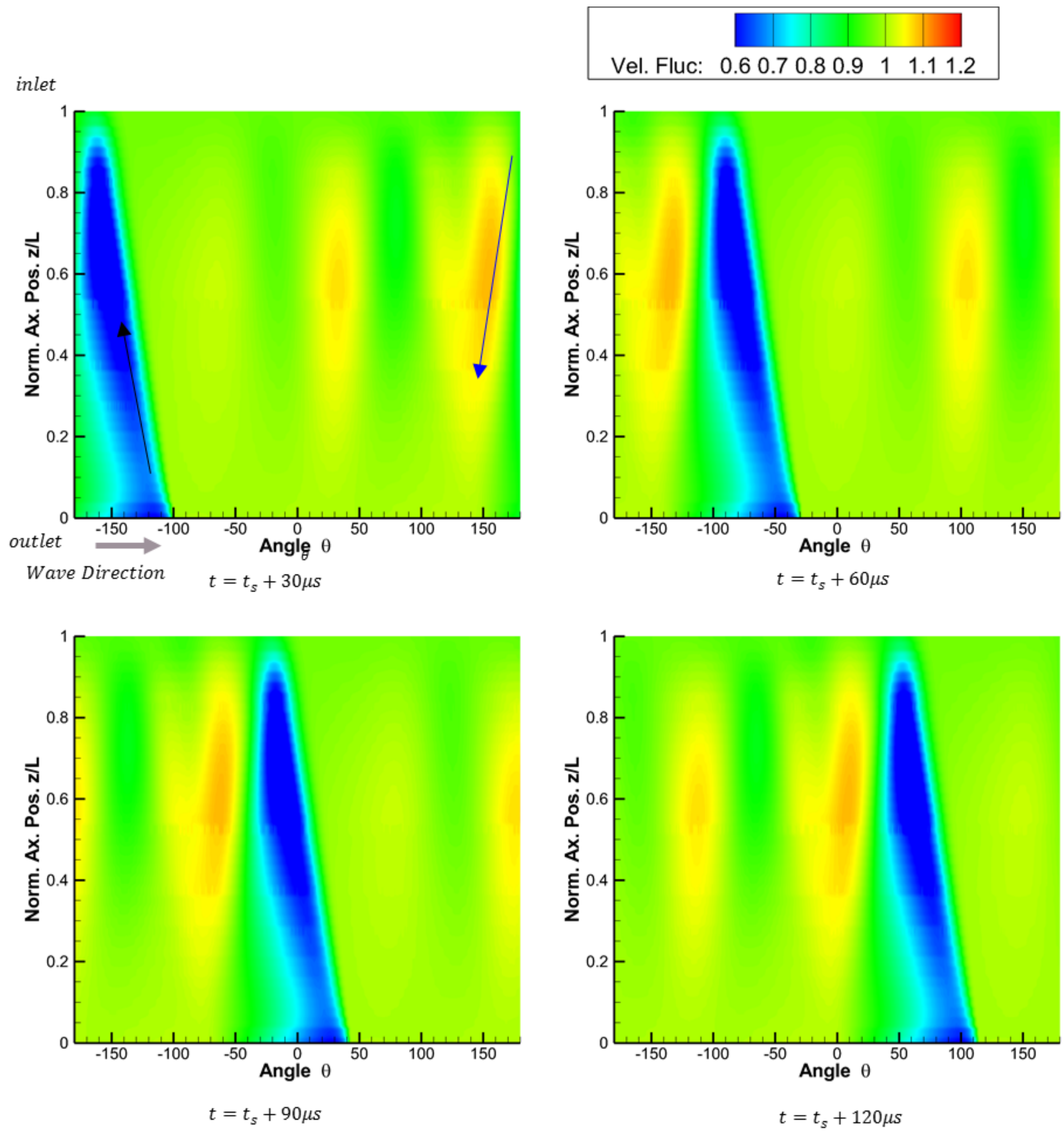


Figure 3.4. Axial velocity fluctuation (local velocity of the baseline case divided by local velocity of steady boundary condition case) contours for the 50th rotation of calculation unwrapped at R=1.92inch location within the middle of the inlet passage: the flow direction, and the wave direction are top to bottom, and left to right, respectively. The pressure wave is applied at the outlet (Normalized z=0).

Unwrapped snapshots of pressure at several axial locations are shown in Figure 3.5. The values at the outlet (the normalized axial position z/L=0 line) are taken from one cell upstream. The largest peak pointed with the red arrows on each line represents the applied pressure wave traveling upstream and the blue arrowed smaller peaks on several lines are the result of the reflection wave traveling downstream. Here it is worthwhile to point out that the injector is metering fluid that evolves a tremendous amount of chemical energy and the small perturbations can manifest themselves as much larger disturbances upon energy release. The applied wave broadens as it travels upstream and is greatly attenuated due to the large area change and the broadening process.

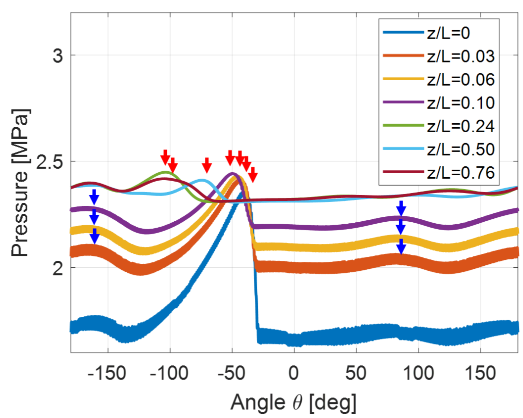


Figure 3.5. Snapshots of Pressure distribution in the axial direction at t=50 $\mu s$ of 50th rotation unwrapped at R=1.92inch. The normalized axial position z/L=0 corresponds the outlet and the values on the line are taken from one cell upstream from the boundary. Red arrows denote the peak of the wave and move from right to left as z/L increases. The blue arrows represent some of reflected peaks from both the the inlet and outlet.

Figure 3.6 provides a graphical depiction of the impulse at a given axial location. Here we note that the impulse contains both applied and reflected wave effects because it is difficult to separate each wave as they interact. Both waves have the identical first mode frequency and its harmonics due to the nature of acoustic wave. This prevents usage of frequency based filters which are usually utilized in signal separation. Formally, the impulse in question is defined:

$$\begin{aligned} \boldsymbol{I} &= \int_{t_S}^{t_{cyc}} p dt - p_{min}(t_{cyc} - t_S) \qquad [Pa \cdot s] \\ I_0 &= I_{input} \qquad [Pa \cdot s] \end{aligned} \tag{3.1}$$

where $P_{min}$ is the minimum pressure for a cycle at a certain fix point at one cell upstream from the boundary, $t_{cyc}$ is the cycle time, and $t_S$ is the starting time of a cycle defined with the certain point.

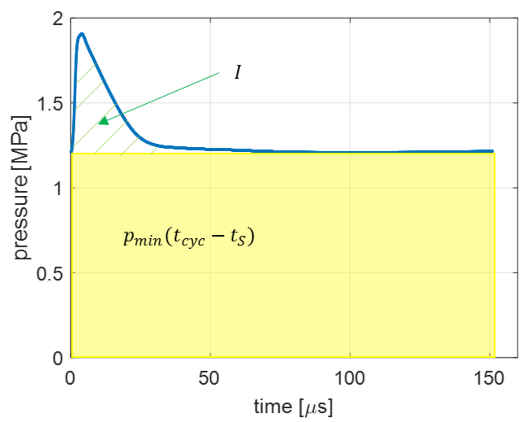


Figure 3.6. Typical Pressure History for a Cycle (blue line) and Denition of Impulse I (hatched area under the line and above the yellow rectangular)

Figure 3.7 shows impulse attenuation normalized by the value applied at the outflow boundary ($I_0$) a few pressure histories at several locations in the inlet. Again, the values at both the boundaries are obtained one cell inside the respective boundaries. Additionally, the impulse information contains both imposed and reflected pressure waves. As seen in the figure, wave is strongly attenuated at the outlet (z/L = 0). The largest attenuation factor here is the boundary condition. The roughly 25% of the annulus is unchoked due to the imposed pressure but remaining 75% is choked. The choked region has the sonic boundary condition and pressure there is only affected by the upstream condition. As a result, the choked region has higher pressure than chamber pressure $P_{cham}$ and this dramatically decreases the transmitted impulse I at z/L=0. The pressure history just upstream of the outlet plane (upper left curve in Figure 3.7) nearly mimics the imposed function except above. However, moving upstream near the z/L = 0.24 location broadening of the wave and attenuation of the peak pressure is evident. Here, an additional wave with different phase is introduced as the reflected wave convects at nearly acoustic speed. Moving further upstream to the z/L = 0.51 location, there is strong evidence of the interaction of the main wave with the reflected wave. This behavior is also noted further upstream at the z/L = 0.6 and 0.7 locations. At the inlet plane the imposed frequency is preserved, although the amplitude is greatly diminished as evidenced by the scale in this pressure plot. Due to the fact that both the imposed and reflected pressure waves interact with widen of the waves, the impulse increases slightly after z/L =0.3.

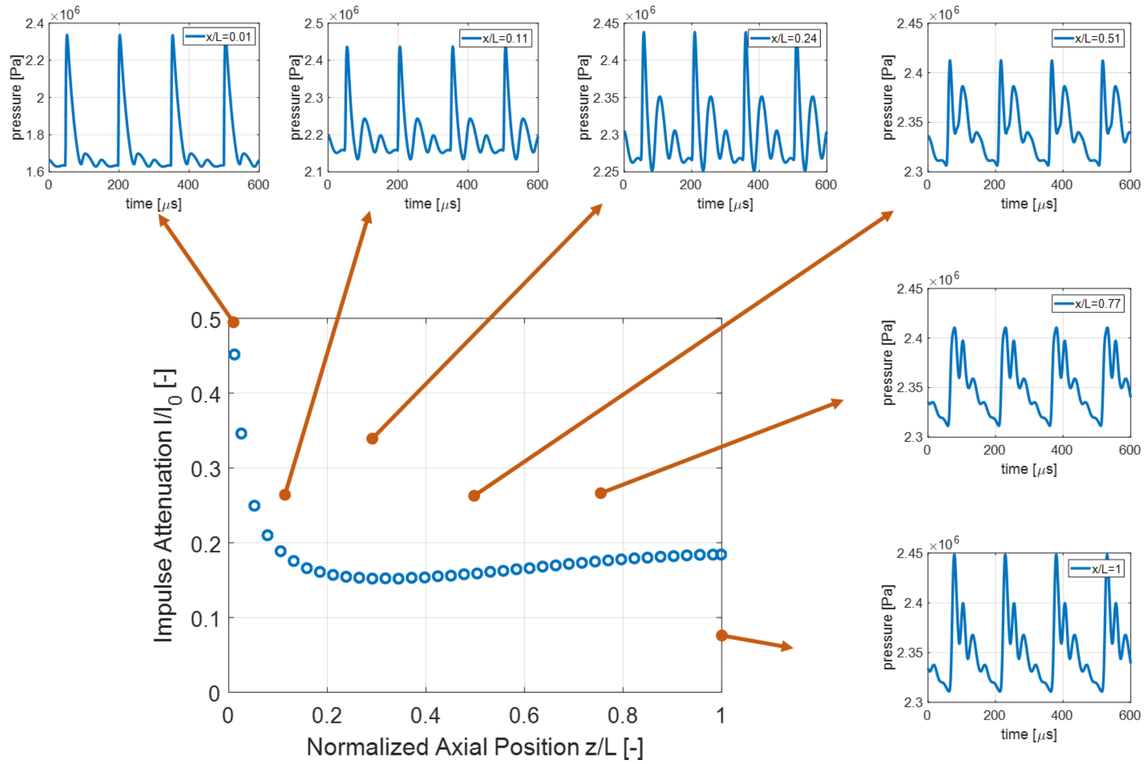


Figure 3.7. Attenuation along with the Axial Direction and Pressure History at Various Locations in the manifold: the flow direction is right to left, while the applied pressure travels left to right and reflects at the inlet (z/L=1). The pressure wave is applied at the outlet (z/L=0). Again, the impulse computed here contains both the imposed and reflected waves. Due to the fact that both the imposed and reflected pressure waves interact with widen of the waves, the impulse increases alightly after z/L =0.3.

Figure 3.8 shows sequential line plots of pressure fluctuation with respect to z/L. The value of y-axis is truncated at Pressure Fluctuation =1.5 and 0.5 in order to observe the wave behavior. This figure demonstrates how the pressure disturbance progress along the axis. At the start of one of the periodic oscillations, t=0$\mu s$, the high pressure wave is imposed at the inlet/combustor interface (z/L=0) and then the imposed wave travels upstream as shown in the blue arrows till t=21$\mu s$. Then the wave remain the inlet (z/L=1) with increment of the pressure fluctuation and reflected back downstream at t=28$\mu s$. This reflected wave propagates downstream and arrives at the outlet boundary around t=49$\mu s$. This wave reflected at the outlet boundary and travels upstream till t=77$\mu s$. The reflection occurs around t=77$\mu s$ at the inlet boundary. The similar sequence of the reflection set at both upstream and downstream boundaries is taken place one more time then the reflection wave from the inlet meets the next impose wave around t=154$\mu s$. There are total three reflections at the inlet boundary and two reflections at the outlet. The imposed wave and reflected waves are attenuated and broaden as they propagate.

Similar structure can be seen in the velocity fluctuation snapshots shown in Figure 3.9. It is observed that the imposed wave and the reflection wave from the outlet boundary decelerate the flow and the reflection waves from the inlet accelerate the flow. There are total three reflections at the inlet boundary and two reflections at the outlet. The imposed wave and reflected waves are attenuated and broaden as they propagate.

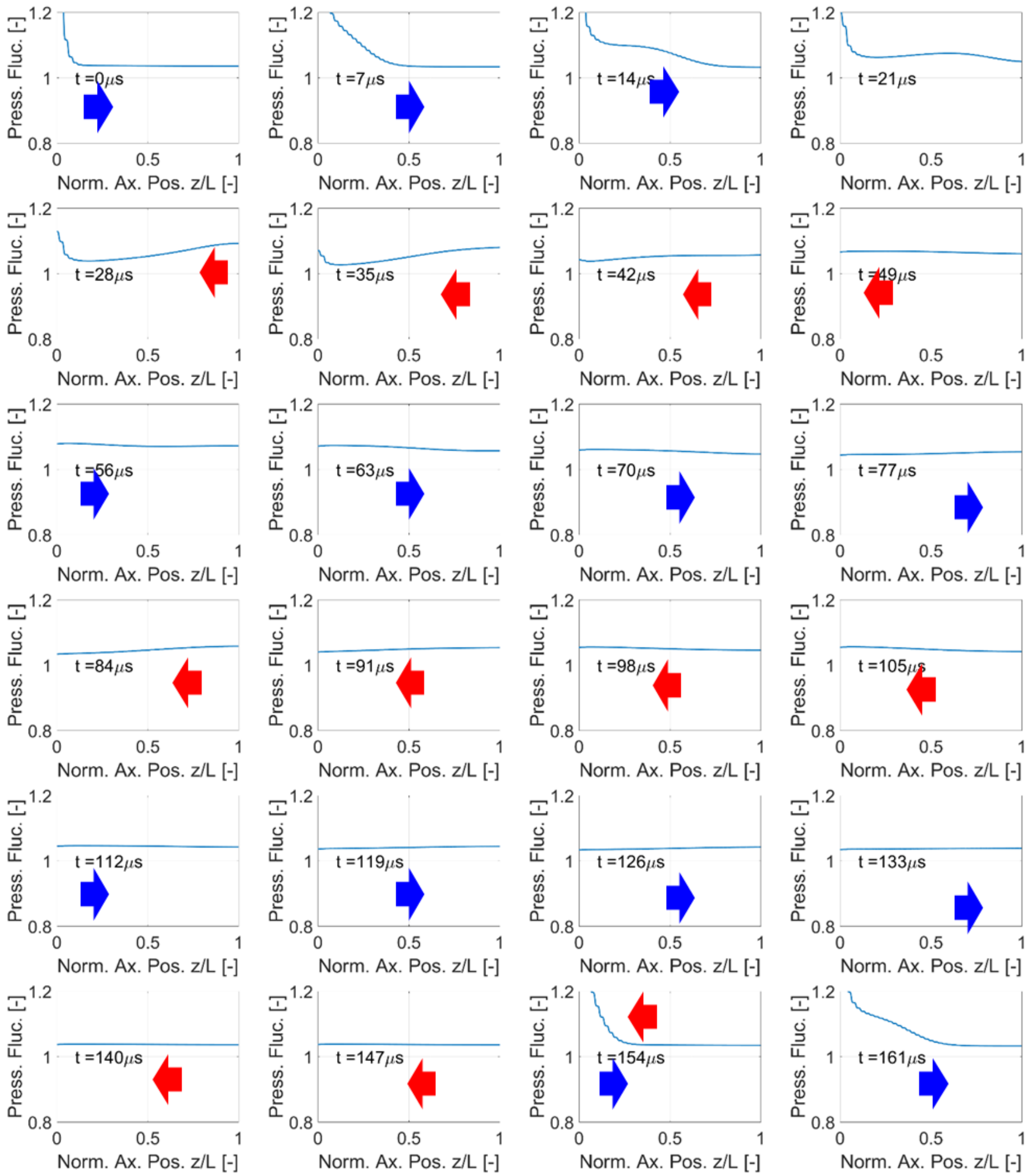


Figure 3.8. Sequential line plot of pressure fluctuation along the normalized injector axis: the flow directionis right to left, while the applied pressure travels left to right and reflects at the inlet (z/L=1). The pressure wave is applied at the outlet (z/L=0). Y-axis is truncated between 0.5 and 1.5. The blue arrow indicates the imposed or relfected wave traveling upstream while the red arrow represents the reflected waves from the inlet boundary.

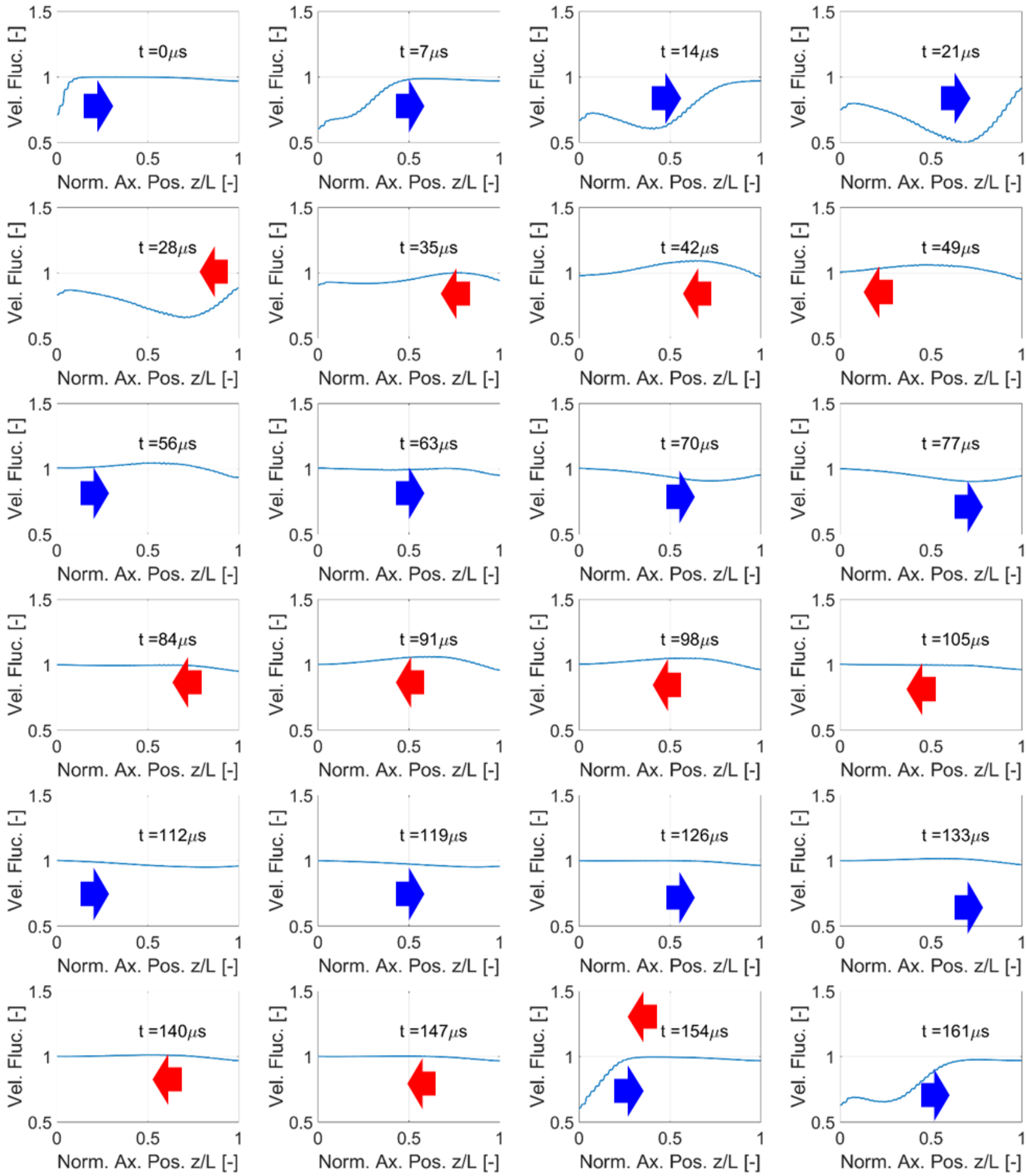


Figure 3.9. Sequential line plot of velocity fluctuation along the normalized injector axis: the flow directionis right to left, while the applied pressure travels left to right and reflects at the inlet (z/L=1). The pressure wave is applied at the outlet (z/L=0). Y-axis is truncated between 0.5 and 1.5.

One of the prime factors motivating this calculation is the determination of the dynamic response of the annular injector to the imposed pressure disturbance that is representative of a passing detonation wave. Figure 3.10 shows pressure, axial velocity, density, fill height, and mass flux history at a point one cell inside from the outlet of the injector for $150\mu s$. The pressure history has one large peak, which represents the imposed wave and other small two peaks. The two peaks are caused by the reflections. The velocity history indicates that there is no back flow in this condition since the amplitude of the imposed disturbance does not exceed the inlet pressure for this strongly convergent inlet design. However, there is roughly 100 m/s drop in velocity due to the imposed disturbance. Also, there are small overshoots around 55 and $105\mu s$ due to the reflection waves. The gas density field is increased by approximately 35% increment by the imposed disturbance and the two small disturbances around 55 and $105\mu s$. These large variations may affect the detonation behavior at the chamber.

In order to assess the influence of injector unsteadiness on the combustor flow, fill height and mass flux histories to the chamber are presented in Figure 3.10. The fill height is assumed to simply be the time integral of the fill velocity. The fill process is interrupted ever-so-slightly by the imposed waveform, but the bulk of the graph shows a linear behavior associated with a constant fill velocity. In contrast, the mass flux shows a more complex behavior due to the counteracting effects of gas deceleration and compression from the imposed disturbance. The large reduction in velocity dominates the mass flux at early times. As a result the injector flow drops directly after wave passage. As the flow recovers, there is actually an interval of overshoot due to the transient combination of velocity and density disturbances due to the reflection wave. Eventually the mass flux takes on a steady character at times about identical that of the imposed disturbance. This complex behavior implies that keeping instantaneous chamber mixture ratio as designed is very difficult except in the case with fuel injectors which behave identical to the oxidizer injector.

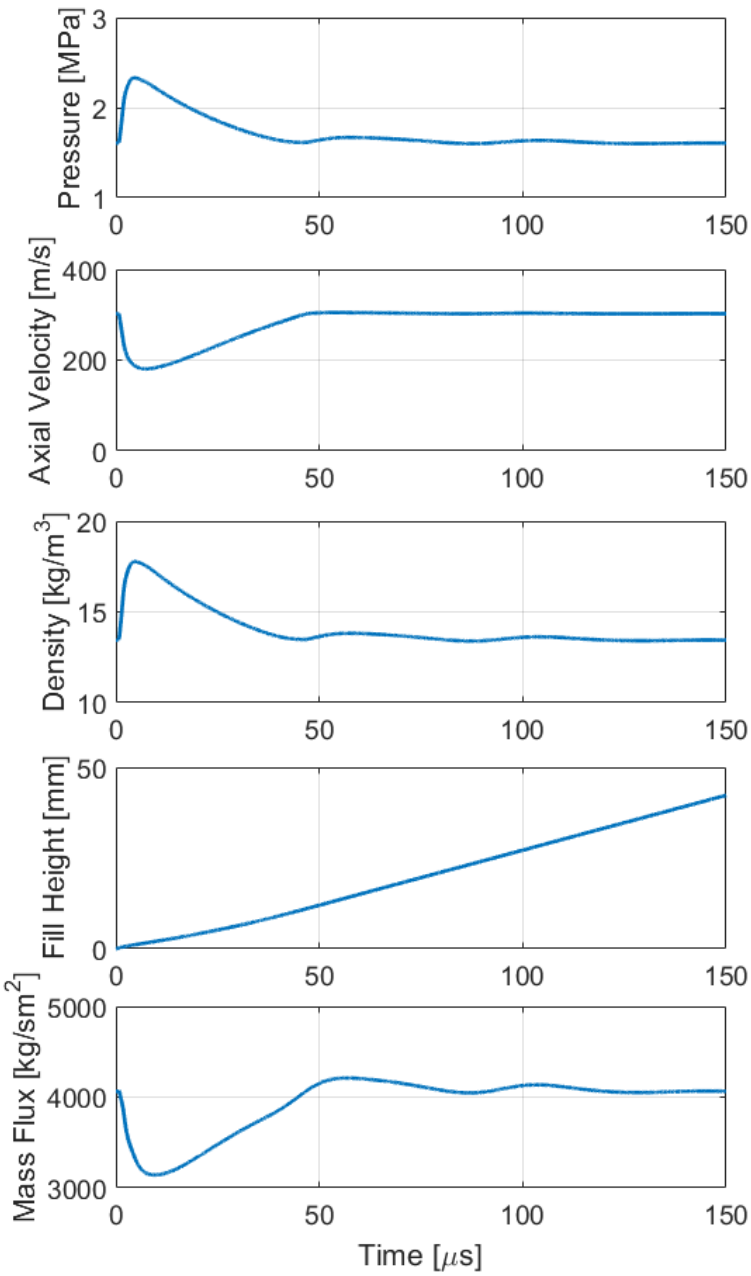


Figure 3.10. Pressure, Axial Velocity, Density, Mass Flux and Fill Hight History for 150$\mu s$ at the outlet (The values are computed from one cell upstream from the outflow boundary): the cycle time of this condition is roughly for 151$\mu s$.

## 3.2 Parametric Study

In this section the results of the parametric study are presented. The calculation cases evaluate effects of detonation strength and design parameters such as input pressure ratio, input impulse size, area ratio, and number of waves. Other simulation conditions are kept the same as explained in Chapter 2. For example, the inlet is a constant mass flow boundary ($\dot{m} = 0.96kg/s$ at T=500K of pure oxygen). In all cases, most of the outlet is choked except in the region where the high pressure is imposed. Table 3.1 shows details regarding the important results whereas Table 2.3 in the previous chapter contains the parametric conditions. The main results compared in the parametric study are average manifold pressure which is obtained at the middle of the axial direction (z/L=0.5), cycle fill height, injector check-off interval, impulse attenuation along the injector axis and mass flux fluctuations (both maximum and minimum from the steady condition). The cycle fill height is the final fill height of a cycle, which is a key parameter for RDE operation [5]. The cycle fill height is related to the mixture amount that the next detonation front can consume. It is useful to characterize the transient injector response in terms of an equivalent injector check-off interval, $t_{off}$, attributed to the imposed detonation overpressure. Physically, the check-off interval is the interval that a steady- flow injector would need to be turned off in order to produce the same integrated mass flow as the dynamic injector response:

$$\frac{\overline{\dot{m}}}{A}(t_{cyc} - \boldsymbol{t_{off}}) = \int_{t_S}^{t_{cyc}} \rho w dt \tag{3.2}$$

where $\overline{\dot{m}}$is the average mass flow rate, $t_{cyc}$ is the cycle time and $\rho u$ is the computed mass flux at the injector exit boundary. The maximum and minimum mass flux in percent are computed with Equation 3.3:

$$\begin{aligned} max\ mass\ flux &= \tfrac{(max[\rho v] - \dot{m}A_{\text{outlet}})}{\dot{m}A_{\text{outlet}}} \\ min\ mass\ flux &= \tfrac{(min[\rho v] - \dot{m}A_{\text{outlet}})}{\dot{m}A_{\text{outlet}}} \end{aligned} \tag{3.3}$$

where max and min are the maximum and minimum functions, $\rho$ and $v$ are the density and velocity from the computational result and $\dot{m}$ and $A_{\text{outlet}}$ are the mass-flow rate and the area of the exit plane.

Table 3.1. Summary of parametric study results. The average injector pressure is computed at the middle of axial direction ($z/L$=0.5).

| Case No. Name | Average Injector Pressure [MPa] | Cycle Fill Height [mm] | Maximum Mass Flux [%] | Minimum Mass Flux [%] | Check-off Intervals [ns] |
|---|---|---|---|---|---|
| 0. Base PR=8 | 2.34 | 42.6 | 5.7 | -11.0 | 0.9 |
| 1. Long PR=8 | 2.32 | 55.8 | 4.6 | -5.4 | 0.1 |
| 2. Long PR=11 | 2.38 | 53.8 | 8.7 | -23.0 | 0.6 |
| 3. Long PR=19 | 2.56 | 50.7 | 19.7 | -83.5 | 3.5 |
| 4. Small Dia. | 2.31 | 27.4 | 3.3 | -6.8 | 0.2 |
| 5. Same I PR=4.5 | 2.29 | 57.3 | 3.0 | -2.7 | 0.0 |
| 6. Two Wave | 2.34 | 27.0 | 4.9 | -4.7 | 0.2 |
| 7. Wider Gap PR=19 | 1.72 | 48.1 | 68.1 | -203.0 | 12.1 |
| 8. Same I PR=15 | 2.41 | 54.6 | 10.6 | -53.9 | 1.0 |
| 9. Two Wave PR=19 | 3.16 | 21.5 | 33.0 | -73.1 | 3.9 |

### 3.2.1 Effect of Inlet Length

As noted in Table 2.3, Case 1 presumes a triangular pressure excursion with a maximum pressure ratio of 8.0 and a width corresponding to 30% of the annulus. A detailed evaluation of this case is presented as it is representative of the inlet geometry in the Purdue experimental rig [7]. Figure 3.11 shows these dimensionless pressure fluctuation contours at various instances in time. Contours are displayed as a function of azimuthal location for a point at R=1.92 inch which is the center of the converging annular passage. The flow direction is from top to bottom. The wave is imposed in azimuthal direction from the left to right as shown as the magenta arrow. The black arrows indicate the pressure fluctuation traveling up stream and the yellow and red arrows represent the downstream reflection wave. As with Case 1, the wave is significantly attenuated even at locations very near the exit plane. For example, the red region represents pressures only about 18% above the unperturbed value.

As seen the red arrow in Figure 3.11, the reflected wave traverses the next applied wave as it convects to the outlet boundary. There is, however, no reflection from the outlet boundary, due to the fact that the region at which the reflected wave arrives is choked and is represented as a supersonic boundary. The reflection wave effect can be seen as iso-pressure line angle change reported in Figure 3.11 which is a magnified image of t=60$\mu s$. The high pressure fluctuation peak trajectory forms a "ridge" that corresponds the imposed and reflected waves. Since the x-axis is unwrapped angle in the constant radius and y-axis is a normalized axis of the injector, an angle of the ridge from x-axis represents a velocity vector angle constructed with the wave velocity and axial characteristic velocity (either u+a or u-a). The two angles on Figure 3.11 are computed with the input wave speed (2000m/s), average flow velocity (39.8m/s), and average sonic speed (418.1m/s) and adjust to the aspect ratio of the figure. These angles agree with the contour ridges since high Mach number region is limited to near the exit.

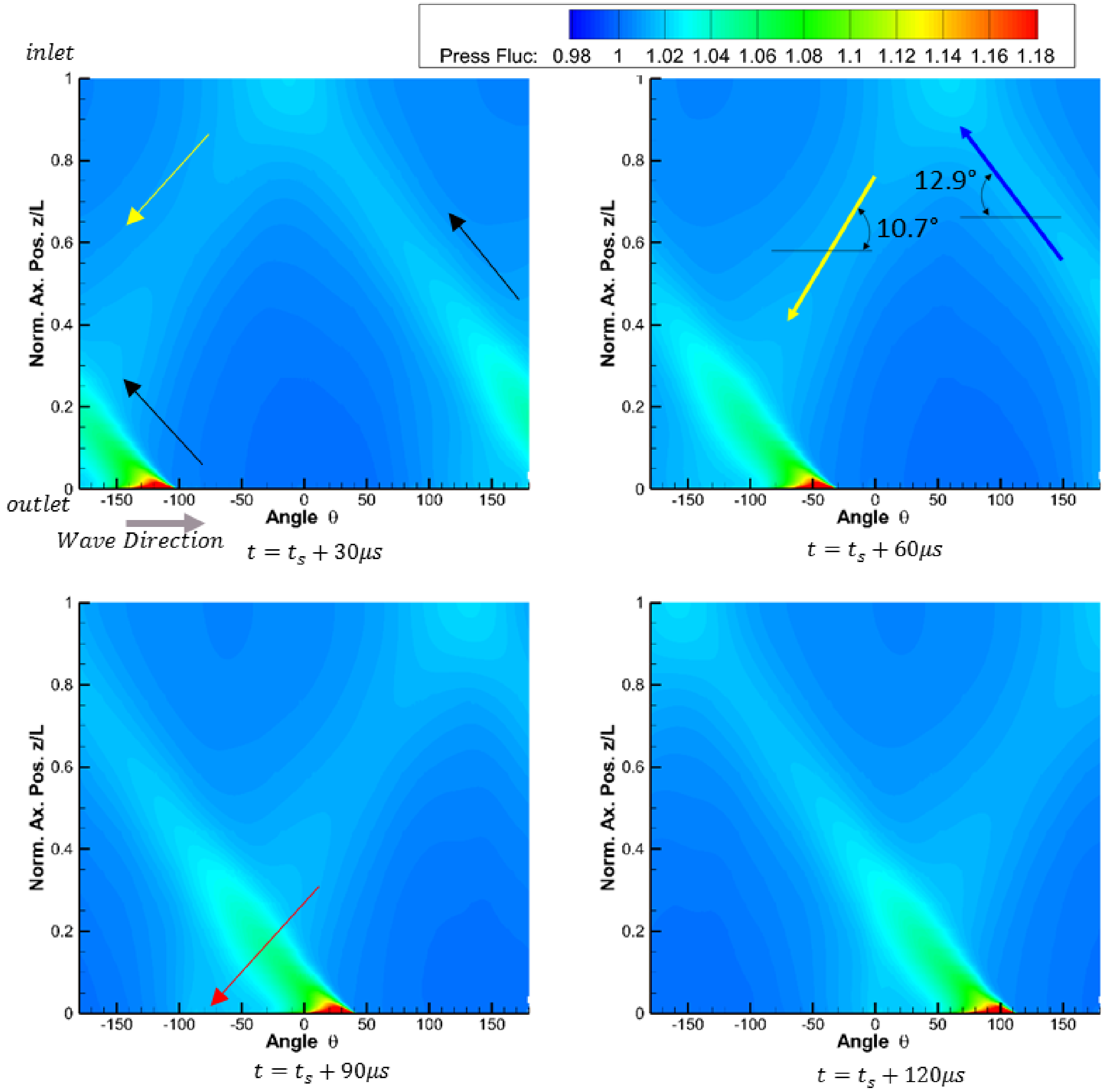


Figure 3.11. Pressure fluctuation (local pressure of the baseline case divided by local pressure of steady boundary condition case) contours for the 24th rotation of calculation unwrapped at R=1.92inch location within the middle of the inlet annulus: the flow direction, and the wave direction are top to bottom, and left to right, respectively. The pressure wave is applied at the outlet (Normalized z=0). The arrows of angle in figure are adjusted with the aspect ratio of the figure(x-axis is compressed largely comparing to y-axis).

Figure 3.12 shows temporal evolution of the axial velocity fluctuation in the inlet duct at the mid-radius point. The flow and wave direction are the same as Figure 3.11. The same wave structure Figure 3.11 as is seen: the black arrows show upstream traveling perturbation while the blue arrow represents the downstream wave. Since the flow rate produced by the injector is proportional to this quantity, it provides an important measure of the inlet dynamic response. From Figure 3.12, the applied wave decelerates the local flow; in the blue region the velocity is depressed to roughly 80-90% of the unperturbed value whereas the red region is 110% of the unperturbed value. This behavior agrees well with an acoustic wave convecting upstream at velocity $(u - a)$ and then convecting downstream at velocity $(u + a)$ where a is sound local sound speed.

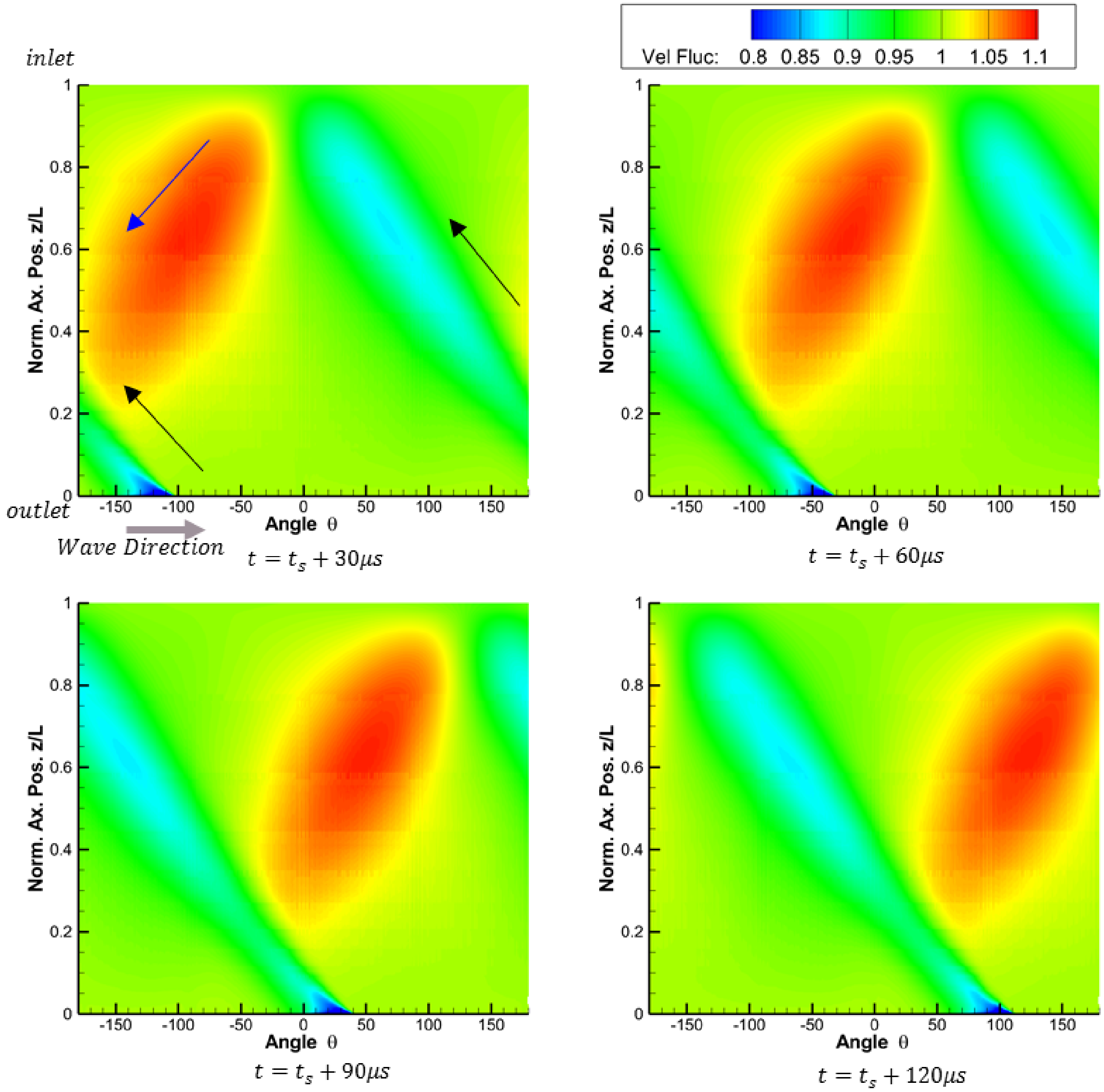


Figure 3.12. Axial velocity fluctuation (local velocity of the baseline case divided by local velocity of steady boundary condition case) contours for the 24th rotation of calculation unwrapped at R=1.92inch location within the middle of the inlet passage: the flow direction, and the wave direction are top to bottom, and left to right, respectively. The pressure wave is applied at the outlet (Normalized z=0).

Unwrapped snapshots of pressure at several axial locations are shown in Figure 3.13. The values at the outlet (the normalized axial position z/L=0 line) are taken from one cell upstream. The maximum pressure at z/L=0 line is 1.93MPa which is 2% smaller than the maximum input pressure (2MPa) due to the handling of boundary handling explained in Chapter 2. The largest peak on each line represents the applied pressure wave traveling upstream and the smaller peak on z/L=0.5 and 0.76 lines is the result of the reflection wave traveling downstream. The reflection peaks near the inlet are not observed because the large area change along the axial direction hides the peak. The applied wave broadens as it travels upstream and is greatly attenuated due to the large area change and the broadening process.

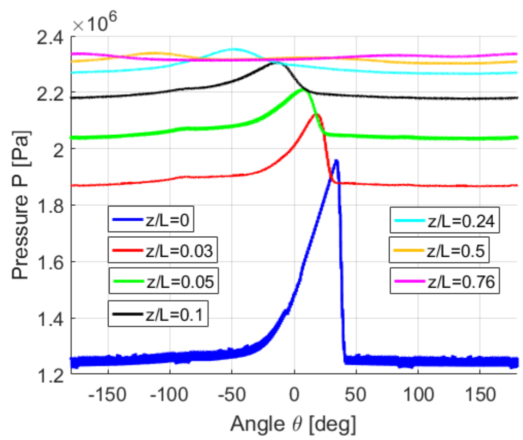


Figure 3.13. Snapshots of Pressure distribution in the axial direction at $t = t_S + 50\mu s$ of 24th rotation unwrapped at R=1.92inch. The normalized axial position z/L=0 corresponds the outlet and the values on the line are taken from one cell upstream from the boundary.

Figure 3.14 shows impulse attenuation normalized by the value applied at the outflow boundary ($I_0$) a few pressure histories at several locations in the inlet. As seen in the figure, wave is strongly attenuated at the outlet (z/L = 0). The largest attenuation factor here is the boundary condition. The roughly 28.8% of the annulus is unchoked due to the imposed pressure but remaining 71.2% is choked. The choked region has the sonic boundary condition and pressure there is only affected by the upstream condition. As a result, the choked region has higher pressure than chamber pressure $P_{cham}$ and this dramatically decreases the transmitted impulse I at z/L=0.

The pressure history just upstream of the outlet plane (upper left curve in Figure 3.14) nearly mimics the imposed function except above. However, moving upstream near the z/L = 0.2 location broadening of the wave and attenuation of the peak pressure is evident. Moving further upstream to the z/L = 0.5 location, there is strong evidence of the interaction of the main wave with the reflected wave. Here, an additional wave with different phase is introduced as the reflected wave convects at nearly acoustic speed. This behavior is also noted further upstream at the z/L = 0.6 and 0.7 locations. At the inlet plane the imposed frequency is preserved, although the amplitude is greatly diminished as evidenced by the scale in this pressure plot. The dip on the figure is caused by the interaction between imposed upstream traveling wave and the reflected wave which convects downstream. This can be confirmed with Figure 3.15 which is same as Figure 3.11 $t = 60\mu s$, except the line which shows the "dip" position. The dip position is the smallest pressure gain position along the axis of the injector due to the interaction of the imposed wave and the reflected wave.

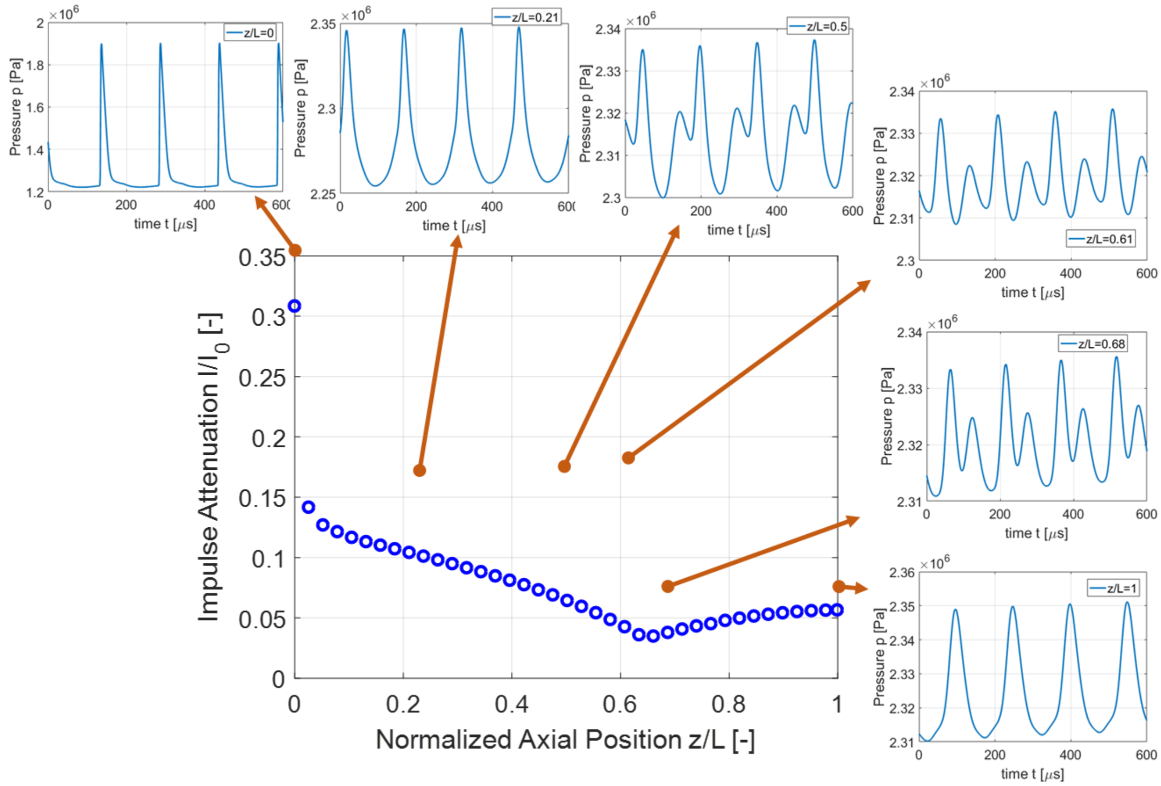


Figure 3.14. Attenuation along with the Axial Direction and Pressure History at Various Locations in the manifold: the flow direction is right to left, while the applied pressure travels left to right and reflects at the inlet (z/L=1). The pressure wave is applied at the outlet (z/L=0).

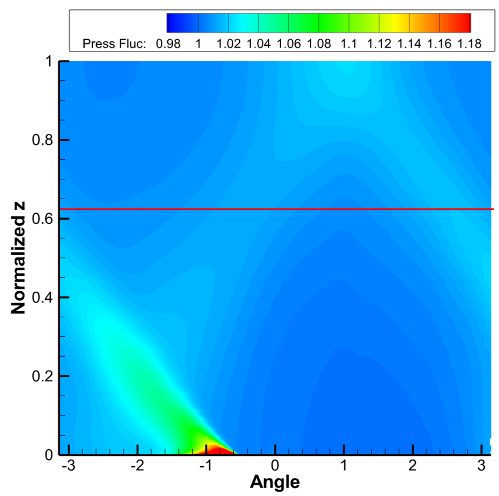


Figure 3.15. Pressure fluctuation contour: The red line indicates the axial location of the "dip" in impulse in Figure 3.14

As mentioned previously, the disturbance appears to propagate almost entirely at acoustic speed, i.e. that non-linear effects appear to be largely unimportant relative to the speed the disturbance is convected. Figure 3.16 demonstrates this assertion as the CFD result and the wave position estimated with 1D steady analytical result assuming upstream/downstream propagation at $u + a$ and $u - a$ speeds, respectively using standard compressible flow treatment in Eqns.3.4 to 3.7 below. The maximum and/or peaks of the pressure along the axis are captured in every time step from the CFD results. The "wait" at the inlet boundary is caused by the width of the wave and the pressure values during the "wait" at the boundary are changing over time. The resultant time-position history is computed by integrating the characteristic velocity along the axial direction. The inlet of injector is at z/L =1 and the outlet is 0. It is noted that the "wait" time at the inlet of analytical result is adjusted to the CFD result since 1D steady analytical method cannot predict the time. Also, CFD inlet result is utilized for $T_0$ in the analytical method.

$$\frac{A(z)}{A_{exit}} = \frac{M_{exit}}{M(z)} \left[ \frac{(1 + \frac{\nu-1}{2} M(z)^2)}{(1 + \frac{\nu-1}{2} M_{exit}{}^2)} \right]^{(\nu+1)/(\nu-1)} \tag{3.4}$$

$$\frac{T_0}{T(z)} = 1 + \frac{\nu - 1}{2} M(z)^2 \tag{3.5}$$

$$u(z) = M(z)\sqrt{\gamma RT(z)} \tag{3.6}$$

$$a(z) = \sqrt{\gamma RT(z)} \tag{3.7}$$

As noted previously, both results agree especially for upstream, except the initial part. The difference near the inlet is caused by the imposed pressure. The flow velocity u become slower due to the applied wave and the upstream wave travel velocity $u - c$ is larger than the steady 1D analysis. The similar effect can be seen near the inlet for the reflected wave. The reflected wave makes local flow speed faster and the downstream wave travel velocity $u + a$ becomes greater there. These wave and flow velocity interaction can be confirm graphically in Figure 3.11.

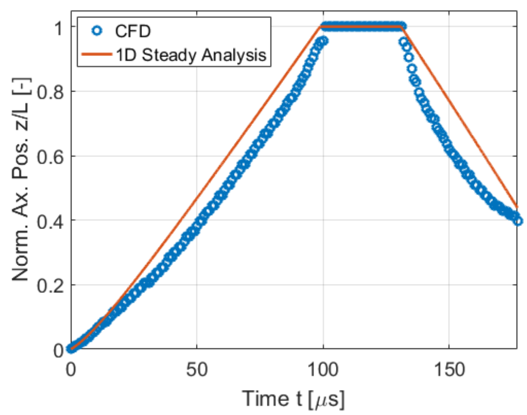


Figure 3.16. Wave Peak Position Comparison between CFD result and 1D steady analysis: free end reflection at the inlet makes the peak "wait" at the inlet and the waiting time of isentropic result is adjusted withe the CFD value. The inlet of injector is at z/L (the normalized axial position) =1 and the outlet is placed at z/L = 0.

Figure 3.17 shows pressure, axial velocity, density, fill height, and mass flux history at a point one cell inside from the outlet of the injector for 220$\mu s$. Again, the maximum pressure is 1.93MPa; 2% smaller than the input pressure (2MPa) due to the outflow boundary treatment discussed in Chapter 2. The velocity history indicates that there is no back flow in this condition due to the fact that the amplitude of the imposed disturbance does not exceed the inlet pressure for this strongly convergent manifold design. However, there is roughly 100 m/s drop in velocity due to the imposed disturbance .Also, there are small overshoots near 35 and 205$\mu s$ due to the previous reflection wave. The gas density field is increased by approximately 35% increment by the imposed disturbance. These large variations may affect the detonation behavior at the chamber.

The fill height and mass flux histories to the chamber are also presented in Figure 3.17. The fill process is interrupted ever-so-slightly by the imposed waveform, but the bulk of the graph shows a linear behavior associated with a constant fill velocity as same as the base case. The mass flux shows a more complex behavior due to the counteracting effects of gas deceleration and compression from the imposed disturbance. The large reduction in velocity dominates the mass flux at early times. As a result the injector flow drops directly after wave passage. As the flow recovers, there is actually an interval of overshoot due to the transient combination of velocity and density disturbances due to the reflection wave. Eventually the mass flux takes on a steady character at times about identical that of the imposed disturbance. The reflection wave arrival with respect to the imposed wave is different comparing to it in the base case, due to the longer injector. As a result, the mass flux fluctuation is less because of the more dumping effect due to the long injector design.

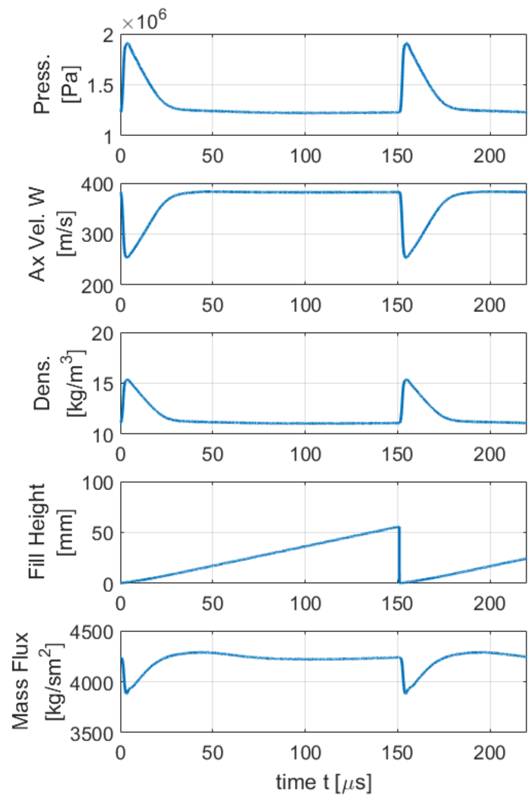


Figure 3.17. Pressure, Axial Velocity, Density, Mass Flux and Fill Hight History for $220\mu s$ at the outlet (The values are computed from one cell upstream from the outflow boundary): the cycle time of this condition is roughly for $151\mu s$ . In the axial velocity field, small over shoots near for 35 and $205\mu s$ are caused by the previous reflected wave.

### 3.2.2 Effect of Impulse Shape

The effects of input impulse shape is investigated on three cases: Case 1, 5 ,and 8. These three cases have identical input impulse values but their shape is different. There is no back flow in these three cases. From Table 3.1, the average manifold pressure increases as the input pressure ratio increases among these cases, although the input impulse is the same value. This can be explained as the higher input pressure creating an unchoked region and the high pressure propagating through the region to the manifold. As a result, the manifold average pressure becomes larger.

The input impulse shape affects the cycle fill height. Higher peak pressures do lead to a lower fill height and a lower overall inlet responsiveness even though the overall impulse is identical in these cases. Case 5 has a 1.5mm larger cycle fill height than the base case and Case 8 has a 1.2mm smaller cycle fill height than the base case. These are explained in Figure 3.18, which is the history data of the three cases. As seen in the figure, large imposed pressure on Case 8 reduces the axial velocity during the time when higher pressure is applied (roughly $20\mu s$). The large reduction of the axial velocity dominates the fill height non-linearity in this case. The base case and Case 5 recover their axial velocity slower (approximately $25\mu s$) than the higher pressure case but the reduction of axial velocity is much smaller and the non-linear part of fill height histories are small.

The injector check-off intervals are affected by the input impulse shape. Similar to the cycle fill height, the main parameter is high pressure impulse. The higher pressure case (Case 8) has the largest check-off time among the three cases. In Case 8, although the large imposed pressure compresses the oxygen gas, the large axial velocity reduction dominates the mass flux history. The mass flux overshoots the steady mass flux due to the previous reflection wave effect after the large reduction. However, it does not affect the check-off interval. In the base case, a similar phenomenon to Case 8 is observed except with a slightly longer time to the pressure recovery, axial velocity, density, and mass flux. In addition to this, the reduction of mass flux is much smaller. The check-off interval of the case is $0ns$ because the input pressure is not high enough to unchoke the outlet boundary.

Impulse attenuation along the axis of the injector is also investigated. Figure 3.19 shows impulse attenuation along the injector axis for these identical input impulse cases. The higher input pressure cases have a larger transmission of impulse to the injector manifold, and then the impulse faded quickly near the injector outlet. In Figure 3.19 , the “dip” in each line is caused by the interaction of the imposed and

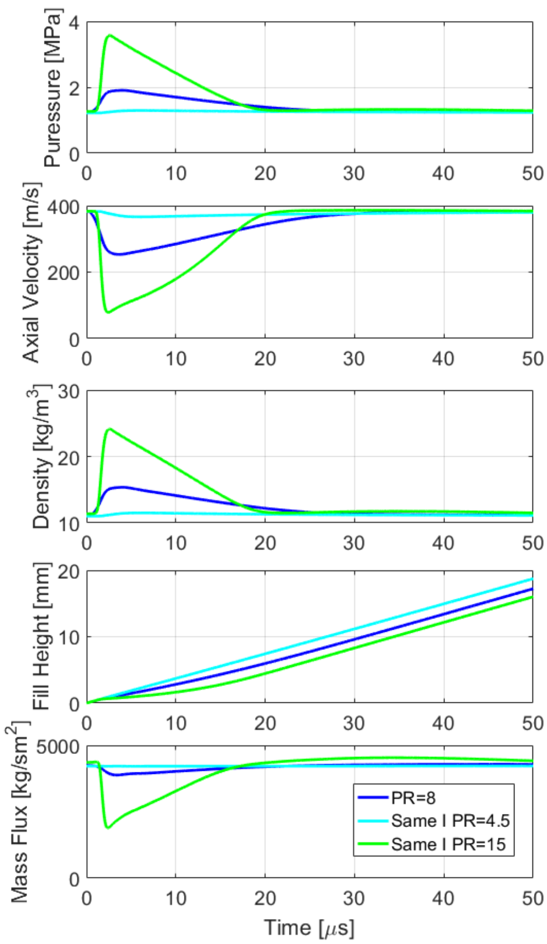


Figure 3.18. Pressure, Axial Velocity, Density, Fill Height, and Mass Flux History of Identical Impulse Cases (Case1, 5, 8) for $50\mu s$

reflected waves. Interestingly the dip position does not change with respect to the input impulse shape.

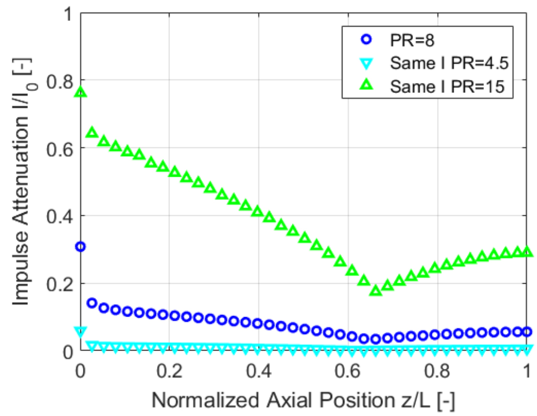


Figure 3.19. Impulse attenuation along the axis of the injector for the cases with identical input impulse

### 3.2.3 Effect of Wave Intensity

Three cases (Case 1, 2, and 3) are compared to evaluate effects of wave intensity. As explained in Chapter 2, the input pressure ratio is the only difference among the three cases. Higher input pressure ratio automatically means higher input impulse in these cases. There is no back flow at the limited cycle period in the three cases but there is back flow in the early cycles in the highest pressure ratio case (PR=19). As in the previous subsection, a higher input pressure ratio results in higher average manifold pressure for the same reason: the input high pressure propagates through the unchoked region of the outlet and pressurizes the manifold.

For the cycle fill height, the trend seems similar to the previous subsection. The relation between the input pressure ratio and cycle fill height is nearly proportional. Larger pressure ratio and impulse causes a wider unchoked region on the output, and this wider unchoked region makes flow slower. The highest input pressure case has 10% less cycle fill height compared to the base case. The higher imposed pressure impedes flow and reduces axial velocity more and for a longer time as shown in Figure 3.20. At the highest pressure time (around $3\mu s$), the axial velocity is reduced to 25m/s, which predominantly reduces fill height. The combination of the pressure ratio and impulse size affects to the axial velocity recovery time. Higher input pressure ratio and larger impulse size result in longer recovery time. The axial velocity recovery time is identical to the time at which the fill height history becomes a straight line.

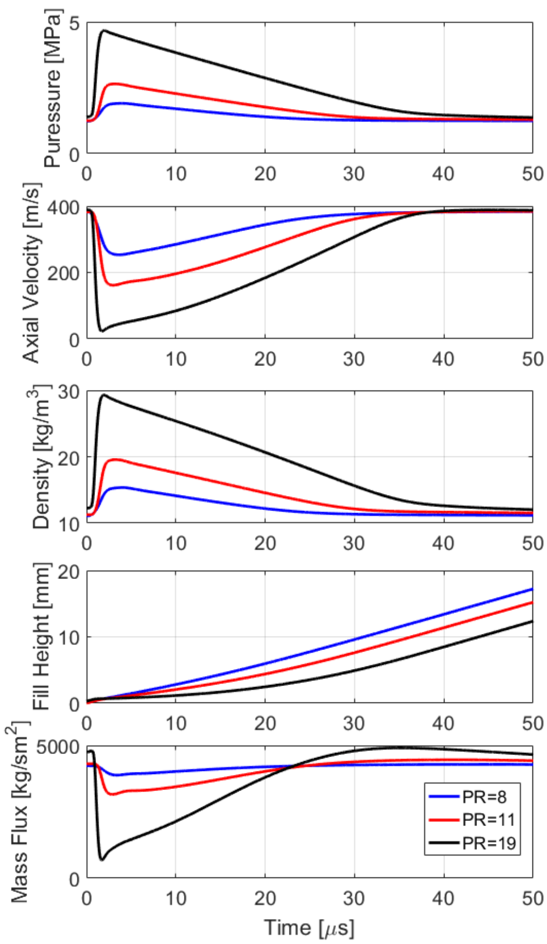


Figure 3.20. Pressure, Axial Velocity, Density, Fill Height, and Mass Flux History of cases (Case1, 2, 3) with different input pressure ratio for $50\mu s$

The injector check-off interval of Case 3 is dramatically more increased than the base case. This can be seen in the mass flux history: the imposed pressure decreases the mass flux around $3\mu s$ and this larger drop increases the check-off interval. It is noted that a higher pressure case has larger overshoot in the axial velocity and mass flux due to the larger reflected wave. Interestingly, the time when the overshoot occurs is identical in the three cases.

Figure 3.21 reports impulse attention along with the injector axis for Case1, 2, and 3 with different input pressure ratios. As in the previous subsection the same phenomenon is observed in these cases. Higher pressure case has more an impulse transmission at the outlet boundary (z/l=0). The transmitted impulse quickly decays near the boundary. The dip position is identical among these three cases and also the three cases in the past subsection. The dip point similarity suggests that the wave traveling speeds ($u + a$ and $u - a$) are identical for these 6 cases.

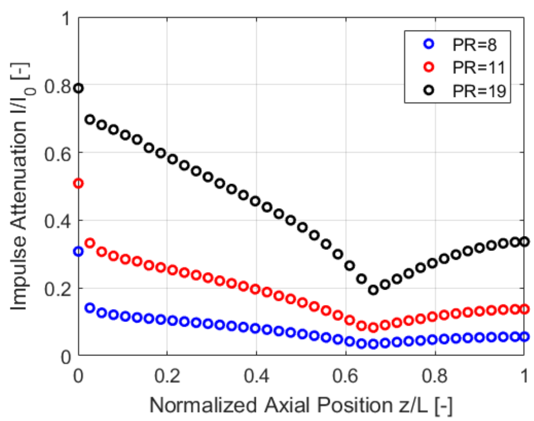


Figure 3.21. Impulse attenuation along the axis of the injector for the cases with identical input impulse

### 3.2.4 Effect of Number of Waves and Aspect Ratio of Injector

The number of wave effects are investigated with Cases 1 and 6 with a low input pressure, and Cases 3 and 9 with a high input pressure. Effects of the aspect ratio of the injector is also evaluated in Cases 1 and 4 with a low pressure input. There is no back flow in any cases in the limited cycle. However, in Cases 3 and 9, there is back flow in the early cycles. In the lower pressure input cases (Case 1, 4, and 6), the average manifold pressure is nearly the same. In contrast to the higher input

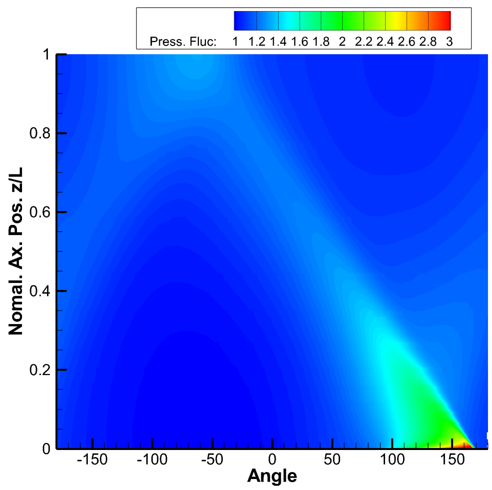


Figure 3.22. Pressure fluctuation contours unwrapped of the input pressure ratio=19 case at R=1.92 inch

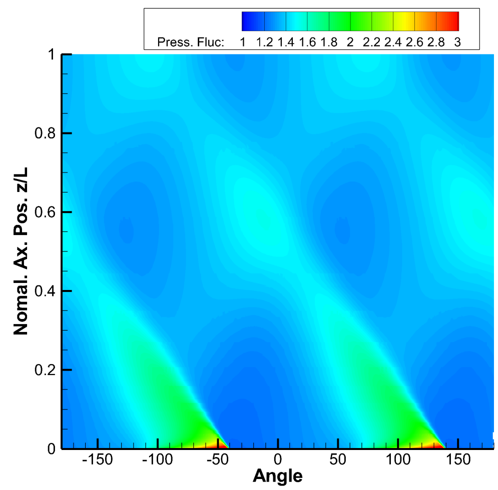


Figure 3.23. Pressure fluctuation contours unwrapped of the two wave and input pressure ratio=19 case at R=1.92 inch

pressure cases, the increment of the wave raises the average manifold pressure by 23% (0.6 MPa). It is worth presenting the unwrapped pressure fluctuation contour of both the highest pressure cases in Figure 3.22 and Figure 3.23. As seen in the figures, the wave structure of the two wave cases is a superposition of the single wave case, except with regard to the interaction of waves and pressurized background.

The cycle fill height of the low input pressure two wave case (Case 6) is approximately the half of the low input pressure single wave case (Case 1), and close to the cycle fill height of small diameter case (Case 4). In order to explain these, Figure 3.24 presents history data of these three cases (Case 1, 4, and 6). The two wave case is identical to the base case except regarding the cycle time. The dynamic effect in the fill height only occurs in the early region. As a result, the cycle fill height of the two wave case is slightly smaller than that of the base case. The smaller diameter case has a marginally larger (approximately 10m/s) axial velocity where the imposed wave has no affect but the difference is small, so the cycle fill height is almost the same as in the two wave case. In fact, the cycle fill height is dominated by the dynamic response instead of the steady velocity region in these cases. In the high input pressure, the cycle fill height of the two wave case (case 9) is 3.85 mm smaller than half of the single wave case (Case 3) fill height. Figure 3.25 shows the history data for these two cases. As in the low input pressure ratio cases, the dynamic part of the velocity history governs the cycle fill height. Since the imposed waveform occupies only a small fraction of a cycle in both of these cases, the effect of doubling the number of waves is similar to halving the perimeter. From this point of view, it is possible to predict the cycle fill height of a two wave case from a single wave case in which the identical input conditions are utilized.

The injector check-off intervals of the three low pressure cases (Case 1, 4, and 6) are nearly identical. Similarly, the high input pressure cases (Case 3 and 9) have close check-off interval. This suggests that the injector check-off interval is also dominated by the dynamic response of the injector.

Figure 3.26 reports impulse attenuation of the 5 cases (Case 1, 3, 4, 6, and 9). Transmitted impulses to the manifold in all cases shown are smaller than the input impulses due to the boundary condition explained in section 3.2.1. Also, the impulses' information contain the impose wave and the reflected wave(s): the two wave cases and the small diameter case have two reflection waves while the other single wave cases have one reflection wave. Interestingly, the two wave case with input pressure ratio=8 and the small diameter case are identical. This implies that an n-times diameter manifold with n-times number of wave, gives the same manifold attenuation. The impulse near the outlet boundary in the two wave case with the input pressure ratio=19 is attenuated more than the comparable single case since the manifold pressure in the two wave case is higher than the single wave case. The dip position agrees in both the single wave cases and double wave cases, and the shape of attenuation curve among the same wave number cases is similar.

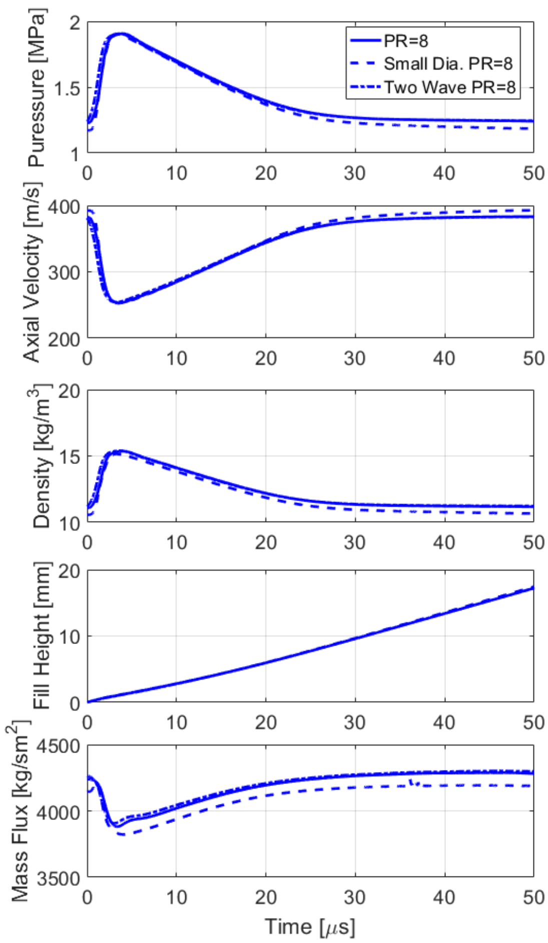


Figure 3.24. Pressure, Axial Velocity, Density, Fill Height, and Mass Flux History of Cases (Case 1, 4, 6) for $50\mu s$: the two wave case is overlapped with the base case.

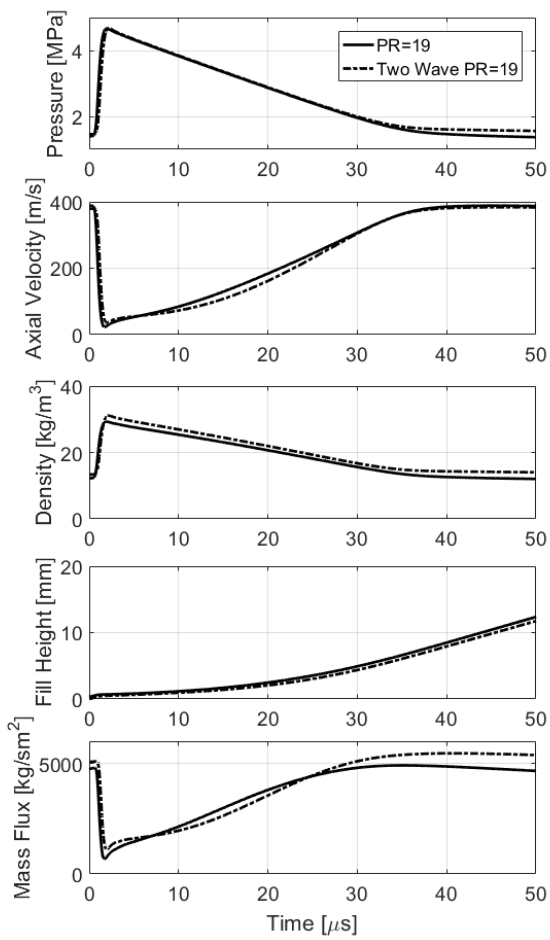


Figure 3.25. Pressure, Axial Velocity, Density, Fill Height, and Mass Flux History of Two wave Case (Case 9) and Single Wave case (Case 3) with input PR=19 for $50\mu s$

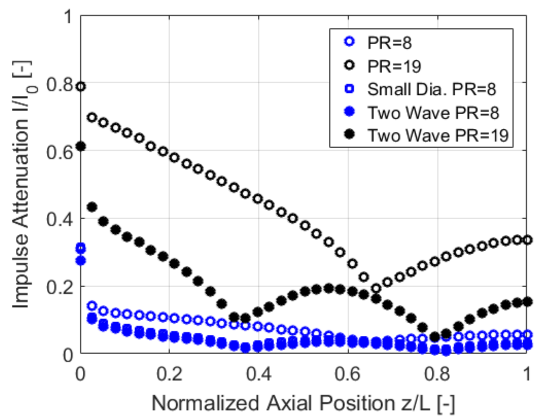


Figure 3.26. Impulse attenuation of the 5 cases (Case 1, 3, 4, 6, and 9). The small diameter case coincides with the two-wave PR=8 case.

### 3.2.5 Effect of Area ratio

Geometry is an important design parameter and effects of injector area ratio is evaluated in high pressure input. Cases 3 and 7 are same except the area ratio. To achieve this, Case 7 has a double size injector gap compare to Csse 3. As expected the average manifold pressure of the larger aspect ratio case (Case 7) is 33% lower than the original geometry case (Case 3). Figure 3.27 shows the pressure fluctuation contour of the wider gap case. The imposed wave propagates into the manifold more than Case 3 (Figure 3.22).

The cycle fill height is reduced mainly due to back flow. Figure 3.28 contains history data of the original geometry and wider gap cases. The wider gap case has back flow after 28 rotations, which is already reached at the limited cycle, because of lower manifold pressure. The lower manifold pressure is caused by the softer choked injector design. There is a slight negative fill height region while the velocity is negative. The velocity recovery of the wider gap case takes roughly 5 longer than the baseline geometry case. A wider gap causes longer recovery time in velocity, and this implies more interaction between the injector and the chamber.

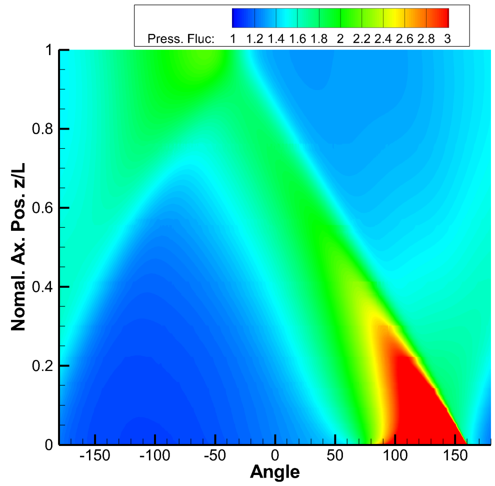


Figure 3.27. Pressure fluctuation contours unwrapped of the input pressure ratio=19 with the wider gap case at R=1.92 inch

The area ratio is also a main factor for check-off interval because of back flow in the larger gap configuration. The back flow results in negative mass flux at the beginning of the cycle. Negative mass flux dramatically increases check-off interval but is still in the order of ten nanosecond.

Wave attenuation inside the manifold is assessed to access the manifold response to the dynamic impulses, which shown in Figure 3.29. The transmitted impulse to the manifold is almost same as the input impulse and decays gradually instead of quick reduction in the first few points from the outlet in Case 7. The dip position shifts to downstream due to the flow velocity change, especially near the outlet.

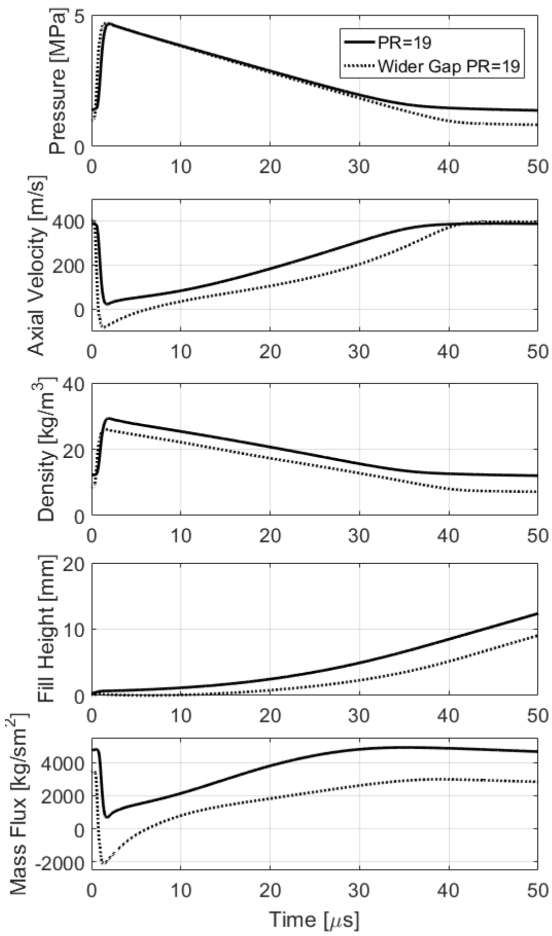


Figure 3.28. Pressure, Axial Velocity, Density, Fill Height, and Mass Flux History of the original geometry case (case 3) and the larger area ratio case (Case 7) with input PR=19 for $50\mu s$

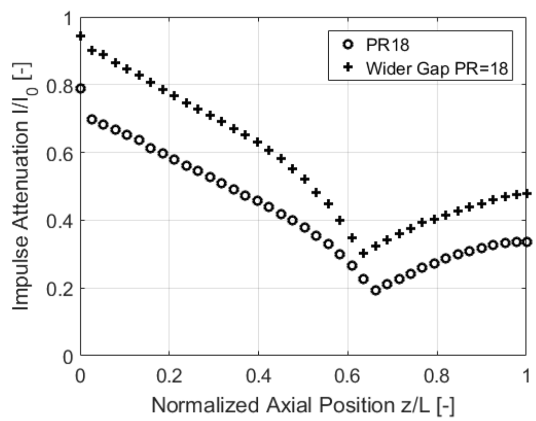


Figure 3.29. Wave attenuation of the case with the larger area ratio and the original geometry case.

# 4. RESULTS AND DISCUSSION FOR SIMULATION OF NON-PREMIXED DETONATION WAVE CHARACTERISTICS WITH VARIABLE MIXING PROFILES

Another parametric study (the 2D simulations described in Section 2.3) is executed on the Rosen Center for Advanced Computing (RCAC)'s Brown cluster at Purdue University. The computational time required per case was approximately 2 days on 96 cores and the equivalent CPU time is 3500 hours with a time step of $5.0^{-9}$ s, the simulated physical time is 0.2 ms. This time corresponds to the arrival of a coupled detonation wave at the other end of the computational domain. The mesh resolution of this study is $0.2mm$, which was determined from the mesh convergence study in Section 2.3. Since this study attempts to assess the injector spacing and mixing efficiency, there exists a possibility that the wave may be decoupled, in which case, the physical time simulated will be shorter than that required for complete consumption of the unreacted propellants. The global equivalence ratio is set to unity for all the cases described herein. The local equivalence ratio which is computed from the mixing efficiency equation 2.3 will vary as a function of the injector spacing chosen paremetrically, as explained in Section 2.3). Table 3.2.5 recalls the concise calculation conditions for this study and there are total 29 simulations (seven injector spacings and four mixing efficiencies plus the perfectly premix case).

Table 4.1. Concise calculation conditions for non-premixed detonation wave parametric study. The detail conditions are in Chapter 2

| | Driver | Runway | Target |
|---|---|---|---|
| pressure [Pa] | 13106031 | 48263 | 48263 |
| temperature [K] | 4002.2 | 354 | 354 |
| velocity in x and y [m/s] | 1121.6, 0 | 0, 0 | 0, 0 |
| mass fraction of $H_2$ | 0.00649 | 0 | mixing efficiency |
| mass fraction of H | 0.00174 | 0 | mixing efficiency |
| mass fraction of $O_2$ | 0.1131 | 0.7996 | mixing efficiency |
| mass fraction of O | 0.027 | 0 | mixing efficiency |
| mass fraction of OH | 0.1014 | 0 | mixing efficiency |
| mass fraction of $HO_2$ | 0.0008 | 0 | mixing efficiency |
| mass fraction of $H_2O$ | 0.3228 | 0 | mixing efficiency |
| mass fraction of $CH_3$ | 1.05E-09 | 0 | mixing efficiency |
| mass fraction of $CH_4$ | 1.88E-10 | 0.2004 | mixing efficiency |
| mass fraction of CO | 0.2154 | 0 | mixing efficiency |
| mass fraction of $CO_2$ | 0.2114 | 0 | mixing efficiency |
| mass fraction of $CH_2O$ | 9.03E-07 | 0 | mixing efficiency |

## 4.1 Perfectly premixed case

Prior to the investigation of the influence of injector spacing and the mixing efficiency, a perfectly premixed case is computed to provide a reference condition for the 2D computations. Figure 4.1(a) shows snapshots of pressure, temperature and heat release. As shown in Fig 4.1(a), the detonation wave in this case propagates from the left to right (the azimuthal direction of an RDE engine) as a near uniform condition perpendicular to the x-axis. The pressure is coupled with the combustion (heat release) as expected in a detonation wave. It should be noted that the detonation cell structure requires presence of non-uniformities and in the absence of such through either the initial or the boundary conditions, it may not appear in the solution as evident from Fig 4.1(a). Line plots for these parameters on the injector surface are presented in Figure 4.1(b) to provide values. he normalized heat release is defined as the heat release at the point divided by 2.5 TW

Figure 4.2 presents the pressure distributions along the injector surface (x=0) at several different instances in time. The peak pressure can be seen to vary slightly with time, but the shape of the pressure wave is similar during the $10\mu s$ considered here. The averaged wave profile during the $10\mu s$ is shown as the black solid line, which represents 100 snapshots during this period. As demonstrated by the pressure profile, the peak pressure of $\approx 1.5MPa$ is approached rapidly. In average, there are four meshes ($0.8mm$) between the peak pressure location and the wave front. The pressure then relaxes close to the CJ value within a distance of $1mm$. After this initial relaxation, the decay rate is lower and the expansion to the specified farfield pressure can be seen to continue over the distance shown.

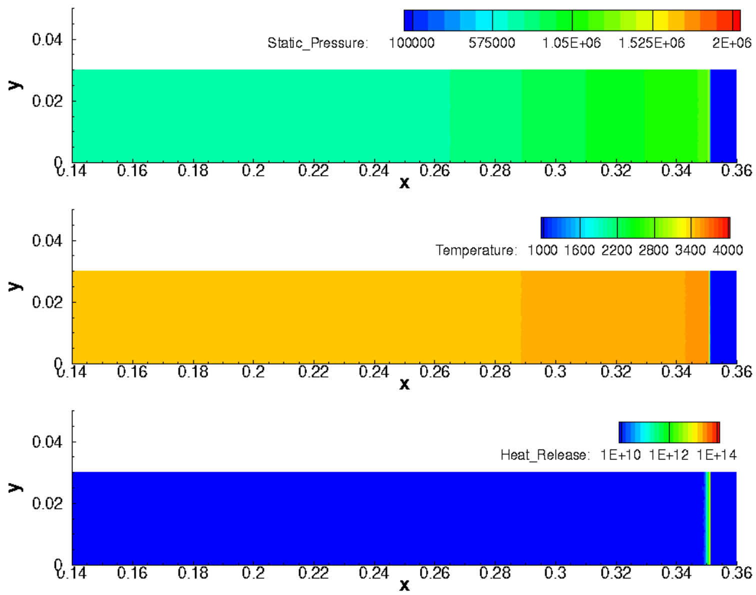


(a) Snapshot of contours at $t = 170.0\mu s$

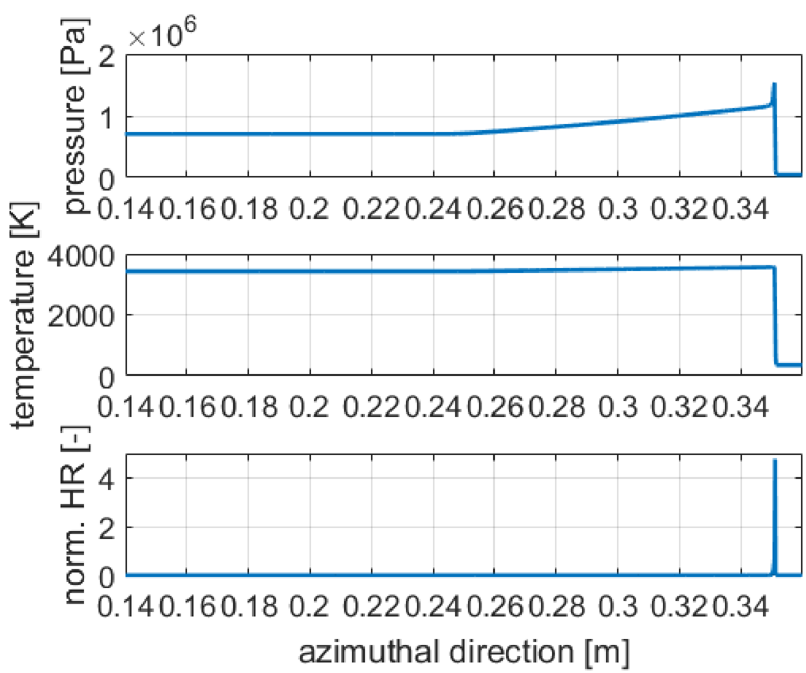


(b) Pressure, temperature and normalized heat release distribution on the injector surface ($y = 0$). The normalized heat release is defined as the heat release at the point divided by 2.5 TW

Figure 4.1. Snapshots of contours and line plots from the premixed case at $t = 170.0\mu s$

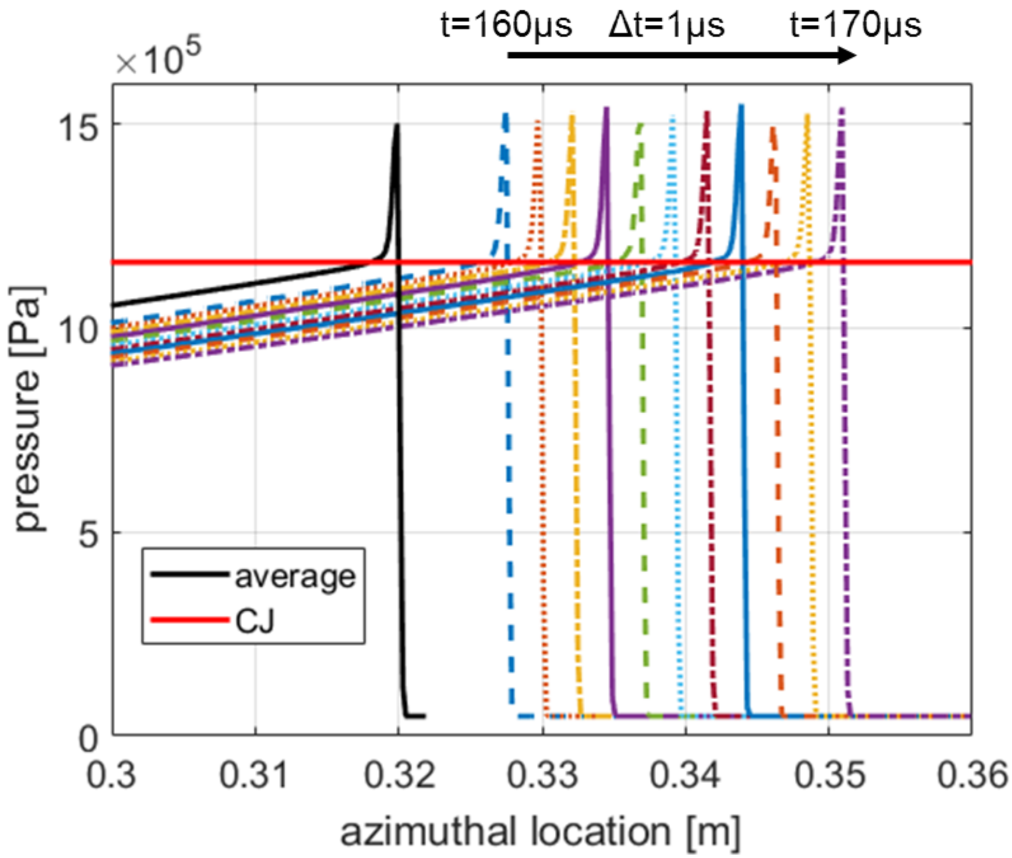


Figure 4.2. Pressure distributions on the injector face

## 4.2 Effects of injector spacing for non-premixed cases

The effects of the injector size are assessed in this section with an objective of determining the maximum allowable injector spacing for the non-premixed cases where the mixing profile does not change along the axial direction (the y-direction of the simulation). A large spacing and injection length scale is desirable for a practical injector to minimize the manufacturing cost and the associated uncertainty. A small spacing and length scale is preferable from the standpoint of operation within the design parameters. Another consideration is the ratio of injection area to injector face area as regions not occupied by injectors serve as aft-facing steps/recirculation zones that may anchor parasitic deflagration from unburned reactants displaced into this region by the detonation wave. The optimal point may lie between the two limits depending on the mission specific injector design.

The initial and boundary conditions used for this study are explained in Figure 2.9 (the computational domain), Table 2.5 and 2.6. The injector spacing, which consists of one oxidizer and fuel injection, is varied in a geometric progression from 360 mm to 180 mm and so on, up to 5.6 mm. Generally, it is observed that the injectors spacings above 90 mm do not sustain the detonation and decoupling is observed during the simulation as shown in Figure 4.3. The global equivalence ratio of unity, maintained in all the cases considered does not preclude such decoupling. The decoupled pressure wave propagates simply as a shock and its speed decreases as the combustion lags further behind. A typical shock propagation velocity of the decoupled cases is below 500 $m/s$. The combustion wave follows with even lower speed than the acoustic velocity and the uniformity in the axial direction may not remain the same as the driving section, as seen from Fig. 4.3.

The cases with 45 mm and finer injector spacing show a similar trend, which comprises of initial decoupling and somewhat delayed re-coupling of the pressure and combustion. The time of decoupling from the start of the simulation and the delay between decoupling and re-coupling is dependent on the injector spacing. Figure 4.4

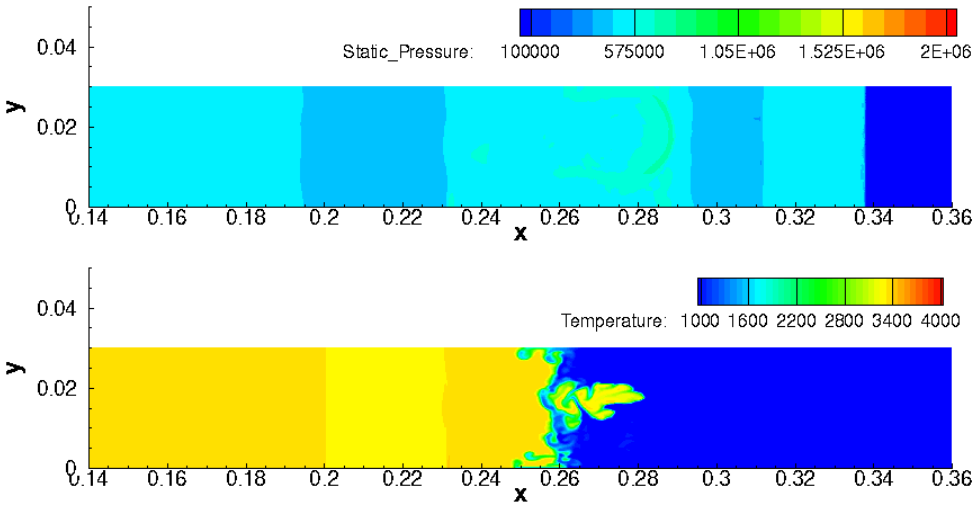


Figure 4.3. Snapshots of non-premixed case with 90mm injector spacing at $t = 300\mu s$.

and 4.5 present a sequence of snapshots of pressure and temperature contours for the 5.6 mm spacing case. At $t = 60.0\mu s$, the decoupled combustion wave accelerates locally. The larger injector spacings - 90 mm and higher show similar local acceleration at some point in time, but it is not sustained to reach a stationary condition in the frame of reference of the wave. In contrast, the shorter spacings show that the combustion continues to accelerate in the pressure wave frame of reference and burns the pressurized, heated and mixed propellants at $t = 70.0\mu s$ and $t = 80.0\mu s$. This "explosion" eventually catches the pressure wave and the re-coupled waves as seen $t = 90.0\mu s$ develop to near stationary detonation at $t = 180\mu s$. This decouple-explosion-re-couple sequence becomes smoother and happens earlier with finer injector spacing. The recoupled wave is almost uniform in axial direction for the 5.6 mm spacing case.

The 45 mm spacing case is a boundary case and although it shows the same decouple-explosion-re-couple sequence, computation diverged during the re-coupling phase. The fully non-premixed propellant case is therefore assumed to have a limitation of 22.5 mm injector spacing for successful re-coupling. This is the largest spacing to sustain the detonation wave in the combustion chamber.

It is worth pointing out that the detonation cell-like structure becomes apparent towards the later part of the simulation, likely due to the presence of non-uniform initial conditions and re-coupling process observed (Fig. 4.1(a)).

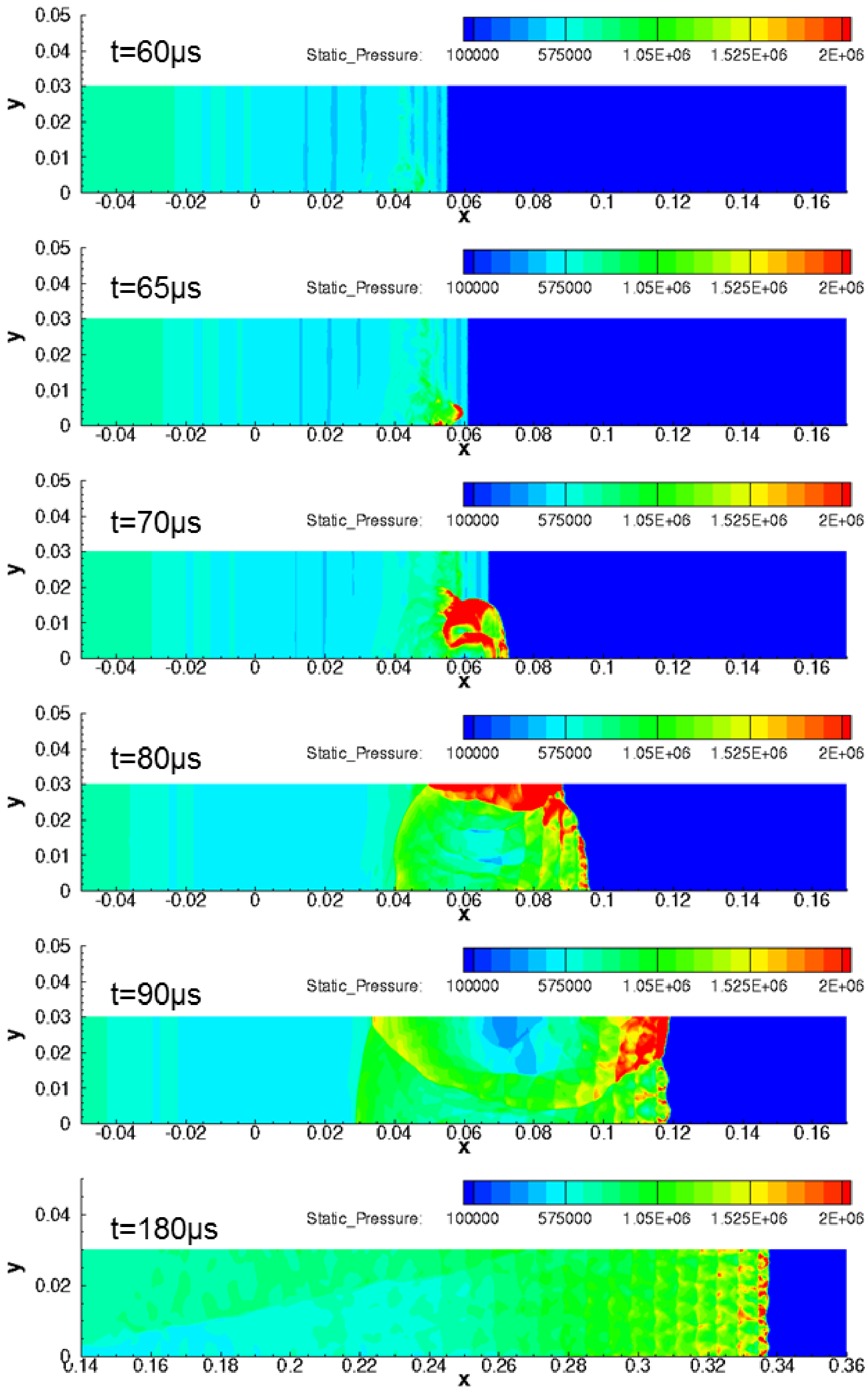


Figure 4.4. Sequential pressure snapshots from the 5.6 mm injector spacing case

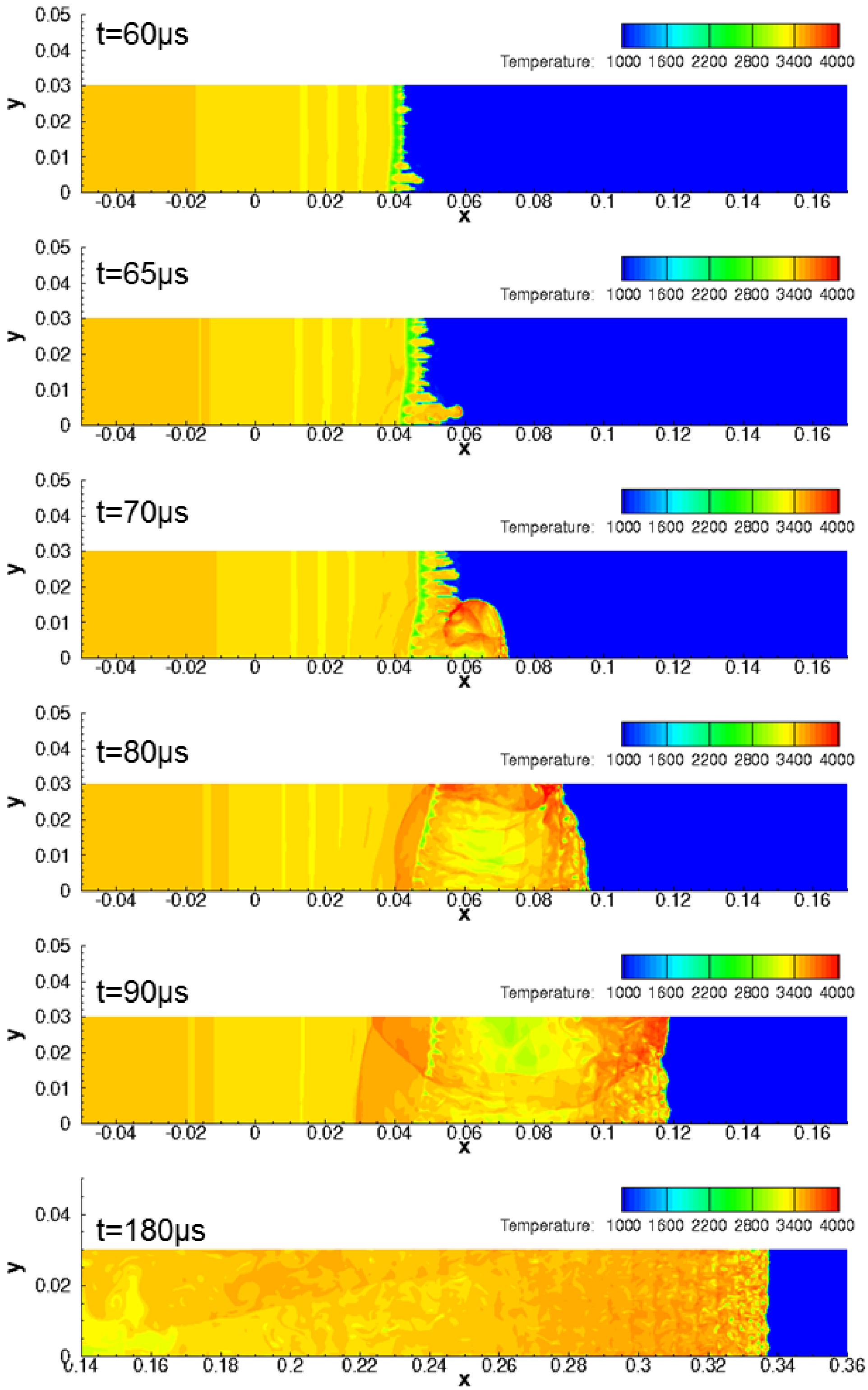


Figure 4.5. Sequential temperature snapshots from the 5.6 mm injector spacing case

In order to quantify differences among all cases, Figure 4.6 shows the average pressure profile at the injector surface (y=0) and time and space averaged axial pressure ($\bar{P}$) profile behind the wave. Due to different instances of re-coupling, the start time for averaging the cases is defined as $40\mu s$ before the leading detonation wave arrives at the 85% of the target region. In each case, the azimuthal and axial pressure profile is averaged using 400 frames (the output frequency is every $0.1\mu s$) taken at equal intervals over a period of $40\mu s$. The average azimuthal pressure profile at the injector surface is computed by aligning the wave fronts at all instances considered. The wave front for a time instance is picked as the location of first non-zero pressure gradient from the sample profile shown in Fig. 4.2. The average pressure behind the wave ($\bar{P}$) is obtained with Equation 4.1 for a length of 0.12 m from the wave front. The 45 mm spacing case is excluded due to the numerical difficulty as mentioned before. Corresponding data is excluded from Fig. 4.6. All the decoupled cases with 90 mm and larger spacing are also excluded from the Fig 4.6(b).

$$\bar{P} = \frac{\int_{len}^{\text{wave front}} p(x)dx}{len}, \quad where\ len = 0.12\ m \tag{4.1}$$

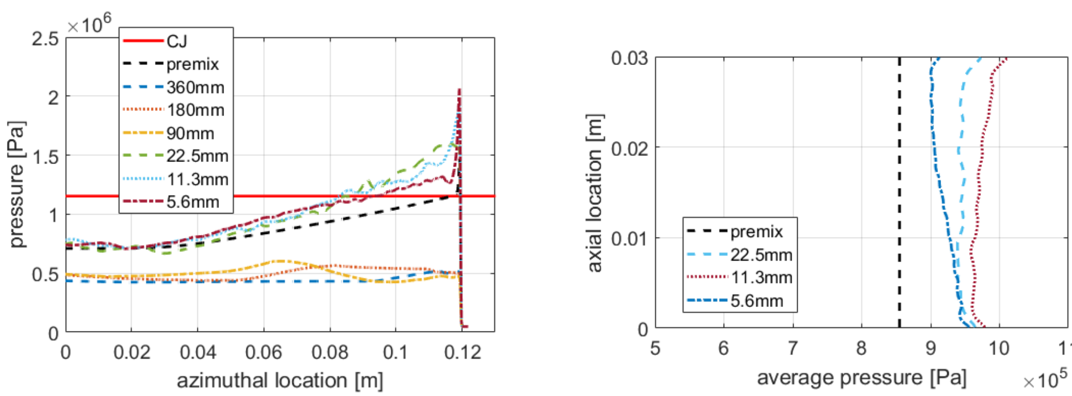


(a) Averaged pressure profile on the injector face. the x-axis represents the azimuthal direction of an RDE, which is the x-direction of contours.

(b) Time and space (0.12m from the wave front) averaged pressure. the y-axis represents the axial direction of an RDE, which is the y-direction of contours

Figure 4.6. Non-premixed cases

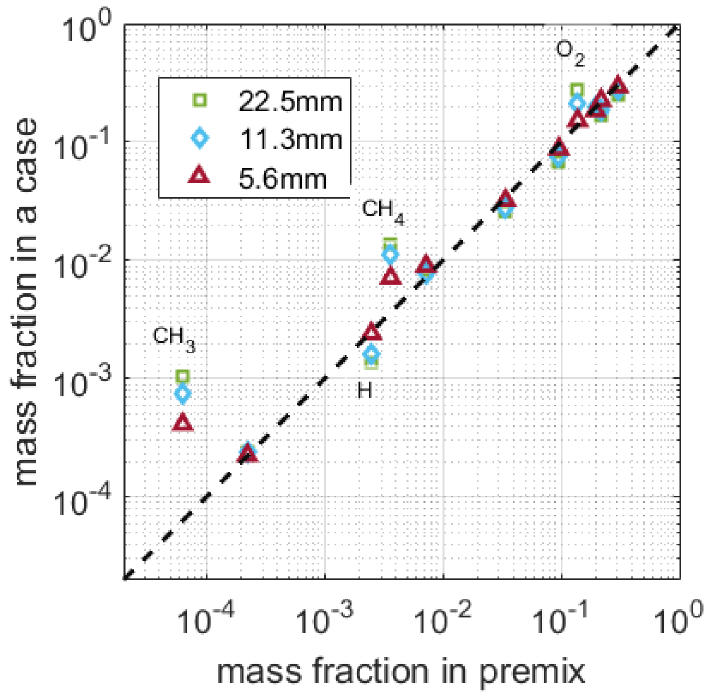


Figure 4.7. Time and space (0.12m from the wave front) averaged mass fraction of species against the Time and space (averaged over axial direction at wave front ) averaged mass fraction of the premixed case

The azimuthal pressure profiles of cases with 90 mm and larger spacing shown in Fig 4.6(a) display a decoupling of pressure and combustion. The peak of the averaged pressure profile of the coupled detonation cases is larger than the premixed case and a more detailed analysis is required to explain this difference. The Chapman-Jouguet condition assumes that the products of combustion are at an equilibrium condition. The analysis of von Neumann [54] as explained by Lee [55] does take into account the degree to which the combustion is complete, but neither approach takes into account possible alternate pathways that are inherent to chemical kinetics with reversible elementary reactions. This can be evaluated based on the deviation of the products composition in the case of non-premixed case from that of the premixed case. Such deviation is easy to assess using a parity plot as shown in Figure 4.7. The specific difference highlighted in this figure is that the unburnt fuel, oxidizer and their derivatives in the non-premixed combustion products exceed those in the premixed case by 100% to orders of magnitude. This is a clear indication of either protracted heat release or intense heat release. The rich mixtures, where the oxidizing radicals are limited show the former - a delayed heat release, but this does not match with the presence of additional oxygen as seen from the Fig 4.7. The other possibility is the extreme heat release rates that delay the equilibrium. This is a more likely scenario based on the temperatures seen from Fig 4.5. The time and space averaged pressure profiles that exceed the premixed case are possibly the result of this difference, which is akin to a series of explosions and subsequent thermo-acoustic amplification.

## 4.3 Effects of mixing efficiency

As explained in Section 2.3, four profiles are considered for this study. Two of these - the non-premixed and "poor" consider that the entire target region remains partially premixed at best. The other two profiles attain near global equivalence ratio towards the end of the target region, which is then expected to best support the coupling of the shock and reaction front in the detonation wave. For the purpose of assessing the effects of mixing efficiency profiles, the injector spacing is fixed at 22.5 mm, which supports a coupled detonation for all the profiles selected.

Figure 4.8 shows contours of the baseline mixing profile with 22.5 mm injector spacing. This set of contours is also representative of the Gaillard mixing profile, while the results of poor mixing profile resemble those of the non-premixed cases presented in the previous section. This is due to the fact that closest to the top of the fill region, the "poor" mixing profile is still 50% non-premixed while at the bottom it is exactly non-premixed. In the case of the remaining two mixing profiles (baseline and Gaillard), the initial condition driven detonation wave is sustained near the top, since the cells near the top edge have perfect mixing. Below the clearly coupled detonation wave, an unsteady oblique shock propagates with the same velocity as the detonation wave. Due to the partially premixed reactants and corresponding longer induction times, there are locally higher or lower pressure pockets along the oblique shock. These variations are further accentuated by the transient wave based mixing and combustion towards the bottom.

Between the oblique shock and the injector surface (the bottom edge), combustion is intermittent and dependent on the injector spacing. At the $t = 160\mu s$ of this baseline mixing case, the intermittent combustion shows a higher pressure ratio than the detonation wave. This was explained in more detail in the prior discussion. The similarity is supported by Fig 4.8, which shows temperature and $O_2$ mass fraction contours; containing unburnt pockets of reactants. Similar observations are also reported in the literature [26, 32]. The reflected oblique shock at the bottom edge or injector face creates a higher compression, more intense heat release and thus greater pressure ratio. The reflected oblique shock propagation to the top of the fill region can be seen, but without significant thermo-acoustic coupling as apparent from the $O_2$ mass fraction contour shown in Figure 4.8.

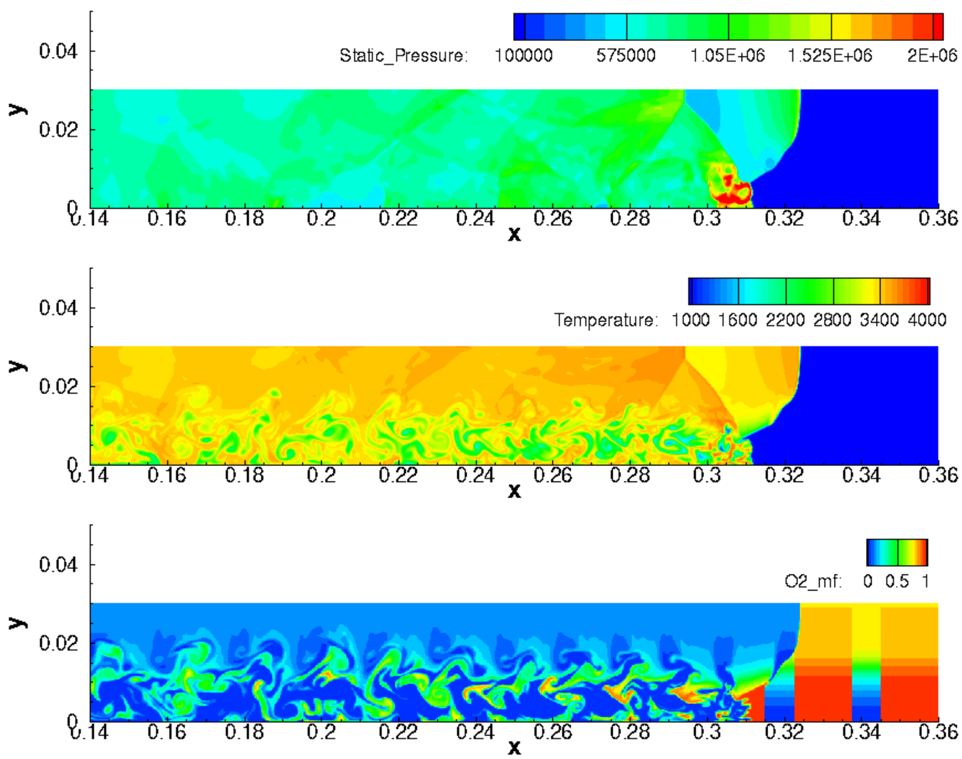


Figure 4.8. Snapshot contours of the 22.5 mm spacing with the baseline mixing at $t = 160\mu s$

A further quantified assessment of the effect of variation in mixing profiles is sought using averaged pressure profiles in axial and azimuthal directions. Figure 4.9(a) and Figure 4.9(b) present the summary results of the four mixing profiles selected. Fig 4.9(a) shows the temporally averaged pressure profiles at the injector surface. The peak pressure in all of the four mixing profiles is greater than that in the premixed case. The decay of peak pressure is directly related to the mixing profile and will be further examined in the next section. Figure 4.9(b) shows the average axial pressure profile behind the wave ($\bar{P}$) within the length of 0.12m. The pressure at the injector face for baseline and Gaillard profiles is nearly the same as the premixed case. The non-premixed and poor cases have larger pressure at this axial location, which implies better performance and larger risk of a backflow at the injector plane. It is worth to pointed out that the averaged pressure from the poor mixing cases resembles it of the non-premixed cases. The average pressure value changes with axial location for the baseline and the Gaillard mixing profile with the peak value at the bottom edge. Given this observation, it may be possible to attain a desired axial pressure profile through injector design for specific mixing profile.

In order to determine the impact of averaging length on the axial pressure profile, Figure 4.10 considers two additional length scales 0.10 m and 0.08 m (len in Equation 4.1). The shorter length scale can be alternatively thought of as having a greater number of detonation waves. The axial profiles thus obtained show similar trends. The magnitude of the pressure difference between various mixing profiles and the premixed results increases with shorter averaging length scale, as expected. Increasing the number of waves in such scenarios may be advantageous from the viewpoint of pressure thrust as the performance metric.

Figure 4.11 presents the time and space (0.12m from the wave front) averaged mass fraction of species against those from the premixed case (22.5mm injector spacing). All the mixing profiles indicate deviation from the premixed case. Combined with the fact that locally higher pressure and temperature values are observed towards the

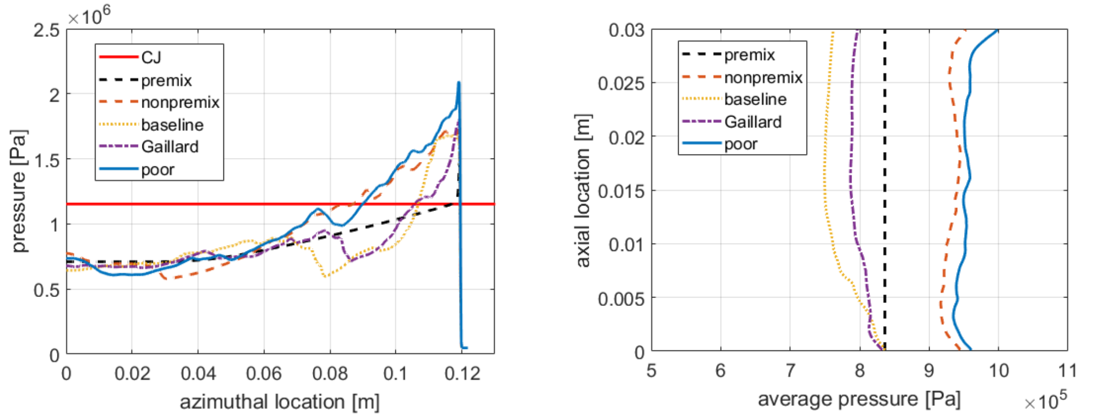


(a) Averaged pressure profile on the injector face (b) Time and space (0.12m from the wave front) averaged pressure

Figure 4.9. 22.5mm injector spacing cases

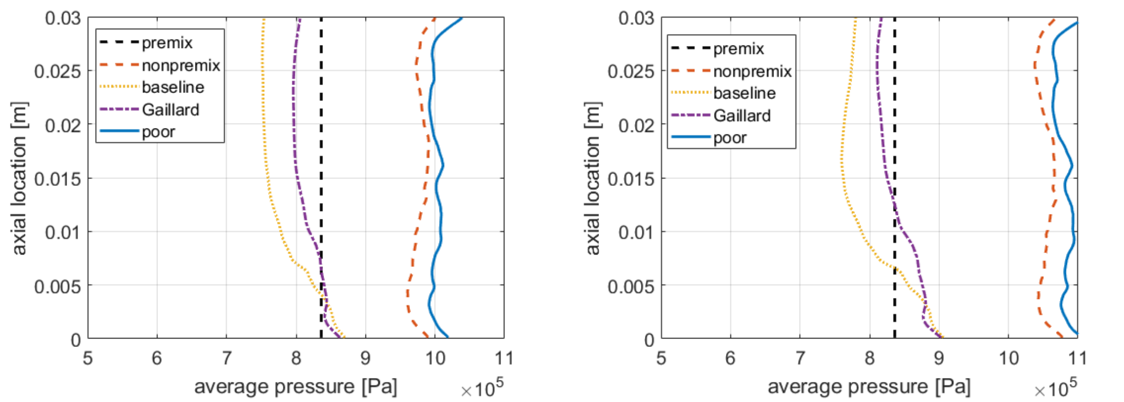


(a) Time and space (0.10m from the wave front) averaged pressure (b) Time and space (0.08m from the wave front) averaged pressure

Figure 4.10. Time and space averaged pressure comparison for 22.5mm injector spacing cases

bottom of the fill region, the partially complete combustion can be a factor that is beneficial in a non-ideal mixing profile.

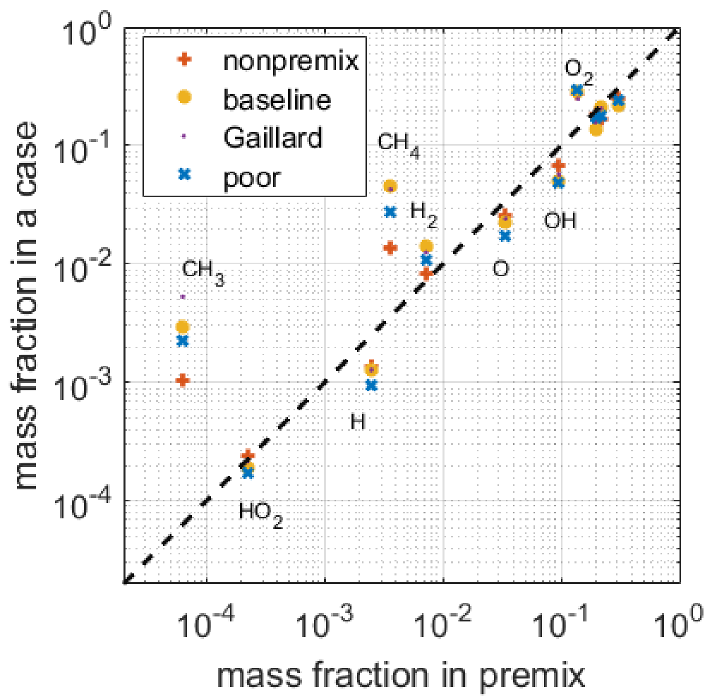


Figure 4.11. Time and space (0.12m from the wave front) averaged mass fraction of species against the Time and space (averaged over axial direction at wave front ) averaged mass fraction of the premixed case (22.5mm injector spacing)

Further analysis of the pressures higher than the ideally premixed case is needed to understand the underlying cause. This purpose is served by considering point monitors in various regions of the flow field. Four such point monitors are shown in Figure 4.12. The locations of the points are 0.2700, 0.2738, 0.2776, and 0.2851 mm from the start of the target region. Pressures and heat release histories at these points are presented in the figure. The four locations chosen track the detonation wave spatially as it passes an oxygen-to-fuel-boundary, the center of a fuel band, a fuel-to-oxygen-boundary, and the center of an oxygen band respectively. The normalized heat release is defined as the heat release at the point divided by 2.5 TW. All data is shifted in time so that the pressure front is located at $t = 0.5\mu s$.

The ZND model [54, 56, 57] assumes the following structure: Firstly, there is an adiabatic shock compression and heating where the wave propagation velocity determines the Mach number with respect to the cold reactants. The compressed and heated propellants dissociate, forming radical pool necessary for the subsequent ignition. In this stage the pressure and temperature are assumed to remain the same as after the shock induced compression. Once the radical concentrations are sufficiently high, a rapid energy release occurs that raises the temperature but reduces the pressure until the CJ pressure and product choking conditions are reached. Depending on boundary/initial conditions present behind the detonation, an expansion fan may follow the detonation wave. In the classical version of this model, the pressure increment only occurs at the shock without any chemical processes. A shock-detonation toolbox has been developed by the research group of Prof. Shepherd [53]. It allows computation of the induction time, which is the time between the shock to the peak heat release. It is approximately $3.49\mu s$ for the globally premixed condition reported herein. The corresponding peak pressure is noted as $\approx 2.17MPa$. As the detonation wave progresses across the points categorized above, it is expected that the heat release process slightly differs due to non-premixed reactants. The ZND theory can also take into account detailed chemical kinetics with different time scales of exothermic and endothermic reactions, thereby allowing the state known as "pathological detonations". These are typically overdriven detonations where the exothermic time scales are shorter than the endothermic time scales, realizing the possibility of intersecting Hugoniot curves. It is of interest to assess the presence of such in the non-premixed cases.

The pressure and heat release at several points are plotted in Figure 4.12. At each point shown, the heat release begins at the same time as the arrival of the shock. This is the first distinction of the simulation results from the classical picture of a shock followed by combustion. As the detonation passes the boundary from oxygen-to-fuel (0.2700) and from fuel-to-oxygen (0.2776), the maximum heat release takes a place within $0.5\mu s$. It is worth noting here that the computational temporal resolution of $0.05\mu s$ and the sampling frequency of 10 MHz allows sufficient number of points during the heat release transient described. Although the points at the center of the fuel and oxidizer bands show relatively lower and slower heat release, it can be seen to occur earlier than the computed induction time for the ZND model estimate that is based on distinct shock and combustion regions. Presence of multiple heat release peaks including instances of negative heat release are further supporting the possibility of time scale separation of various reactions due to the non-premixed nature of the reactants. The resulting peak pressure, although close to the prediction of the ZND model, shows multiple peaks. In one particular instance - at the center of the oxidizer band, the heat release appears greater than the ZND model predictions. This case needs a further analysis to understand the reason behind the higher pressure.

The highest pressure at the center of the oxidizer band can be better understood from a normalized p-v diagram. It is further useful to simultaneously follow the heat release and pressure increase at the point under consideration. These quantities are plotted in Figure 4.13(a). The corresponding normalized p-v diagram augmented with the ZND model as well as the premixed case is shown in Figure 4.13(b). Both the figures show that the initial pressure rise occurs within first five points. The premixed case shows a similar pressure rise within four points and the peak is limited to a value lower than the non-premixed case. The delay between start of the shock compression

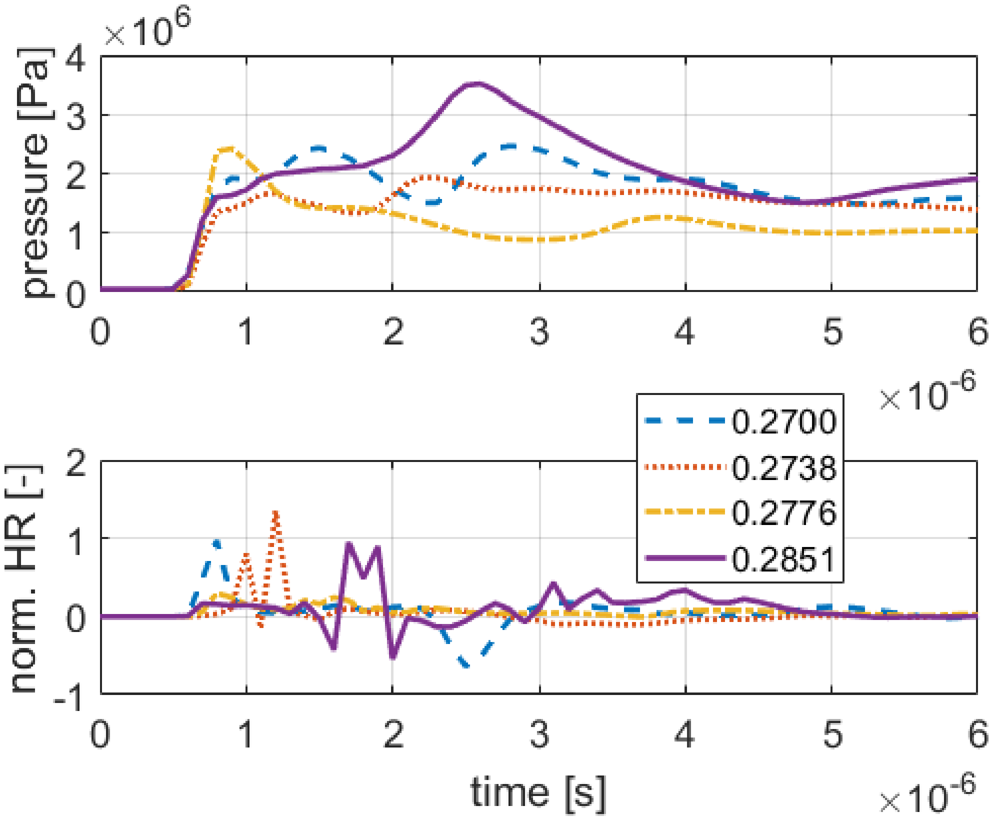


Figure 4.12. Pressure and normalized heat release histories from the non-premixed case with 22.5 mm injector spacing.the four points (0.2700, 0.2738, 0.2776, and 0.2851 mm) represent oxygen-to-fuel-boundary, fuel-center, fuel-to-oxygen-boundary, and oxygen-center, respectively. The normalized heat release is defined as the heat release at the point divided by 2.5 TW. All data is shifted in time as the pressure front is located at $t = 0.5\mu s$.

and the peak heat release for the premixed case is lower than the non-premixed case. This allows the shock induced compression in the non-premixed case to to proceed closer to the von Neumann spike. The variation in the peak pressure as a result of chemical kinetics processes has been noted by Nordeen [58].

The ZND model shows peak pressure equal to the von Neumann spike. The heat release starts at this point and the state approaches the CJ or the tangency condition to the final Hugoniot curve by the completion of combustion. The premixed case follows this closely, albeit at a lower peak pressure than the ZND model. This phenomenon is well noted in the literature [58,59]. The non-premixed case, however, shows a much different picture. In this case, the delayed heat release begins closer to the peak pressure point and occurs nearly as a constant pressure process on the p-v diagram. Beyond this heat release, the point experiences additional compression. Such a compression could be due to the non-uniformities present in the flowfield as seen from Figure 4.4. The simultaneous compression and exothermic reactions are responsible for the higher pressure observed in this case. Subsequent to the peak pressure, the heat release continues and pressure reduces. It is followed by another nearly constant-pressure process that corresponds to endothermic behavior. This clearly demonstrates the separation of exothermic and endothermic time scales. A similar case has been hypothetically discussed by von Neumann [54] by considering intersecting Hougoit curves. It is shown in Figure 4.14. Such occurrence has been experimentally demonstrated. It is noted to be due to partially complete reactions [55] and leads to the pathological and overdriven detonations.

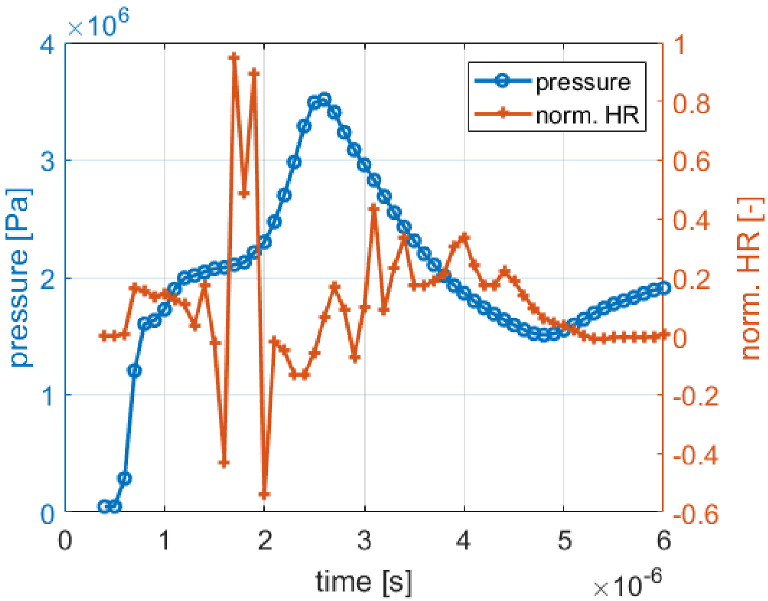


(a) Selected pressure and normalized heat release histories at 0.2851 of the non-premixed 22.5 mm injector case

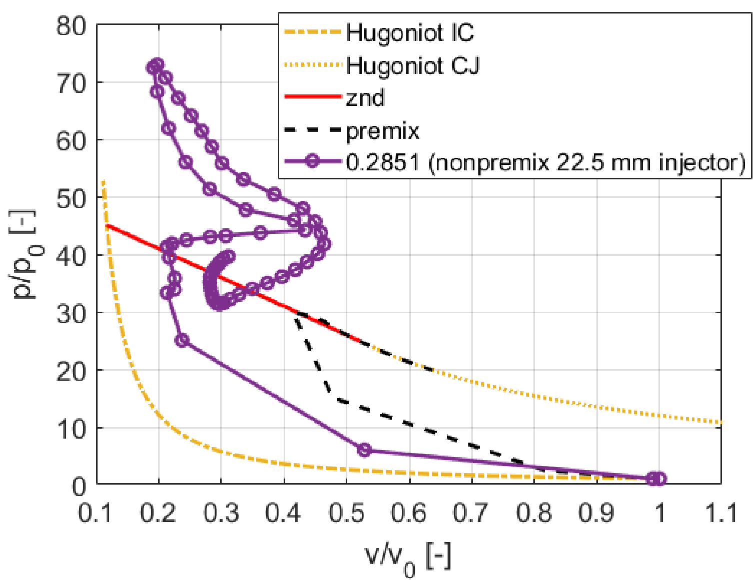


(b) Pressure and volume diagram of the ZND result, the premixed case, and the 0.2851 of the non-premixed 22.5 mm injector case

Figure 4.13. Selected data at 0.2851 of the non-premixed 22.5 mm injector case

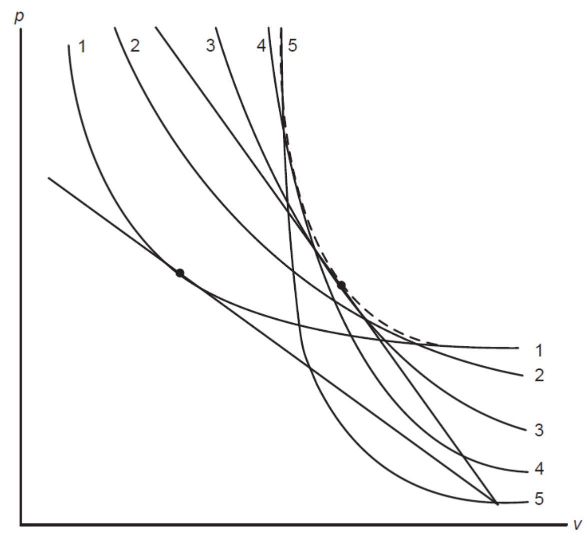


Figure 4.14. Partially reacted Hugoit curves that intersect [54]

Table 4.3 summaries the average pressure behind the wave ($\bar{P}$) within a length of 0.12m (len in Equation 4.1). From this table, it can be seen that the poor mixing profile with 11.3 mm injector spacing outperforms the rest in terms of the average pressure. This trend is observed with injector spacings that are 22.5 mm or finer.

Table 4.2. Time and space average pressure at the injector surface for all cases with length of 0.12 (len in Equation 4.1)

| Case | Time and space average pressure $\bar{P}$ [MPa] | Case | Time and space average pressure $\bar{P}$ [MPa] |
|---|---|---|---|
| premixed | 0.836 | 360mm Gaillard | 0.759 |
| 360mm non-premixed | 0.524 | 180mm Gaillard | 0.779 |
| 180mm non-premixed | 0.485 | 90mm Gaillard | 0.781 |
| 90mm non-premixed | 0.488 | 45mm Gaillard | 0.815 |
| 45mm non-premixed | 0.695 | 22.5mm Gaillard | 0.833 |
| 22.5mm non-premixed | 0.945 | 11.3mm Gaillard | 0.840 |
| 11.3mm non-premixed | 0.940 | 5.6mm Gaillard | 0.834 |
| 5.6mm non-premixed | 0.913 | 360mm poor | 0.505 |
| 360mm baseline | 0.714 | 180mm poor | 0.503 |
| 180mm baseline | 0.726 | 90mm poor | 0.486 |
| 90mm baseline | 0.744 | 45mm poor | 0.608 |
| 45mm baseline | 0.802 | 22.5mm poor | 0.961 |
| 22.5mm baseline | 0.837 | 11.3mm poor | 0.984 |
| 11.3mm baseline | 0.834 | 5.6mm poor | 0.835 |
| 5.6mm baseline | 0.835 | | |

# 5. CONCLUSIONS AND RECOMMENDATIONS

## 5.1 Conclusions

Rotating detonation engines (RDEs) generate dynamic injection processes that can couple with the combustion field contributing both to waveform topology and strength. A series of 3-D unsteady simulations have been conducted to enhance understanding of the dynamic response of annular injectors that are frequently used in both airbreathing and rocket RDEs. The effect of detonation waveform shape (total impulse and total pressure ratio), number of waves, and the design of the annular injector (length and area ratio) have been assessed.

In general, all the results show a strong attenuation of the detonation overpressures in the near field of the injector exit and as a result, the wave traversing the annular passage is largely acoustic in nature. With the mass flow inlet boundary condition employed, reflections are present at this boundary and reflected waves have a non-negligible contribution to the transient mass flow of the injector. These mass flow pulsations could conceivably contribute to the formation of additional waves depending on their energy content and subsequent detailed mixing and combustion. Often observed alternating strong and weak waves in the limit cycle of a RDE combustor are likely a result of the injector dynamics. The lifetime of the reflected waves is limited in the the baseline case of the 3D injector dynamics simulation due to the passage of subsequent detonation waves and strong attenuation near the exit of the injector.

Increasing the number of waves or shortening the length of the injector created reflections as one would predict from acoustic behavior. The transient mass flow produced by passing detonation waves has a relatively small effect on the fill characteristics (fill height) for the cases studied. In the presence of higher amplitude waves these effects will likely be higher. Together with the non-linearities in the heat release, the small fluctuations in the mass flow can significantly alter the detonation behavior.

The two dimensional non-premixed detonation parametric study further examines the effects of the potential non-uniform mixture due to the injector dynamics exposed to a single planer detonation wave. In all non-premixed cases, the detonation wave is decoupled with the pressure wave (the shock) and the combustion wave once the detonation wave arrives at the non-premixed target region. In the cases with the 45 mm and smaller injector spacings, the combustion wave which is decoupled from the detonation wave accelerates after a certain time depending on the injector spacing. Then the accelerated combustion wave burns the mixture between the shock and combustion wave where the mixture has been heated and pressurized by the shock. This rapid explosion eventually catches the shock and these two waves then recouple. This decouple-explosion-recouple sequence becomes smoother and happens earlier with finer injector spacing. The recoupled wave is almost flat and perpendicular to the axial direction for the 5.6 mm spacing case. However, there are some higher pressure pockets than the CJ and the premixed case.

The poor mixing efficiency cases show similar trends to the non-premixed cases: the decouple-explosion-recouple sequence and the local high pressure pockets. The local higher pressure which exceeds in value compared to the premixed case is caused by delayed heat release behind the shock, almost constant pressure combustion, and another compression from the upstream high pressure pockets. The enhanced compression and the almost constant pressure combustion are the result of time scale separation of exothermic and endothermic reactions due to the non and poor mixing efficiencies. The compression observed in the middle of the oxidizer band on the injector surface is closer to the classical ZND : the shock is the only pressurization mechanism for the mixture. In contrast, the combustion starts at the same time as the shock arrives in the premixed, the baseline and Gaillard mixing efficiency cases in CFD.

With good mixing efficiencies, the detonation wave is sustained in regions that have nearly perfect mixing efficiency, instead of the decouple-explosion-recouple sequence. The oblique shock is formed and propagated to the bottom (i.e. the injector surface) with unsteady combustion occurring on the oblique shock. The oblique shock reflects at the injector surface and the reflection pressurizes the mixture with subsequent wave based mixing and combustion. The peak pressure on the injector surface in these cases is *larger* than the premixed case. Additionally, there are unburnt fuel and oxidizer behind the combustion wave.

The non-premixed and poor mixing efficiency cases with the 45 mm or finer injector spacings provide the higher time and space averaged pressure at the injector surface than that of the premixed case. The poor mixing profile with 11.3 mm injector spacing is the best performer among all the cases in this part of parametric study with respect to pressure thrust. It may be possible to attain a desired axial pressure profile through injector design for specific mixing profile.

## 5.2 Future work

The two parametric studies have provided some insight for design and operational performance of RDEs. However, there are some unanswered questions regarding these studies. In order to resolve these questions, the following changes and additional simulations should be conducted:

1. Additional 3D injector dynamics parametric study further studying injection area ratio, wave strength, and injection profile.

2. Additional 2D non-premixed detonation parametric study considering different propellants and operating conditions. In particular, the effect of operating pressure is of critical interest.

3. High fidelity injector mixing simulations which focus on the mixing of propellants against multiple detonation waves.

4. Evaluations of chemical kinetic mechanisms specifically for the detonation conditions.

In the 3D injector dynamics parametric study, the parameters are limited to the pressure ratio, the area ratio and length of the injector, and the number of waves. However, the injector can be designed with more freedom. For example, the contraction rate could be non-linear. Also, the imposed pressure profile can be more realistic such as an exponential decay from the peak pressure rather instead of the linear decrement imposed currently.

About the 2D non-premixed detonation simulation, there is the only one initial condition (pressure. temperature, and global equivalence ratio), whereas the detonation behavior is highly affected by the initial temperature, pressure and global equivalence ratio. A similar parametric study must be performed at higher pressure condition since rocket applications operate at higher pressures than air breathing applications. The initial condition also highly affects the detonation behavior through its influence on the chemical kinetics. These observations point out that simulations with finer divisions in the injector spacing and more variety in the mixing efficiency profile may be needed. Other parameters can be introduced in this type of study and an example is the product gas recirculation.

As explained in the Introduction section, there are several full 3D RDE simulations but the coupling of injector and chamber may not have always been incorporated. The injector dynamic affects the mixing efficiency and Gaillard et. al. [9, 28] provide an example of this. In a similar vein, characterization of the mixing efficiency with the design of injector and its dynamics would be desirable. Since the mixing occurs in three dimensions and it is highly time dependent, detailed computation of the turbulence in unsteady flows is appropriate and should be adopted. Although conjectured computational load is relatively high for a research group in a university setting, the simulations will become feasible with the advances in high performance computing.

Since the methane and oxygen chemical reaction is one of the most studied combustion reactions, there are many versions. The ignition delay in a condition is highly depend on the mechanism as evident in Figure 2.8. In this paper, FFCM-Y [48] is utilized because of its good balance between the computational cost and accuracy. However, it is important for further investigation that the chemical kinetic mechanisms be inspected. A small change in ignition (and ignition delay) drastically changes the heat release timing and eventually affects the detonation. This research must target detonation conditions and compare with existing experimental data.

# REFERENCES


[1] E. Wintenberger and J. E. Shepherd. Thermodynamic Cycle Analysis for Propagating Detonations. *Journal of Propulsion and Power*, 22(3):694–697, 2006.

[2] J. A. Nicholls and R. E. Cullen. The Feasibility of a Rotating Detonation Wave Rocket Motor RPL-TDR-64-113. Technical report, 1964.

[3] B V Voitsekhovskii, V V Mitrofanov, and M E Topchiyan. Stucture of the Detonation Front in Gases (Survey). *Combustion, Explosion and Shock Waves*, 5(3):385–395, 1969.

[4] Frank K. Lu and Eric M. Braun. Rotating Detonation Wave Propulsion: Experimental Challenges, Modeling, and Engine Concepts (Invited). *Journal of Propulsion and Power*, 30(September-October):1125–1142, 2014.

[5] Fedor a. Bykovskii, Sergey a. Zhdan, and Evgenii F. Vedernikov. Continuous Spin Detonations. *Journal of Propulsion and Power*, 22(6):1204–1216, 2006.

[6] Douglas A Schwer and K. Kailasanath. Numerical Investigation of Rotating Detonation Engine. *46th AIAA/ASME/SAE/ASEE Joint propulsion Conference & Exhibit*, (July):1–15, 2010.

[7] David Stechmann, Stephen D. Heister, and Swanand Sardeshmukh. High-Pressure Rotating Detonation Engine Testing and Flameholding Analysis with Hydrogen and Natural Gas. *55th AIAA Aerospace Sciences Meeting AIAA/SAE/ASEE Joint Propulsion Conference*, (January):1–17, 2017.

[8] Daniel E Paxson. A General Numerical Model for Wave Rotor AhalysiS. Technical report, 1992.

[9] Thomas Gaillard, Dmitry Davidenko, and Francis Dupoirieux. Numerical Investigation of an Unsteady Injection Adapted to the Continuous Detonation Wave Rocket Engine Operation. *Eucass*, (JUNE), 2015.

[10] DA Schwer and K Kailasanath. Effect of Inlet on Fill Region and Performance of Rotating Detonation Engines. *AIAA Paper*, (August):1–17, 2011.

[11] Douglas A. Schwer and Kailas Kailasanath. Feedback into Mixture Plenums in Rotating Detonation Engines. *50st AIAA Aerospace Sciences Meeting including the New Horizons Forum and Aerospace Exposition*, (January):1–15, 2012.

[12] Douglas A. Schwer and Kailas Kailasanath. On Reducing Feedback Pressure in Rotating Detonation Engines. *51st AIAA Aerospace Sciences Meeting including the New Horizons Forum and Aerospace Exposition*, (January):1–15, 2013.

[13] Douglas A. Schwer, Thomas A. Kaemming, and Kailas Kailasanath. Pressure Feedback in the Diffuser of a Ram-RDE Propulsive Device. *55th AIAA Aerospace Sciences Meeting*, (January), 2017.

[14] S. M. Frolov, a. V. Dubrovskii, and V. S. Ivanov. Three-dimensional numerical simulation of the operation of the rotating-detonation chamber. *Russian Journal of Physical Chemistry B*, 7(1):276–288, 2012.

[15] Sergey M Frolov, Alexey V Dubrovsky, and Vladislav S Ivanov. Three-dimensional numerical simulation of a continuously rotating detonation in the annular combustion chamber with a wide gap and separate delivery of fuel and oxidizer. *Progress in Propulsion Physics*, 8:375–388, 2016.

[16] Peter A T Cocks, Adam T Holley, Chris B Greene, and Martin Haas. Development of a High Fidelity RDE Simulation Capability. *53rd AIAA Aerospace Sciences Meeting*, (January):1–21, 2015.

[17] Peter A. Cocks, Adam T. Holley, and Brent A. Rankin. High Fidelity Simulations of a Non-Premixed Rotating Detonation Engine. *54th AIAA Aerospace Sciences Meeting*, (January):1–18, 2016.

[18] Jason C. Shank, Paul I. King, James Karnesky, Frederick R. Schauer, and John L. Hoke. Development and Testing of a Modular Rotating Detonation Engine. *50th AIAA Aerospace Sciences Meeting*, (January), 2012.

[19] Daniel E Paxson. Relative Reference Frame. *52nd Aerospace Sciences Meeting*, (January):1–14, 2014.

[20] Daniel E Paxson, Matthew L Fotia, John Hoke, and Fred Schauer. Comparison of Numerically Simulated and Experimentally Measured Performance of a Rotating Detonation Engine. *AIAA Aerospace Sciences Meeting*, 5(January):1–11, 2015.

[21] Peter Strakey, Donald Ferguson, Andrew Sisler, and Andrew Nix. Computationally Quantifying Loss Mechanisms in a Rotating Detonation Engine. *54th AIAA Aerospace Sciences Meeting*, (January):1–14, 2016.

[22] Yang Chenglong, Ma Hu, Wu Xiaosong, and Xu Xueyang. A computational and experimental study of injection structure effect on H 2 -air rotating detonation engine. *52nd AIAA/SAE/ASEE Joint Propulsion Conference*, pages 1–12, 2016.

[23] Songbai Yao and Jianping Wang. Multiple ignitions and the stability of rotating detonation waves. *Applied Thermal Engineering*, 108:927–936, 2016.

[24] Dasheng Lim, Stephen D. Heister, David P. Stechmann, Brandon Kan, and Brent Justice. Transient Response of a Liquid Injector to a Transverse Pressure Wave. *51st AIAA/SAE/ASEE Joint Propulsion Conference*, pages 1–17, 2015.

[25] Clinton Bedick, Andrew Sisler, Donald H. Ferguson, and Peter Strakey. Development of a Lab-Scale Experimental Testing Platform for Rotating Detonation Engine Inlets. *55th AIAA Aerospace Sciences Meeting*, (January):1–14, 2017.

[26] Christopher Lietz, Yogin Desai, Ramakanth Munipalli, Stephen A. Schumaker, and Venke Sankaran. Flowfield analysis of a 3d simulation of a rotating detonation rocket engine. In *AIAA Scitech 2019 Forum*, 2019.

[27] Takuma Sato and Venkatramanan Raman. Hydrocarbon fuel effects on non-premixed rotating detonation engine performance. In *AIAA Scitech 2019 Forum*, page 2023, 2019.

[28] T. Gaillard, D. Davidenko, and F. Dupoirieux. Numerical simulation of a rotating detonation with a realistic injector designed for separate supply of gaseous hydrogen and oxygen. *Acta Astronautica*, 141:64 – 78, 2017.

[29] Qingyang Meng, Ningbo Zhao, Hongtao Zheng, Jialong Yang, and Lei Qi. Numerical investigation of the effect of inlet mass flow rates on h2/air non-premixed rotating detonation wave. *International Journal of Hydrogen Energy*, 43(29):13618 – 13631, 2018.

[30] Jian Sun, Jin Zhou, Shijie Liu, Zhiyong Lin, and Wei Lin. Effects of air injection throat width on a non-premixed rotating detonation engine. *Acta Astronautica*, 2019.

[31] Christopher Lietz, Mathias Ross, Yogin Desai, and William A. Hargus. Numerical investigation of operational performance in a methane-oxygen rotating detonation rocket engine. In *AIAA Scitech 2020 Forum*.

[32] Jumpei Fujii, Yoshiki Kumazawa, Akiko Matsuo, Soma Nakagami, Ken Matsuoka, and Jiro Kasahara. Numerical investigation on detonation velocity in rotating detonation engine chamber. *Proceedings of the Combustion Institute*, 36(2):2665–2672, 2017.

[33] XiaoCheng Mi, Andrew J Higgins, Hoi Dick Ng, Charles B Kiyanda, and Nikolaos Nikiforakis. Propagation of gaseous detonation waves in a spatially inhomogeneous reactive medium. *Physical Review Fluids*, 2(5):053201, 2017.

[34] XC Mi, AJ Higgins, CB Kiyanda, HD Ng, and N Nikiforakis. Effect of spatial inhomogeneities on detonation propagation with yielding confinement. *Shock Waves*, 28(5):993–1009, 2018.

[35] Supraj Prakash, Romain Fiévet, and Venkatramanan Raman. The effect of fuel stratification on the detonation wave structure. In *AIAA Scitech 2019 Forum*, page 1511, 2019.

[36] Arnab Roy, Peter Strakey, Todd Sidwell, and Don Ferguson. Unsteady Heat Transfer Analysis to Predict Combustor Wall Temperature in Rotating Detonation Engine. pages 1–14, 2015.

[37] Robert Driscoll, Andrew St. George, and Ephraim J. Gutmark. Numerical investigation of injection within anaxisymmetric rotating detonation engine. *International Journal of Hydrogen Energy*, pages 1–12, 2015.

[38] Y-H Choi and Charles L Merkle. The application of preconditioning in viscous flows. *Journal of Computational Physics*, 105(2):207–223, 1993.

[39] Matthew Evan Harvazinski. *Modeling self-excited combustion instabilities using a combination of two-and three-dimensional simulations*. PhD thesis, PURDUE UNIVERSITY, 2012.

[40] Bonnie J McBride, Sanford Gordon, and Martin A Reno. Coefficients for calculating thermodynamic and transport properties of individual species. 1993.

[41] S Mathur, PK Tondon, and SC Saxena. Thermal conductivity of binary, ternary and quaternary mixtures of rare gases. *Molecular physics*, 12(6):569–579, 1967.

[42] Aiaa editorial policy statement on numerical and experimental accuracy. *Journal of Propulsion and Power*, 25(1):12–12, 2009.

[43] S Venkateswaran and CL Merkle. Evaluation of artificial dissipation models and their relationship to the accuracy of euler and navier-stokes computations. In *Sixteenth International Conference on Numerical Methods in Fluid Dynamics*, pages 427–432. Springer, 1998.

[44] Lei Peng, Dong Wang, Xiaosong Wu, Hu Ma, and Chenglong Yang. Ignition experiment with automotive spark on rotating detonation engine. *International Journal of Hydrogen Energy*, 40(26):8465–8474, 2015.

[45] David C Wilcox. Formulation of the kw turbulence model revisited. *AIAA journal*, 46(11):2823–2838, 2008.

[46] David Paul Stechmann. *Experimental Study of High-Pressure Rotating Detonation Combustion in Rocket Environments*. PhD thesis, PURDUE UNIVERSITY, 2017.

[47] M. Frenklach, H. Wang, M. Goldenberg, G.P. Smith, D.M. Golden, C.T. Bowman, R.K. Hanson, W.C. Gardiner, and V. Lissianski. Gri-mech—an optimized detailed chemical reaction mechanism for methane combustion. *Gas Research Institute Topical Report, GRI-95/0058*, 1995.

[48] R. Xu and Hai Wang. A reduced methane combustion reaction model for chemical propulsion simulations. In *unpublished*, 2018.

[49] David G. Goodwin, Raymond L. Speth, Harry K. Moffat, and Bryan W. Weber. Cantera: An object-oriented software toolkit for chemical kinetics, thermodynamics, and transport processes version 2.4.0, 2018.

[50] Chung K Law. *Combustion physics*. Cambridge university press, 2010.

[51] E.S. Oran, T.R. Young, J.P. Boris, and A. Cohen. Weak and strong ignition. i. numerical simulations of shock tube experiments. *Combustion and Flame*, 48:135 – 148, 1982.

[52] Juan Li, Zhenwei Zhao, Andrei Kazakov, and Frederick L. Dryer. An updated comprehensive kinetic model of hydrogen combustion. *International Journal of Chemical Kinetics*, 36(10):566–575, 2004.

[53] S. Browne, J. Ziegler, and J. E. Shepherd. Numerical solution methods for shock and detonation jump conditions, 2015.

[54] John Von Neuman. Theory of detonation waves. Technical report, Institute for Advanced Study Princeton NJ, 1942.

[55] John HS Lee. *The detonation phenomenon*. 2008.

[56] Yakov Borissovich Zeldovich. On the theory of the propagation of detonation in gaseous systems. 1950.

[57] Werner Döring. On detonation processes in gases. *Ann. Phys*, 43(421-436):9, 1943.

[58] Craig A. Nordeen and Douglas A. Schwer. Quasi-steady-state analysis of a high resolution detonation simulation. In *AIAA Scitech 2019 Forum*.

[59] Douglas A. Schwer, Ryan F. Johnson, Andrew Kercher, David Kessler, and Andrew T. Corrigan. Progress in efficient, high-fidelity, rotating detonation engine simulations. In *AIAA Scitech 2019 Forum*.